Dynamic Stability and Sub-Synchronous Resonance Suppression in Wind-Integrated Grids Using Virtual Inertia Control Scheme

Dissertation submitted to
Visvesvaraya National Institute of Technology, Nagpur
in partial fulfillment of the requirements for the award of
the degree

Master of Technology
in
Power Electronics and Drives

by

Rishav Dutta
(MT23PED009)

under the guidance of

Dr. Jawaharlal Bhukya

Department of Electrical Engineering
Visvesvaraya National Institute of Technology
Nagpur 440 010 (India)

June 2025

Dynamic Stability and Sub-Synchronous Resonance Suppression in Wind-Integrated Grids Using Virtual Inertia Control Scheme

Dissertation submitted to
Visvesvaraya National Institute of Technology, Nagpur
in partial fulfillment of the requirements for the award of
the degree

Master of Technology
in
Power Electronics and Drives

by

Rishav Dutta
(MT23PED009)

under the guidance of

Dr. Jawaharlal Bhukya

Department of Electrical Engineering
Visvesvaraya National Institute of Technology
Nagpur 440 010 (India)

June 2025

© Visvesvaraya National Institute of Technology (VNIT) 2009

Department of Electrical Engineering
Visvesvaraya National Institute of Technology, Nagpur

Declaration

I, Rishav Dutta, hereby declare that this dissertation titled "Dynamic Stability and Sub-Synchronous Resonance Suppression in Wind-Integrated Grids Using Virtual Inertia Control Scheme" is carried out by me in the Department of Electrical Engineering of Visvesvaraya National Institute of Technology, Nagpur. The work is original and has not been submitted earlier whole or in part for the award of any degree/diploma at this or any other Institution / University.

Rishav Dutta
Date: 30th, May 2025

Certificate

This to certify that the dissertation titled "Dynamic Stability and Sub-Synchronous Resonance Suppression in Wind-Integrated Grids Using Virtual Inertia Control Scheme" is submitted by **Rishav Dutta** in partial fulfillment of the requirements for the award of the degree of **Master of Technology in Power Electronics and Drives**, VNIT Nagpur. The work is comprehensive, complete and fit for final evaluation.

30/05/2025

Dr. Jawaharlal Bhukya
Assistant Professor,
Dept. of Electrical Engineering,
VNIT, Nagpur

Dr. B. S. Umre
Head, Department of Electrical Engineering,
VNIT, Nagpur
Date: 30th, May 2025

Department of Electrical Engineering
Visvesvaraya National Institute of Technology, Nagpur

Non-Plagiarism Certificate

This is to certify that the Master of Technology Dissertation titled *"Dynamic Stability and Sub-Synchronous Resonance Suppression in Wind-Integrated Grids Using Virtual Inertia Control Scheme"*, submitted by **Rishav Dutta**, Enrollment No. **MT23PED009**, ID No. **30834**, is an original work carried out by the candidate under the supervision of **Dr. Jawaharlal Bhukya**, Assistant Professor, Department of Electrical Engineering, Visvesvaraya National Institute of Technology, Nagpur. The work presented in this dissertation is genuine and has not been copied from any published or unpublished sources. Proper citations and acknowledgements have been provided wherever references to existing literature or external contributions have been made. The dissertation has been subjected to a plagiarism check using the standard software tool, **Turnitin**, and the overall similarity index was found to be within the permissible academic limits as prescribed by the institute. This certificate is issued in accordance with the academic policies of **VNIT Nagpur**. A summary of the report is provided below.

ORIGINALITY REPORT

18%	12%	15%	%
SIMILARITY INDEX	INTERNET SOURCES	PUBLICATIONS	STUDENT PAPERS

Rishav Dutta,
Enrollment No.: MT23PED009,
ID No.: 30835,
Date: 30th May 2025

30/05/2025

Dr. Jawaharlal Bhukya
Assistant Professor,
Dept. of Electrical Engineering,
VNIT, Nagpur

Acknowledgement

I would like to express my sincere gratitude to my supervisor, Dr. Jawaharlal Bhukya. His continuous support, guidance and encouragement throughout this research have been extremely invaluable. His perspectives and feedback were instrumental in the shaping of this thesis.

I am also very much grateful to the faculty and staff of the Department of Electrical Engineering, VNIT, Nagpur, for the provision of a conducive research environment and necessary resources.

Special thanks to all my peers, friends and seniors for their unwavering assistance during challenging times. Lastly, I am thankful to my parents for being there by my side and pushing me throughout my academic journey.

Rishav Dutta

VNIT, Nagpur

ABSTRACT

In recent years, the rapid integration of wind energy systems has outpaced other renewable sources, introducing new operational challenges. Among these challenges, Sub-Synchronous Oscillations, particularly Sub-Synchronous Resonance (SSR), have emerged as a serious concern, with cases reported in regions such as the United States, China, and Australia. Despite this, the manifestation of SSR in practical WTGs, especially those based on Doubly-Fed Induction Generators (DFIGs), remains insufficiently addressed in existing literature. This thesis seeks to address this gap by presenting a comprehensive study focused on the modelling and mitigation of SSR in DFIG-based wind power plants. Specifically, three Supplementary Damping Controllers (SDCs) are proposed and strategically embedded within the inner current regulation loops (ICRLs) of the Grid Side Converter and Rotor Side Converter (RSC). Among them, one controller based on Virtual Inertia (VISDC), designed to emulate the inertial response of synchronous generators, placed in RSC, demonstrates superior damping performance. The effectiveness of the proposed controllers is evaluated under varying SC levels, a known trigger for SSR, and further validated under the most severe fault condition, a three-phase symmetrical fault. The simulation results confirm effective suppression of unwanted oscillations and highlight the system's fault ride-through capability. Additionally, the real-time-based experimentations on the OPAL-RT simulator setup (OP4610XG) exhibit a near-identical dynamic response to the simulations, thereby validating the feasibility and robustness of the proposed control strategy. The findings provide a foundation for future work on adaptive and intelligent control methods for mitigating SSR in large-scale wind integration.

LIST OF FIGURES

Figure 2-1. Types of SSOs 12
Figure 3-1. Schematic Diagram of Major WTG Components of a Modern HAWT 22
Figure 3-2. Type A Fixed-Speed WT equipped with SCIG 23
Figure 3-3. Type B WT Featuring Limited Variable-Speed and WRIG 24
Figure 3-4. Type C WT Featuring Variable-Speed and DFIG with Partial-Scale PEC 24
Figure 3-5. Type D Variable-Speed with Full Scale PEC with PMSG/WRSG 25
Figure 3-6. Power flow in DFIG during Sub-Synchronous Mode of Operation 27
Figure 3-7. Power flow in DFIG during Super-Synchronous Mode of Operation 27
Figure 4-1. Block diagram of the DFIG system with integration of the grid 34
Figure 5-1. Control Scheme for RSC 50
Figure 5-2. Control Scheme for GSC 51
Figure 5-3. Proposed Control Scheme for GSC 52
Figure 5-4. Proposed SDC Scheme for RSC 53
Figure 5-5. VISDC Scheme Proposed for RSC 54
Figure 5-6. Flow chart of the control scheme for the DFIG-based WTG, along with the placements of proposed controllers SDC and VISDC 54
Figure 6-1. Experimental RT-Lab Configuration Using OPAL-RT for Real-Time Verification of the Proposed System 58
Figure 6-2. Schematic of DFIG-WPS 59
Figure 6-3. Active power in pu of DFIG response subject to varying compensation levels 62
Figure 6-4. Reactive power in pu of DFIG response subject to varying compensation levels 63
Figure 6-5. Electromagnetic torque in pu of DFIG response subject to varying compensation levels 63
Figure 6-6. Phase ‘A’ current magnitude in pu of DFIG response subject to varying compensation levels 64
Figure 6-7. Phase A voltage magnitude (in pu) of DFIG response subject to varying compensation level 64
Figure 6-8. Phase A voltage magnitude in pu of DFIG response subject to LLLG fault 69
Figure 6-9. Phase A current magnitude in pu of DFIG response subject to LLLG fault 69
Figure 6-10. Active power in pu of DFIG response subject to LLLG fault 70
Figure 6-11. Reactive power in pu of DFIG response subject to LLLG fault 70
Figure 6-12. Electromagnetic torque in pu of DFIG response subject to LLLG fault 71
Figure 6-13. Pole Plot of Eigenvalues of SSR Analysis 78
Figure 6-14. Pole Plot of Eigenvalues of Transient Analysis 78

LIST OF TABLES

Table 3-1. Classification of WTG Types.....25
Table 5-1. Tuned PI Controller Gains for RSC, GSC, and VISDC Schemes 55
Table 6-1. Enhanced Unified Comparative Analysis & Control Strategy Progression for Varying Compensation Levels 65
Table 6-2. Comparative Case-Wise Controller Performance Evaluation for Transient Analysis.....72
Table 6-3. Key Transient response parameters subject to LLLG fault 73
Table 6-4. Eigenvalues under different test conditions.....79

NOMENCLATURE

ACRONYMS

AOIC	Analog Output Interface Card
CIG	Converter-Interfaced Generators
DFIG	Doubly-Fed Induction Generators
DR	Damping Ratio
ERCOT	Electric Reliability Council of Texas
FACTS	Flexible AC Transmission System
FOO	Frequency of Oscillation
FRT	Fault Ride Through
GB	Gearbox
GSC	Grid Side Converter
GWEC	Global Wind Energy Council
HAWT	Horizontal Axis Wind Turbine
HIL	Hardware In Loop
HV	High Voltage
IBR	Inverter-Based Resources
IEEE FBM	IEEE First Benchmark Model
IG	Induction Generator
IGBT	Insulated-Gate Bipolar Transistor
IGE	Induction Generator Effect
IRENA	International Renewable Energy Agency
KE	Kinetic Energy
LHP	Left Half Plane
LLC-SDC	Lead-Lag Compensator-based Supplementary Damping Controller
LSC	Load Side Converter
LVRT	Low-Voltage Ride-Through
MDO	Mixed Domain Oscilloscope
MSC	Machine Side Converter
NC-SDC	Nonlinear Control theory-Supplementary Damping Controller
OSF-SDC	Observer and State Feedback Supplementary Damping Controller
PCC	Point of Common Coupling

PEC	Power Electronics Converters
PD	Proportional Derivative
PI	Proportional Integral
PMSG	Permanent Magnet Synchronous Generator
PS	Power Systems
PSS	Power System Stabilizers
PWM	Pulse Width Modulation
RES	Renewable Energy Sources
RHP	Right Half Plane
RoCoF	Rates of Change of Frequency
RPM	Revolutions Per Minute
RSC	Rotor Side Converter
SC	Series Capacitive Compensation
SC_Console	Subsystem Console (OPAL-RT)
SCIG	Squirrel Cage Induction Generator
SDC	Supplementary Damping Controller
SFOCS	Stator Flux Oriented Control Scheme
SM_Master	Subsystem Master (OPAL-RT)
SSI	Sub-Synchronous Interactions
SSO	Sub-Synchronous Oscillations
SSR	Sub-Synchronous Resonance
SSSC	Static Synchronous Series Compensators
SVC	Static Var Compensators
TA	Torque Amplification
TCSC	Thyristor-Controlled Series Capacitors
TI	Torsional Interactions
TL	Transmission Lines
TN	Transmission Network
TSR	Tip Speed Ratio
VI	Virtual Inertia
VISDC	Virtual Inertia-based Supplementary Damping Controller
VSC	Voltage Source Converter
WE	Wind Energy

WECS	Wind Energy Conversion Systems
WF	Wind Farms
WPP	Wind Power Plant
WRIG	Wound Rotor Induction Generator
WRSG	Wound Rotor Synchronous Generator
WT	Wind Turbines
WTG	Wind Turbine Generators
WWEA	World Wind Energy Association

LIST OF PUBLICATIONS

[1] Rishav Dutta and Jawaharlal Bhukya, 'Impact of Compensation Level on SSR Mitigation in Grid-Connected DFIG Wind Power Plants', 5th IEEE International Conference on Sustainable Energy and Future Electric Transportation (IEEE SeFet 2025). (Accepted)

[2] Rishav Dutta and Jawaharlal Bhukya, 'Dynamic Stability and Sub-Synchronous Resonance Suppression in Wind-Integrated Grids Using Rotor-Side Virtual Inertia Control', International Journal of Ambient Energy. (Under review)

TABLE OF CONTENTS

Abstract i
List of Figures ii
List of Tables iii
Nomenclature iv
List of Publications vii
CHAPTER 1. INTRODUCTION 1
1.1 . Overview 1
1.2. Motivation of the Thesis 3
1.2.1. Radial Connection Topology and System Vulnerabilities 3
1.2.2. SSR: A Critical Technical Challenge 3
1.2.3. The Need for Practical and Robust Control Solutions 4
1.2.4. Advancing SDC: The Role of PI and VI 4
1.2.5. Validation and Practical Significance 4
1.2.6. Summary 5
1.3. Research Methodology and Contribution of the Thesis 5
1.3.1. PI Controllers and Virtual Inertia: Suitability and Practical Considerations for Modern Wind Power Applications 5
1.3.2. System Modelling and State-Space Analysis 6
1.3.3. Eigenvalue Analysis and SSR Mode Interpretation 7
1.3.4. Best Practices for Controller Deployment in WE Systems 8
1.4. Thesis Outline 9
CHAPTER 2. LITERATURE REVIEW 11
2.1 . Introduction 11
2.2 . Types of SSR 13
2.2.1. Occurrence condition for Steady State SSR 14
2.2.2. Occurrence condition of Transient SSR 15
2.3. Existing Methods for SSR Suppression 15
2.3.1. FACTS-Based Mitigation Techniques 16
2.3.2. Power System Stabilizers (PSS) 16
2.3.3. Supplementary Damping Controllers 16
2.3.4. Importance of Virtual Inertia in Power Systems 17
2.3.5. Key Insights from Literature 18
CHAPTER 3. WIND ENERGY CONVERSION SYSTEMS 19
3.1. Introduction 19

3.2. WECS 19
3.2.1. WT Components 20
3.2.2. WTG Types: Dependence on Control Methods and Generator Technology ..22
3.2.3. Type A: Fixed-Speed WTGs with Squirrel Cage Induction Generators (SCIGs) 23
3.2.4. Type B: Limited Variable-Speed WTGs with Wound Rotor Induction Generators (WRIGs) 23
3.2.5. Type C: Variable-Speed WTGs with DFIGs 24
3.2.6. Type D: Variable-Speed WTGs with Permanent Magnet Synchronous Generators (PMSGs) or Wound Rotor Synchronous Generators (WRSGs) 24
3.3. DFIG: Architecture and Operating Principles 25
3.3.1. Basic Structure and Grid Interface 26
3.3.2. Operating Principles of DFIG 26
3.3.3. Back-to-Back Converter: RSC and GSC Roles 27
3.3.4. Slip Power Recovery and Energy Conversion Efficiency 28
3.3.5. Betz Limit and Theoretical Power Extraction 29
3.3.5. DFIG's Unique Characteristics Conducive to SSR 29
3.3.6. DFIG's Vulnerability to SSR 30
3.3.7. SSR Mitigation Techniques and Optimal Controller Placement Locations 30
3.4. Inertia Deficiency in IBRs and Role of VI in Grid Stability 32
CHAPTER 4. SYSTEM MODELLING AND STATE-SPACE ANALYSIS 34
4.1. Design of Wind PS Model under study 34
4.1.1. Expression for the Power of WT 35
4.1.2. Expression for Torque 35
4.1.3. Expression for the GB ratio 36
4.1.4. Expression for the Mechanical Equation of the whole system 36
4.2. Expressions for Stator and Rotor Powers 37
4.2.1. Torque Conversion Dynamics in a Two-Mass shaft DFIG system 38
4.2.2. Modelling of DC-Link Capacitor 39
4.2.3. Expressions for RSC, stator-side, and GSC loops 39
4.2.4. Modelling of the Transmission System 40
4.3. Final mathematical equations for PS with SC DFIG-WF 40
4.3.1. Expression for the Power Flow between the WF 41
4.3.2. Determination of Power Rating for DFIG 42
4.4. Design of DC Link Voltage 43
4.5. Design of Transformers and VSC Rating 43

4.6. Linearized System Modelling and Eigenvalue Analysis for System Stability Assessment....45
CHAPTER 5. DESIGN OF THE CONTROLLER....49
5.1. Comparative Analysis of PI-Based and VI-Based SDCs for SSR Mitigation in DFIG-WPPs....49
5.2. Control Scheme for RSC....49
5.3. Control Scheme of GSC....51
5.4. Proposed Supplementary Damping Control Scheme....52
5.4.1. Controller Parameter Selection and Tuning....55
5.4.2. Controller Tuning Methodology Using Modified Ziegler–Nichols Approach....56
CHAPTER 6. RESULTS AND DISCUSSIONS....57
6.1. Real-time validation using OPAL-RT....57
6.2. System under study....58
6.3. Varying Compensation Levels:....59
6.4. Transient Analysis....66
6.4.1. Performance Evaluation of System Parameters Under Severe Grid Faults (LLLG)....72
6.5. Eigenvalue Analysis....73
6.5.1. SSR: Case-wise comparative Analysis....74
6.5.2. Transient Analysis: Case-wise comparative Analysis....76
CHAPTER 7. CONCLUSIONS AND FUTURE WORK....80
7.1. Conclusion....80
7.2. Future Scope....81
ANNEXURE....82
REFERENCES....83

CHAPTER 1. INTRODUCTION

1.1. Overview

With the world experiencing rapid urbanization, industrial growth, and rising living standards, the demand for clean and sustainable electrical energy is at an all-time high [1]. Concerns surrounding the continued use of fossil fuels, such as the emission of greenhouse gases, environmental degradation, and the mounting carbon footprint [2], have accelerated the global transition towards Renewable Energy Sources (RESs). Among these, Wind Energy (WE) has emerged as a particularly promising and cost-effective alternative. Technological improvements and supportive policy frameworks have resulted in significant WE deployments across continents, with wind power now contributing over 2.5% of the global electricity demand [3], [4]. According to the Global Wind Energy Council (GWEC), World Wind Energy Association (WWEA), and the International Renewable Energy Agency (IRENA), the global installed WE capacity surpassed 1.136 TW as of May 2025, with a record 117 GW added in 2024. This capacity is projected to triple by 2030 and increase nearly tenfold by mid-century, underscoring the growing reliance on WE in modern Power Systems (PSs) [5].

A large portion of these Wind Farms (WFs), especially offshore installations, are located in remote areas offering stronger and more consistent wind profiles. However, their geographic distance from load centres necessitates the long-distance transmission of generated power. Conventional transmission infrastructure often proves insufficient for these requirements, as the inductive reactance of High Voltage (HV) Transmission Lines (TLs) increases with distance, impairing power transfer capability and system efficiency. To address this, utilities have increasingly adopted Series Capacitive Compensation (SC) as a cost-effective solution [6]. SC provides reactive power support, improves voltage profiles, enhances power flow stability, and increases the TL's power transfer limit, all without requiring the extensive capital investment needed to construct new TLs [7].

Despite its numerous advantages, SC introduces dynamic interactions within the PS, particularly when interfaced with Power Electronic Converters (PECs) used in Wind Turbine Generators (WTGs), such as those in Doubly-Fed Induction Generators (DFIGs). These interactions may excite resonant modes between the mechanical and electrical

components of the system, especially under partial SC scenarios. This phenomenon, known as Sub-Synchronous Resonance (SSR), can lead to Torsional Interactions (TI) and dangerous oscillations at frequencies lower than the nominal grid frequency [8]. SSR is not exclusive to thermal generating stations but is increasingly observed in modern wind-integrated PSs [7], raising significant concerns about operational stability and equipment lifespan.

The DFIG topology, characterised by a partially-rated back-to-back PEC, offers advantages in terms of independent active and reactive power control, efficient operation under varying wind speeds, and reduced converter cost. However, its interaction with SC-TLs creates an operational vulnerability to SSR, especially during grid disturbances or fault conditions. To address these dynamic challenges, this thesis investigates converter-level damping strategies aimed at mitigating SSR in DFIG-based Wind Power Plants (DFIG-WPPs). Supplementary Damping Controllers (SDCs), such as those based on Proportional Integral (PI) regulation and Virtual Inertia (VI) concepts, are proposed and embedded directly into the Inner Current Regulation Loops (ICRLs) of the DFIG control system. These controllers are designed to actively modulate the output of the Rotor Side Converter (RSC) and Grid Side Converter (GSC) to suppress oscillations in real time. These approaches enable effective real-time mitigation of Sub-Synchronous Oscillations (SSOs), contributing to enhanced stability and reliable operation of wind-integrated PSs.

The analytical backbone of this research is built on both time-domain simulations and eigenvalue-based analysis. Time-domain studies help evaluate transient responses to grid disturbances, while eigenvalue analysis enables theoretical validation of system stability margins and oscillatory mode damping. Additionally, detailed state-space modelling of the DFIG system, the SC Transmission Network (TN), and their interconnections has been performed to support controller design and stability analysis. A comprehensive test bench based on the IEEE First Benchmark Model (IEEE FBM) is developed in MATLAB/Simulink for simulation studies.

To ensure real-world applicability, the proposed control schemes are further validated through experiments conducted on the OPAL-RT OP4610XG real-time simulator. This platform enables rapid prototyping and testing under realistic conditions, including fault scenarios and varying SC levels, thereby bridging the gap between simulation and practical deployment.

In summary, this thesis contributes to the advancement of wind-integrated PSs by focusing on real-time, converter-level damping mechanisms that are robust against SSR phenomena. Advanced control strategies are developed and rigorously validated through detailed modelling, simulation, and OPAL-RT-based experimental studies. Special emphasis is placed on evaluating the effectiveness of the proposed controllers under both normal and fault conditions, thereby demonstrating their capability to enhance the stability and reliability of SC-TNs. The subsequent chapters present the theoretical foundations, controller design methodologies, and comprehensive evaluation results that collectively support the integration of large-scale wind power into modern electrical grids.

1.2. Motivation of the Thesis

The accelerating global transition toward sustainable energy has placed wind power at the forefront of modern electrical grids, with technological advancements and supportive policies driving rapid deployment across continents. As WE's share of the electricity mix grows, particularly through the use of DFIG-WTGs, the technical and operational challenges associated with large-scale integration have become increasingly complex. Among the various WTG technologies, DFIGs are widely favoured for their ability to operate efficiently over a broad range of wind speeds, provide independent control of active and reactive power, and meet evolving grid code requirements [9], [10].

1.2.1. Radial Connection Topology and System Vulnerabilities

Many DFIG-WFs use a radial connection, where several DFIG units are linked together and connected to the grid at a single point, known as the Point of Common Coupling (PCC). This setup is affordable and easy to build, but it also creates some unique risks for the whole system. If one DFIG unit shuts down, whether because of a fault, a protection trip, or routine maintenance, the electrical conditions for the remaining units change. In particular, the line capacitance seen by the other DFIGs increases, which can make resonance problems worse and even destabilize the system. These faults can happen for many reasons, such as converter failures, grid issues, insulation problems, or severe weather. That's why strong control and protection strategies are so important.

1.2.2. SSR: A Critical Technical Challenge

One of the biggest technical challenges here is SSR, which is a major concern when WFs connect to the grid using SC TLs. SSR happens because of complicated interactions between the grid and the moving parts of Wind Turbines (WTs). This

can cause harmful vibrations, put extra stress on the equipment, and in serious cases, even damage the turbines or cause them to lose synchronism with the grid. The risk of SSR is even higher in radial DFIG setups, especially during faults or changing conditions, when sudden shifts in the system or SC can make these resonance problems worse.

1.2.3. The Need for Practical and Robust Control Solutions

Despite extensive research, many SSR mitigation techniques remain theoretical or lack thorough validation under realistic fault conditions. Therefore, the industry requires solutions that are both effective and practical for large-scale deployment. PI controllers are widely used due to their simplicity, ease of tuning, low computational demands, and proven reliability. Their ability to robustly regulate active and reactive power makes them well-suited for the dynamic environment of wind-integrated grids.

1.2.4. Advancing SDC: The Role of PI and VI

This thesis develops and evaluates three PI-based SDCs at different locations for mitigating SSR in DFIG-WPPs, with a comprehensive assessment under both steady-state and fault conditions. While one controller integrates VI concepts to enhance dynamic response, the primary emphasis is on the practical advantages of PI-based strategies. The potential of VI to improve system resilience by emulating the inertial behaviour of synchronous machines will be discussed further in the literature review.

1.2.5. Validation and Practical Significance

To ensure both theoretical soundness and real-world applicability, the proposed solutions are validated using MATLAB/Simulink, OPAL-RT real-time simulation, and eigenvalue analysis. The growing use of SC in long-distance grids highlights the practical value of this work, as utilities aim to boost power transfer without major infrastructure costs. As WE penetration rises, reliable integration, especially under faults or changing grid conditions, remains essential.

1.2.6. Summary

In summary, this thesis is motivated by the need for practical solutions to SSR challenges in wind-integrated PSs. By developing and validating PI-based damping controllers, the work aims to enhance the secure and reliable integration of WE, supporting the sustainability of future power grids.

1.3. Research Methodology and Contribution of the Thesis

The increasing demand for RESs, particularly wind power, has driven the widespread adoption of DFIG-WTs. DFIGs offer several advantages over other generator technologies, making them the preferred choice for modern WE systems. Notably, DFIGs enable independent control of active and reactive power, corresponding to torque and flux, which allows for flexible grid support and efficient energy extraction across a wide range of wind speeds. Additionally, DFIG-WPPs require PECs rated at only about $1/3^{rd}$ of the generator capacity, significantly reducing both the cost and complexity of the overall system compared to fully-rated converter solutions. These features, combined with their proven operational reliability and ability to meet evolving grid code requirements, have led to the increasing deployment of DFIGs in utility-scale WFs worldwide.

1.3.1. PI Controllers and Virtual Inertia: Suitability and Practical Considerations for Modern Wind Power Applications

The selection of PI controllers for this work is motivated by their proven practicality in industrial and PS applications. PI controllers are valued for their simplicity, robustness, and ease of implementation, allowing seamless integration into existing converter architectures without demanding significant computational resources or specialized operator training. Their straightforward tuning process and consistent performance under varying operating conditions make them particularly well-suited for addressing challenges such as SSR in DFIG-WFs.

This thesis further innovates by integrating VISDC into one of the PI-based SDCs. VI enables DFIGs to emulate the inertial response of synchronous generators, enhancing grid resilience during sudden disturbances like faults or load changes. By embedding VISDC within the RSC, this work bridges the gap between conventional damping control and modern grid requirements for inertia support in renewable-dominated PSs.

1.3.2. System Modelling and State-Space Analysis

A robust and accurate system model is essential for analyzing dynamic behaviour and designing effective controllers. This section provides a brief overview of the modelling approaches used for the mechanical dynamics of WTs, the electrical characteristics of DFIGs, and the SC-TL. A concise introduction to eigenvalue analysis is also included, with detailed results presented in subsequent chapters.

1.3.2.1. Mechanical Modelling of Wind Turbines

The mechanical subsystem of the WT is modelled to accurately capture the conversion of WE into mechanical torque and its subsequent transmission to the generator. The aerodynamic model considers the relationship between wind speed, rotor blade characteristics, and the resulting mechanical power. Shaft dynamics are represented using a two-mass or multi-mass model, accounting for the flexibility and torsional oscillations between the turbine rotor and the generator shaft. This detailed mechanical modelling is crucial for analyzing low-frequency oscillations and understanding the system's response to grid disturbances and control actions.

1.3.2.2. Electrical Modelling of DFIG

The electrical behaviour of the DFIG is described using a set of nonlinear differential equations in the synchronously rotating reference frame. The model incorporates stator and rotor circuits, with dynamic equations capturing the interactions between stator and rotor flux linkages, currents, and voltages. Converter controls for both RSC and GSC are included, enabling independent regulation of active and reactive power. This comprehensive electrical model forms the foundation for implementing advanced control strategies, such as supplementary damping and VI, and is essential for investigating the system's dynamic performance under various operating scenarios.

1.3.2.3. SC-TL Modelling

The TL connecting the WF to the grid is modelled as a SC network, incorporating line resistance, inductance, and variable series capacitance. This representation captures the essential dynamics that give rise to SSR phenomena, particularly under different levels of SC. Accurate modelling of the TL is vital for

assessing the impact of compensation on system stability and for designing controllers that can effectively mitigate SSR-related risks.

1.3.2.4. State-Space Formulation and Linearization

To facilitate small-signal stability analysis and controller design, the combined nonlinear model of the WT, DFIG, and TL is linearized around a specific chosen operating point. The state-space representation is derived using MATLAB's Model Linearizer tool, resulting in a set of linear differential equations that describe the system's behaviour in the vicinity of the operating point. This linearized model enables the application of eigenvalue analysis and forms the basis for evaluating the effectiveness of different control strategies in enhancing system stability.

1.3.2.5. Role of Eigenvalue Analysis in Stability Assessment

Eigenvalue analysis is a key method for assessing small-signal stability in PSs. By evaluating the eigenvalues of the linearized state-space model, critical modes linked to SSR and other dynamics can be identified. Their position in the complex plane reveals stability margins and damping characteristics. Detailed analysis and interpretation are presented in later chapters.

1.3.3. Eigenvalue Analysis and SSR Mode Interpretation

Eigenvalue analysis is employed to:

1.3.3.1. Identify SSR Modes

Eigenvalue analysis is used to pinpoint the frequencies of oscillations and corresponding damping ratios of both torsional and electrical resonance modes in the system. This helps in recognizing which modes are susceptible to SSR. Accurate identification is essential for targeted controller design and mitigation strategies.

1.3.3.2. Study Compensation Impact

By varying the SC level from 2% (almost nil) to 60%, the migration of critical eigenvalues in the complex plane is observed. This analysis reveals how increased compensation can shift modes closer to instability and alter system damping. Such insights guide the safe selection of compensation levels.

1.3.3.3. Fault Severity Assessment

System stability is evaluated during a three-phase line-to-ground (LLLG) fault, which represents the most severe symmetrical disturbance. The analysis highlights how such faults can trigger or worsen SSR by causing transient overvoltages and current surges. This assessment is crucial for validating controller robustness under extreme conditions.

1.3.4. Best Practices for Controller Deployment in WE Systems

The findings of this thesis suggest several considerations that may inform the effective deployment and operation of DFIG-based WE systems. These insights pertain to controller placement, VI integration, SC practices, and the role of software-based real-time validation in modern wind power applications.

1.3.4.1. Optimal SDC Placement

For effective and economical SSR mitigation, it is advisable to prioritize the implementation of SDCs at the RSC. The results indicate that RSC-based SDCs, and particularly the proposed VISDC, offer substantial damping performance while minimizing system complexity. This approach reduces the need for additional control hardware and simplifies integration with existing converter architectures.

1.3.4.2. Virtual Inertia Deployment

The integration of VISDC is especially beneficial in PSs with low inherent inertia, which are increasingly common as renewable penetration rises. By enabling DFIGs to emulate the inertial response of synchronous generators, VISDC enhances grid frequency stability during disturbances. It is recommended to deploy VISDC in regions or networks where conventional inertia is insufficient, thereby supporting secure and resilient grid operation.

1.3.4.3. SC Limits

Analysis in this thesis demonstrates that higher levels of SC, while beneficial for power transfer capability, can significantly increase the risk of SSR and reduce system damping. It is therefore recommended to restrict SC to no more than 60% of the line reactance unless advanced damping controls, such as VISDC, are actively implemented. This guideline helps maintain a balance between transmission efficiency and system stability.

1.3.4.4. Controller Validation via Real-Time Performance Evaluation

Before field deployment, it is essential to validate control strategies under realistic operating scenarios. In this work, software-based real-time simulation was performed using the OPAL-RT platform, with communication established between the simulation environment and the controller. System responses were captured and analyzed using the Tektronix MDO3000 oscilloscope, providing high-fidelity insight into controller performance and dynamic behaviour. This approach enables thorough pre-deployment testing of control algorithms, ensuring their effectiveness and reliability in actual grid conditions without the need for full hardware-in-the-loop (HIL) setups.

Collectively, these guidelines are intended to facilitate the practical adoption of advanced damping and inertia control strategies in modern WPPs, supporting the continued integration of renewable energy while maintaining grid stability and reliability.

1.4. Thesis Outline

The thesis is organized as follows:

Chapter 1 introduces the research context, objectives, and significance of DFIG-based WTGs in modern PSs. It presents the problem statement, research motivation, and an overview of the thesis structure.

Chapter 2 reviews the relevant literature on DFIG-WPPs, SSR phenomena, and existing SDC strategies. Key research gaps motivating this study are identified.

Chapter 3 provides a comprehensive overview of Wind Energy Conversion Systems (WECS), emphasizing the operational principles of DFIGs. It covers the major components of WTs, classification into Types A–D based on generator and control technology, and explores the DFIG's unique characteristics, particularly its vulnerability to SSR.

Chapter 4 presents system modelling and state-space analysis, covering key components like the DFIG, converters, and grid interface.

Chapter 5 presents the design and implementation of the controller. The control strategies are described in the context of mitigating SSR in DFIG-WFs.

Chapter 6 presents the comparative analysis of the different cases under varying compensation levels and fault conditions, followed by theoretical validation using eigenvalue analysis. Validation using OPAL-RT-based real-time testing is performed.

Chapter 7 presents the conclusions of the work and outlines the prospective future avenues.

The next chapter presents a detailed literature review, highlighting key contributions from past research and offering deeper insights into the phenomenon of SSR in wind-integrated PSs.

CHAPTER 2. LITERATURE REVIEW

2.1. Introduction

With ever-increasing demand for energy each day, and increasing carbon footprint, the world is moving towards rapid adoption of alternative sources for generation, such as solar, wind, geothermal, tidal, etc. Amongst all, wind has proven to be immensely cost-effective and efficient, with rapid penetration of a large number of WE systems into the PS. Sub-Synchronous Interactions (SSI), also known as SSO, are a problem that is detrimental to the operation of generators and overall grid-connected PSs. SSR (a type of SSI) is a serious problem in WPPs that occurs in DFIGs when connected with SC lines. This occurs when the mechanical vibrations of the rotating parts of the DFIG-WTG match the electrical frequency of the PS, and the exchange of energy takes place typically below the nominal frequency of the grid. This can cause severe damage to equipment. In WFs using DFIGs, the problem can worsen because of how the generator control system interacts with certain types of power TLs. SSR can cause harmful vibrations in the turbine and generator shaft, make the electrical system unstable, and even lead to catastrophic equipment failures if not addressed. To prevent or reduce SSR in WPPs, researchers and engineers have developed several solutions. Every event is seen to have the following 2 characteristics in common: (i) interaction of DFIG-WPPs with a SC grid, resulting in the occurrence of the SSO; (ii) the resulting oscillations do not have any fixed frequencies and can end up building and growing rapidly. SSO and SSI are used alternately and more or less mean the same. They are the umbrella under which various other phenomenon comes. A better visual understanding can be gained from Figure 2-1. Extensive tests to check the system under varying conditions, employing various strategies, have been carried out to mitigate SSO.

It is standard practice to locate WFs in remote areas, particularly offshore, where strong and consistent wind patterns can maximize energy capture. However, this often places WFs far from the end consumers. Owing to this, the WF-generated power needs to be transmitted over very long distances. The inductive reactance of the TLs is in direct relation to their length, thereby limiting the power that can be transmitted over extremely long TLs and reducing system efficiency. To overcome this issue, the generating stations have been pushed to obtain the highest efficiency by employing relatively low-cost series

capacitive repayment (i.e. compensation) [6], instead of continuous infrastructural restructuring of extant power TLs [7]. Inserting series SC into TLs offsets inductive reactance, thereby enhancing the power transfer capability and overall system stability of the transmission corridor. Furthermore, the insertion of reactive power elements into TLs (i.e. SC) boosts power transfer capability, reduces the electrical length, improves the voltage profile, optimizes reactive power regulation, enhances the system's dynamic stability, and facilitates load-sharing capability between parallel cables of the transmission corridors (esp., under radial connection). Despite all the mentioned benefits, the series capacitors exchange energy (i.e. resonate) with the WTG and their PECs, causing TI and resulting in WTG shaft fatigue [8], despite the level of SC being very low. These interactions predominantly can be observed at one or multiple frequencies of the electrical or mechanical parts of the WTG, primarily lower than the grid's system frequency, which is known as SSR. This SSR is not only seen in newer WTG-PSs but also in existing conventional thermal power plants. Due to this, system parameters can be affected severely, causing the system to become unstable [7].

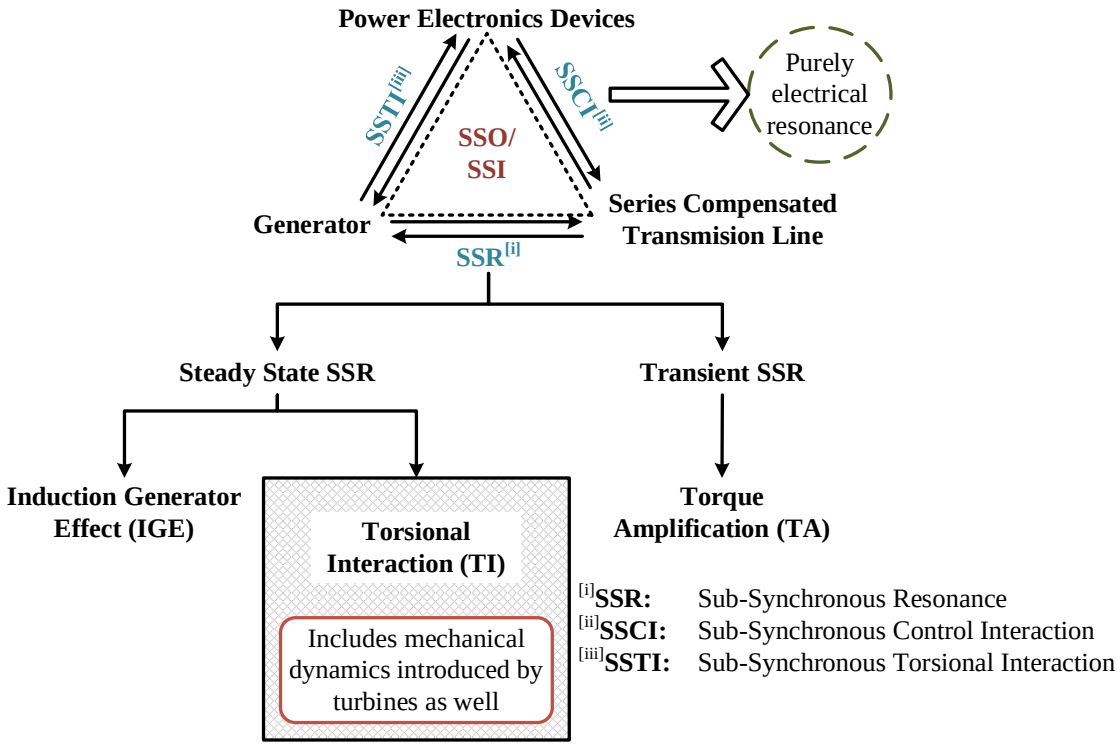

Figure 2-1. Types of SSOs

Interactions occur between various components, and separate names are given accordingly. They could be between the generator and the PECs, or between the generator

and the SC TL, or maybe between the PECs and the SC TL. Among European and North American countries, DFIG-WTGs are the most dominant. They have gained significant attention from the electrical power generation industries, owing to the advantages such as the integration of independent power control [11], reduced rating of the converters (as the converters handle only slip power), high energy efficiency, lower power losses and reduced acoustic noise. Additionally, DFIG WTGs are highly suitable for achieving peak power extraction, especially under varying wind conditions [12]. In [13], it has been reported that the SSR existing between DFIG-based WFs and SC grids was recorded at the Electric Reliability Council of Texas (ERCOT) in the USA (2009), the state of Minnesota, USA (2007) and Guyuan, Hebei Province of China (2012). Following the incidents, extensive research into the SSR problem in DFIG-based WFs coupled with SC PSs was conducted. [14] indicates that DFIGs are more prone to SSR in SC systems compared to fixed-speed WTG and full-scale back-to-back PEC (i.e. AC/DC/AC) connected WTG. DFIG-based WTs are highly susceptible to SSR, leading to unstable oscillations and rapid amplitude escalation. Interactions with PECs and SC systems complicate stability. Grid integration challenges arise due to nonlinear dynamics, requiring advanced control strategies. Historical SSR incidents highlight the need for robust damping solutions to ensure reliable PS operation.

In brief, SSR arises from the interaction between the multi-machine dynamics of DFIG-WFs and SC-TLs. These SCs are commonly installed to enhance the power transfer capability of transmission corridors, particularly when WFs are situated far from major load centers, as is typically the case. However, such compensation can inadvertently create conditions conducive to SSR, posing stability challenges for the integrated PS.

2.2. Types of SSR

A generic formula for SSR is given in the equation (1) :

$$f_{SSR} = f_{nom}\sqrt{\frac{X_{sc}}{X_{tot}}} \tag{1}$$

Where f_{SSR} denotes the resonant frequency, f_{nom} denotes the grid's nominal/fundamental/synchronous frequency; X_{sc} represents the reactance of the series-connected capacitor; X_{tot} is the total reactance available in the system (inclusive of the generator, TL, and transformer of the system), i.e. $X_{tot} = X_{gen} + X_{TL} + X_{xfmr}$.

IEEE categorizes SSR into 2 categories: (a) Steady State SSR and (b) Transient SSR. Steady State SSR is further divided into 2 conditions: (*a.i*) IGE and (*a.ii*) TI. The occurrence conditions of both the categories are elaborated further:

2.2.1. Occurrence condition for Steady State SSR

The RSC gets blocked during the operation of the crowbar, and since there is no flow of current from the RSC, there is no flow of power through the GSC, which essentially becomes open-circuited. This makes the Induction Generator (IG) connect directly to the SC grid. The rigidity of the rotor is responsible for IGE. The activation of the crowbar primarily takes place under the condition of a fault or any other disturbance. During this, a sub-synchronous frequency current (I_{sub}) via the generator stator might align (resonate) with the reactance of the TL and excite the SC system. Torque in the rotor and a voltage in the stator are the outcomes of this current. The voltage that is induced in the stator might end up getting amplified, if at all, by the net resistance of the rotor that corresponds to the I_{sub} seen from the generator becomes negative. This condition is known as the Induction Generator Effect (IGE) [15]. IGE only takes place due to the electrical machines available in the network and doesn't involve the generator-turbine mechanism [16]. The slip at a sub-synchronous frequency is defined by the equation (2) [16], [17]:

$$s_{SSR} = \left(f_{SSR} - \frac{f_{rot}}{f_{SSR}} \right) \tag{2}$$

where f_{rot} represents the rotor frequency generated due to its rotation.

Net rotor resistance at the above sub-synchronous frequency is given by the equation (3) [16]:

$$R_{net} = \frac{R}{s_{SSR}} \tag{3}$$

In equation (2), if $f_{SSR} < f_{rot}$, $R_{net} < 0$ (becomes negative), leading to overdamped oscillation of voltage and current [17].

Under any circumstance, if at all, the complement of the sub-synchronous frequency ($f_{nom} - f_{SSR}$) falls close to/ matches either with the natural mechanical torsional mode frequencies, then the torque induced in the rotor (τ_{rot}) gets amplified, leading to torsional oscillations in the rotor. This is called TI [3].

2.2.2. Occurrence condition of Transient SSR

During transient conditions such as switching actions or faults, a sub-synchronous torque gets created in the rotor owing to the disturbance caused and subsequent sudden change in current. If any of the torsional mode frequencies of the system coincide with the complement of the above torque, the net torque gets quickly amplified. This is known as torsional amplification (TA) [3].

In this work, particular emphasis is placed on the IGE, as it represents a critical SSR mechanism in DFIG-WFs interfaced with SC-TLs. The IGE is especially significant because it can lead to sustained oscillations and stability challenges under certain network conditions, particularly during transient disturbances or faults [18], [19], [20]. By focusing on IGE, this study addresses one of the most relevant and practically observed SSR phenomena in modern wind power integration scenarios.

2.3. Existing Methods for SSR Suppression

Extensive tests to check the system under varying conditions, such as wind speeds, compensation levels, 3-phase faults, load types, etc., employing various strategies have been carried out to mitigate SSO [16]. Among the proposed solutions, the 3 prominent ones are: (i) Optimal tuning of control parameters [21]; (ii) Reactive power management [22]; (iii) Supplementary Damping Controller (SDC) deployment [23]. Unlike the third method, methods one and two exhibit a limited adjustment range; thus, employing SDCs for SSR mitigation constitutes the most promising strategy. Inspired by the design of traditional PS Stabilisers (PSSs) featuring cascaded filters, gains, and phase compensation [21], the development of early-stage SDCs began around the year 2010. [21] refers to this kind of SDC as a Lead-Lag Compensator-based SDC (LLC-SDC). Based on research since 2015, the SDC's design can be classified into 4 groups, which are based on (a) Observer and State Feedback control (OSF-SDC) [22]; (b) Virtual Impedance/Admittance control (VIA-SDC) [24]; (c) Nonlinear Control theory (NC-SDC) [11], [25]; and (d) Auxiliary devices control (Aux-SDC) [26]. Each of the SDCs has its own set of advantages and disadvantages. [27] provides a broad overview of the SSO phenomenon, methods available for its analysis, the associated instability risks across different types of WFs, and potential mitigation strategies that have not yet been extensively investigated. Certain limitations tend to be overlooked in the existing literature, which primarily explores the series-capacitor induced SSO in WPPs [16], [28]. Traditional methods have limited effectiveness,

and SDC design is complex. Existing research overlooks broader instability risks, focusing mainly on series-capacitor SSR. Practical deployment challenges require extensive testing under varying grid conditions for reliability.

2.3.1. FACTS-Based Mitigation Techniques

Flexible AC Transmission System (FACTS) devices, such as Thyristor-Controlled Series Capacitors (TCSC), Static Var Compensators (SVC), and Static Synchronous Series Compensators (SSSC), are widely employed to mitigate SSR by dynamically adjusting line impedance and damping subsynchronous oscillations. For example, TCSC has been shown to effectively suppress SSR in SC grids by introducing variable capacitive reactance, thereby destabilizing resonant modes [29]. Similarly, SVCs enhance damping by modulating reactive power injection, as demonstrated in case studies of Vietnamese thermal plants where SVC-based control strategies resolved SSR-induced shaft failures [29]. SSSC, with its subsynchronous component-based (SSC) control schemes, injects counteractive voltages to neutralize subsynchronous currents, significantly reducing torsional oscillations [30]. While FACTS devices are effective, their high cost and complexity limit widespread adoption in wind-dominated grids.

2.3.2. Power System Stabilizers (PSS)

Power System Stabilizers (PSS) are traditionally used in synchronous generators to damp low-frequency oscillations by modulating excitation systems. However, their efficacy in mitigating SSR in DFIG-WFs is limited due to the lack of direct coupling between PSS and converter controls [31]. Studies indicate that PSS with ΔP (active power deviation) input signals can marginally improve subsynchronous damping in mixed-generation systems by enhancing synchronizing torque. Despite this, PSS remains insufficient for addressing SSR in high wind-penetration scenarios, necessitating complementary strategies like SDCs [32], [33], [34].

2.3.3. Supplementary Damping Controllers

SDCs are specifically designed for converter-interfaced WTs, offering targeted SSR mitigation by modulating RSC controls. These controllers detect subsynchronous frequencies and inject damping signals to destabilize resonant modes. Recent advancements include the integration of SDCs with VI capabilities

(VISDC), enabling dual functionality in damping oscillations and enhancing grid frequency stability [35]. For instance, SSC-based SDCs paired with SSSC have demonstrated near-complete SSR suppression in IEEE benchmark models by nullifying subsynchronous currents [30]. SDCs are increasingly favoured over FACTS and PSS in wind applications due to their lower cost, scalability, and compatibility with existing turbine controls.

2.3.4. Importance of Virtual Inertia in Power Systems

In traditional power systems, synchronous generators inherently provide rotational inertia through their spinning masses, which helps to stabilize system frequency during disturbances. This inertia acts as a buffer, slowing down the rate of frequency change and allowing time for control mechanisms to respond. However, the increasing integration of renewable energy sources, particularly those connected via power electronic converters like wind and solar, has led to a significant reduction in system inertia. Converter-Interfaced Generators (CIGs) lack the physical rotating mass of synchronous machines, resulting in diminished inertial response capabilities [36]. This decline in inertia poses challenges for power system stability, including higher Rates of Change of Frequency (RoCoF) and increased risk of frequency deviations beyond acceptable limits. To mitigate these issues, the concept of virtual inertia has been introduced. Virtual inertia emulates the inertial response of synchronous machines by using control algorithms within power electronic converters to inject or absorb power in response to frequency changes [37]. In the context of DFIG-WECS, virtual inertia can be implemented through modifications in the control strategies of the RSC. By doing so, DFIG-based systems can contribute to frequency stability, enhancing the overall resilience of the power grid [38].

As power systems continue to evolve with higher penetrations of renewable energy, incorporating virtual inertia into converter-based generation becomes essential. It ensures that the benefits of renewable integration do not come at the expense of system stability and reliability. More on VI is discussed in section 3.4 of the next chapter.

2.3.5. Key Insights from Literature

1. FACTS devices (TCSC, SVC, SSSC) provide robust SSR damping but face economic and operational barriers in WFs [29], [30].
2. PSS offers limited SSR mitigation in DFIG systems and is more suited to conventional grids [31].
3. SDCs, particularly those integrated with VI, represent a cost-effective and scalable solution for modern WFs [30], [35].

This analysis underscores the shift toward SDC-based strategies in WE systems, aligning with the focus of this work on PI-based SDCs and VISDC.

The reviewed literature highlights the evolving challenges and research trends associated with the integration of DFIG-WPSs, particularly under resonance and fault conditions. To establish a comprehensive understanding, the subsequent chapter delves into the fundamental aspects of Wind Energy Conversion Systems (WECS), including various WT configurations (Types A–D) and the detailed architecture of the DFIG-based system used in this work.

CHAPTER 3. WIND ENERGY CONVERSION SYSTEMS

3.1. Introduction

WE stands at the forefront of the global transition toward sustainable and low-carbon power generation. By utilizing the kinetic energy (KE) of moving air, WTs efficiently convert wind's mechanical energy into electrical power, providing a clean and renewable alternative to conventional fossil-fuel-based electricity. The deployment of WFs, both onshore and offshore, has expanded rapidly over the past decade, driven by technological advancements, supportive policy frameworks, and the urgent need to address climate change. As of 2024, global installed wind power capacity has exceeded 1,100 GW, making wind one of the fastest-growing sources of electricity worldwide [39].

The environmental benefits of WE are substantial: it produces no direct greenhouse gas emissions, requires no water for operation, and has a minimal ecological footprint compared to traditional power plants. Economically, the wind sector has catalysed job creation, regional development, and cost reductions in electricity supply, particularly as the levelized cost of WPP continues to decline. Nevertheless, challenges remain, including the inherent variability of wind resources, integration with existing power grids, and concerns regarding land use and wildlife impacts. Overcoming these challenges is essential for maximizing the contribution of WE to a resilient, decarbonised energy system [40].

The following sections detail the fundamental components and working principles of WECS, including the aerodynamic and mechanical subsystems, control strategies, and modelling approaches such as DFIG-WT modelling, generator and power electronic interfaces, as well as the integration of these models for comprehensive system analysis and control design.

3.2. WECS

A Wind Energy Conversion System (WECS) is an integrated assembly designed to capture the KE of wind and convert it into electrical energy suitable for grid supply or local use. At its core, a WECS consists of a WT that extracts energy from the wind, a mechanical drive train, an electrical generator, PECs, and a suite of control systems

that ensure optimal and safe operation. Over the years, WECS technology has evolved from simple fixed-speed IG systems to sophisticated variable-speed, variable-pitch configurations employing advanced generators such as DFIG and Permanent Magnet Synchronous Generators (PMSG). Modern WECS are engineered to maximize energy capture, improve grid compatibility, and enhance operational flexibility under varying wind and grid conditions.

The fundamental operation of a WECS involves converting the wind's KE into mechanical rotation via the turbine blades, which is then transformed into electrical power by the generator. This power is conditioned and controlled before being delivered to the grid. The following subsections explore the main components of a WT, providing a foundation for detailed modelling and analysis in subsequent sections.

Figure 3-1 showcases the most important components of a Horizontal Axis WT (HAWT)

3.2.1. WT Components

1. ***Turbine Blades:*** Aerodynamically shaped and typically constructed from fibreglass, carbon fibre, or composite materials, turbine blades are mounted on the rotor hub. Their length, profile, and material composition directly influence the amount of KE extracted from the wind and converted into rotational mechanical energy.
2. ***Pitch Mechanism:*** The pitch system dynamically adjusts the angle (pitch) of the blades to optimize energy capture across varying wind speeds. By feathering the blades during high winds or storms, the pitch mechanism also serves as a primary means of protecting the turbine from mechanical overload and excessive loads.
3. ***Rotor Mechanical Brake:*** An essential safety feature, the rotor brake enables rapid stopping of the rotor during emergencies, grid faults, or scheduled maintenance. This system works in conjunction with aerodynamic braking (via blade pitching) to ensure safe and controlled shutdown of the turbine.
4. ***Generator:*** The generator transforms the mechanical energy from the rotor into electrical energy. Modern WTs may employ asynchronous (induction), synchronous, or permanent magnet generators. The choice of generator type affects grid integration, efficiency, and control strategies—DFIGs, for

example, are widely used for their variable speed and grid support capabilities.

5. ***Yaw Controller:*** The yaw system rotates the nacelle (the housing that contains the generator and gearbox) to align the rotor with the prevailing wind direction. Accurate yaw control maximizes energy capture and reduces asymmetric loading on the blades and tower.
6. ***Gearbox:*** In many turbines, a gearbox (GB) steps up the low-speed rotation of the rotor to a higher speed suitable for the generator. However, direct-drive turbines eliminate the GB, reducing mechanical complexity and maintenance requirements.
7. ***Tower and Foundation:*** The tower elevates the rotor to heights where wind speeds are typically higher and more consistent, enhancing energy yield. The foundation anchors the entire structure, providing stability against dynamic wind loads and ensuring long-term structural integrity.
8. ***Wind Sensors:*** Anemometers and wind vanes, mounted atop the nacelle, continuously measure wind speed and direction. This real-time data feeds into the turbine's control systems, enabling adaptive adjustments to blade pitch and yaw orientation for optimal performance and protection.
9. ***Control and Protection Systems:*** Embedded controllers monitor and regulate all turbine operations, including pitch, yaw, generator output, and safety interlocks. Advanced control algorithms improve efficiency, enable fault detection, and ensure compliance with grid codes.
10. ***Power Electronics and Converter Systems:*** Especially in variable-speed turbines (e.g., DFIG or full-converter types), PECs manage the interface between the generator and the grid. They enable variable-speed operation, grid support functions, and compliance with power quality and stability requirements.

Together, these components form an integrated system capable of reliably converting WE into electricity while maintaining operational safety, efficiency, and grid compatibility.

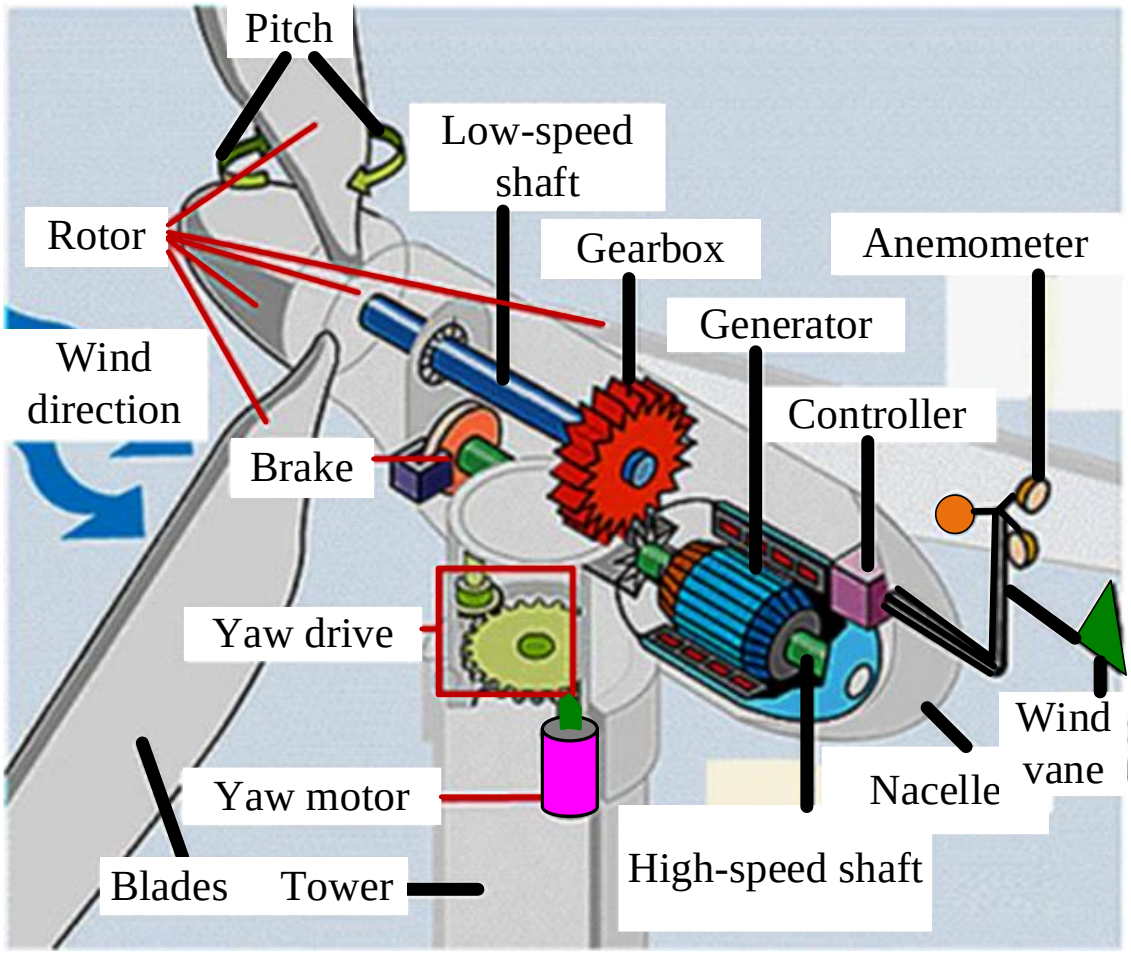

Figure 3-1. Schematic Diagram of Major WTG Components of a Modern HAWT

3.2.2. WTG Types: Dependence on Control Methods and Generator Technology

WTGs can be classified based on several technical criteria, reflecting differences in operational strategy, mechanical design, electrical configuration, and control methods. Fundamentally, the operational characteristics and performance of WTGs are determined by the combination of generator technology and the associated control strategies. Broadly, WTGs are categorized into constant speed and variable speed systems, each employing distinct generator types and control configurations to optimize energy capture and grid integration.

These classification criteria include:

1. **Speed regulation** (constant or variable speed),
2. **Pitch control strategy** (fixed or variable pitch),
3. **Drive train configuration** (gearless or geared),
4. **Generator type**, and
5. **Grid connection topology** (direct coupling or via PECs interface).

Based on these factors, four main types of WTGs are widely used in the industry:

3.2.3. Type A: Fixed-Speed WTGs with Squirrel Cage Induction Generators (SCIGs)

Type A WTGs operate at nearly constant speed, closely synchronized with the grid frequency. They use squirrel cage induction generators (SCIGs) directly connected to the grid through a step-up transformer without any PECs. This simple and robust configuration leads to low initial costs, high mechanical reliability, and ease of maintenance. However, constant-speed operation restricts the turbine's ability to adapt to wind speed variations, resulting in reduced energy capture efficiency, increased mechanical stress due to wind turbulence, and poor power quality control. Additionally, **Type A** turbines lack the dynamic response and grid support capabilities required by modern grid codes. Figure 3-2 shows a typical Type A WTG.

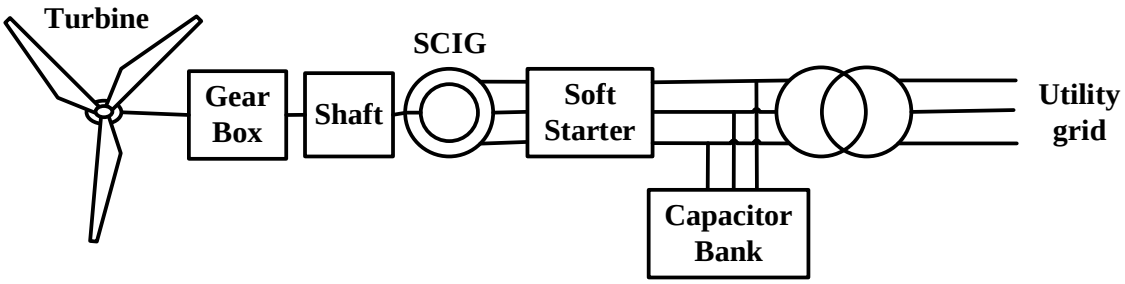

Figure 3-2. Type A Fixed-Speed WT equipped with SCIG

3.2.4. Type B: Limited Variable-Speed WTGs with Wound Rotor Induction Generators (WRIGs)

Type B turbines employ wound rotor induction generators (WRIGs) with external rotor resistance or a rotor-side PEC to allow limited variation of rotor speed. This capability slightly enhances energy capture and reduces mechanical stress compared to **Type A** turbines. Although still primarily connected to the grid without a full converter interface, Type B systems offer limited dynamic control over torque and power output. However, the external resistance introduces additional losses, and the variable speed range remains narrow, which restricts their ability to exploit wind speed variability fully. Figure 3-3 shows the schematic for Type B WT.

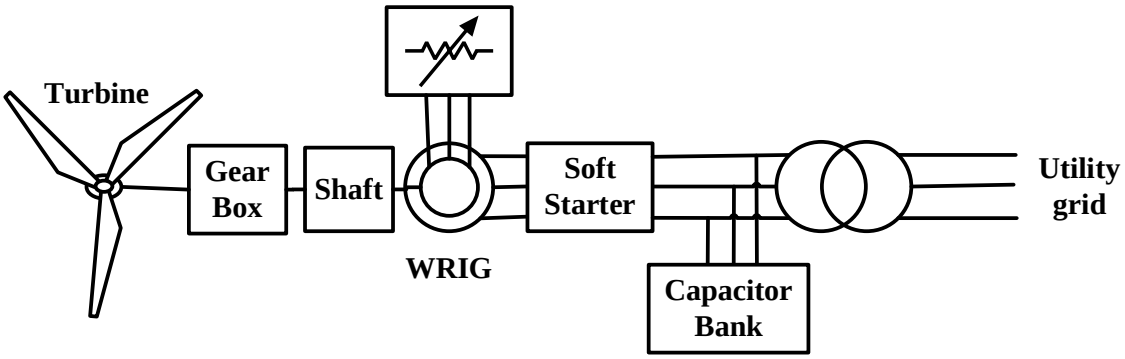

Figure 3-3. Type B WT Featuring Limited Variable-Speed and WRIG

3.2.5. Type C: Variable-Speed WTGs with DFIGs

Type C WTGs are among the most widely deployed in utility-scale WFs. They utilize a DFIG with a partial-scale back-to-back PEC (typically handling 25–30% of the total power) connected to the rotor circuit. This configuration allows for variable-speed operation over a broad range (±30% of synchronous speed), leading to improved aerodynamic efficiency, reduced mechanical loading, and better control over active and reactive power. The partial-scale converter also enables grid support functions such as low-voltage ride-through (LVRT), voltage regulation, and frequency control, making Type C turbines compliant with modern grid codes while remaining cost-effective due to the reduced converter size. Figure 3-4 shows a typical Type C WT.

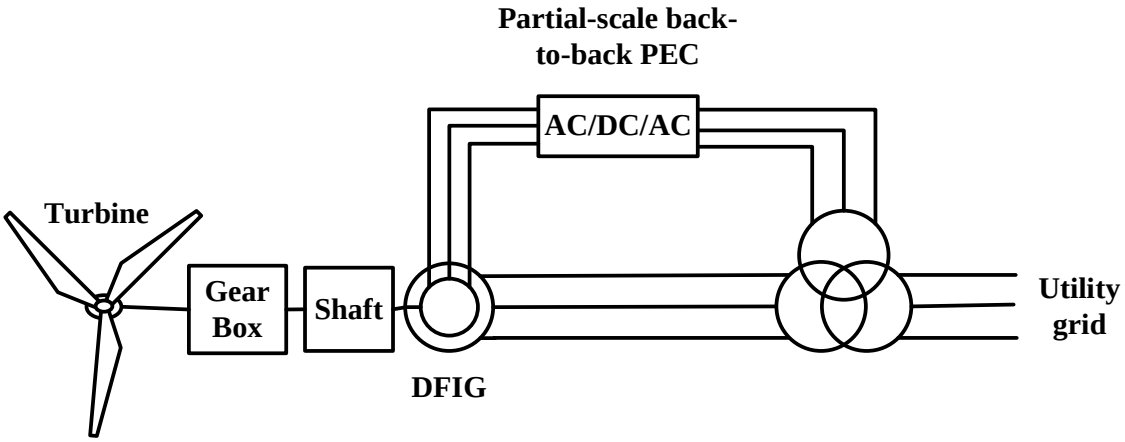

Figure 3-4. Type C WT Featuring Variable-Speed and DFIG with Partial-Scale PEC

3.2.6. Type D: Variable-Speed WTGs with Permanent Magnet Synchronous Generators (PMSGs) or Wound Rotor Synchronous Generators (WRSGs)

Type D turbines use full-scale PECs (typically 2-level or 3-level voltage source converters) interfacing gearless or geared synchronous generators with the grid. The generator can be either a PMSG (preferred for offshore and direct-

drive systems due to high power density and absence of excitation losses) or a WRSG. The full-scale converter decouples the generator from the grid, providing maximum control flexibility over both active and reactive power, enabling operation over a wide speed range, and ensuring compliance with stringent grid codes and fault ride-through requirements. **Type D** WTGs exhibit excellent power quality, improved reliability, and are well-suited for offshore WFs and weak grid conditions, although at the cost of higher capital and maintenance complexity. Figure 3-5 depicts Type D WT.

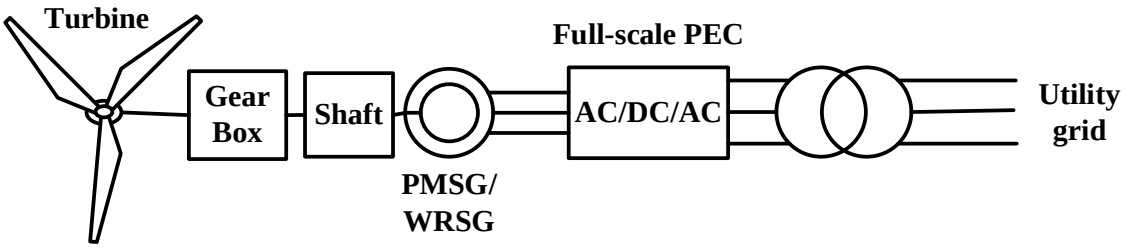

Figure 3-5. Type D Variable-Speed with Full Scale PEC with PMSG/WRSG

Table 3-1. Classification of WTG Types

Type	Generator Type	Speed Control	Power Electronics	Grid Connection	Typical Application
Type A	SCIG	Constant Speed	None	Direct to Grid	Early-generation/ Small onshore
Type B	WRIG	Limited Variable Speed	Rotor Resistance (or converter)	Direct to Grid	Transitional/ Legacy systems
Type C[1]	DFIG	Variable Speed	Partial-Scale Converter	Stator: Direct, Rotor: Converter	Predominantly modern onshore
Type D	PMSG/ WRSG	Full Variable Speed	Full-Scale Converter	Fully Decoupled via Converter	Offshore/ Large-scale modern

[1] Although Type C WTGs are predominantly used in onshore WFs, they have also been increasingly adopted in various offshore installations due to their cost-effectiveness and mature control technology.

3.3. DFIG: Architecture and Operating Principles

DFIGs have emerged as the dominant generator topology for WPPs due to their ability to offer variable-speed operation with reduced converter ratings, typically around 30% of the generator power. This is made possible by their unique architecture, where the

stator is directly connected to the grid, while the rotor is interfaced via a partially rated back-to-back converter. This configuration enables independent control of active and reactive power, meeting stringent grid code requirements while optimizing energy extraction over a broad wind speed range.

3.3.1. Basic Structure and Grid Interface

In a DFIG-WT, the low-speed shaft from the WT rotor is connected to the DFIG rotor through a multi-stage GB, since the natural rotational speed of the turbine is not sufficient for direct power generation at grid frequency. The stator of the DFIG is directly connected to the grid, allowing approximately 70–75% of the total power to flow directly without conversion losses. The rotor, on the other hand, is connected to the grid through slip rings and a back-to-back Voltage Source Converter (VSC) configuration, which handles the remaining 25–30% of the power.

This partial-scale power electronics architecture significantly reduces converter size and cost compared to full-converter systems. Moreover, it enables bidirectional power flow and dynamic control of rotor currents, which is essential for regulating both active and reactive power.

3.3.2. Operating Principles of DFIG

The key operational advantage of DFIG lies in its ability to operate at variable speeds, governed by the *slip* defined as:

$$s = \frac{\omega_s - \omega_r}{\omega_s} \tag{4}$$

Where:

- ω_s = synchronous speed
- ω_r = rotor speed

Depending on the sign of the slip, the DFIG system operates in both sub-synchronous and super-synchronous modes, depending on wind speed:

1. **Sub-synchronous mode (s > 0):** Rotor speed is below synchronous speed; power flows from the grid into the rotor through the converter. The RSC injects current into the rotor to maintain torque production, while the GSC returns this power to the grid. Refer to Figure 3-6 for a pictorial representation.

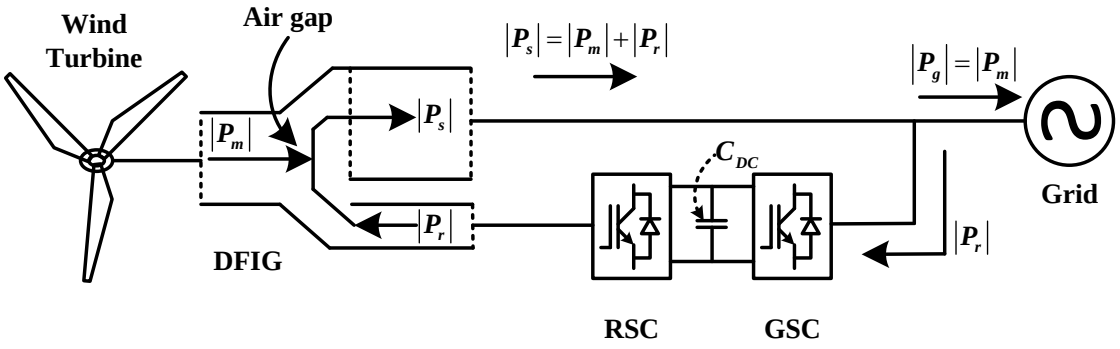

Figure 3-6. Power flow in DFIG during Sub-Synchronous Mode of Operation

2. **Super-synchronous mode (s < 0):** Rotor speed is above synchronous speed; power flows from the rotor to the grid. In this case, both stator and rotor contribute to the grid power. Refer to Figure 3-7 for a pictorial representation.

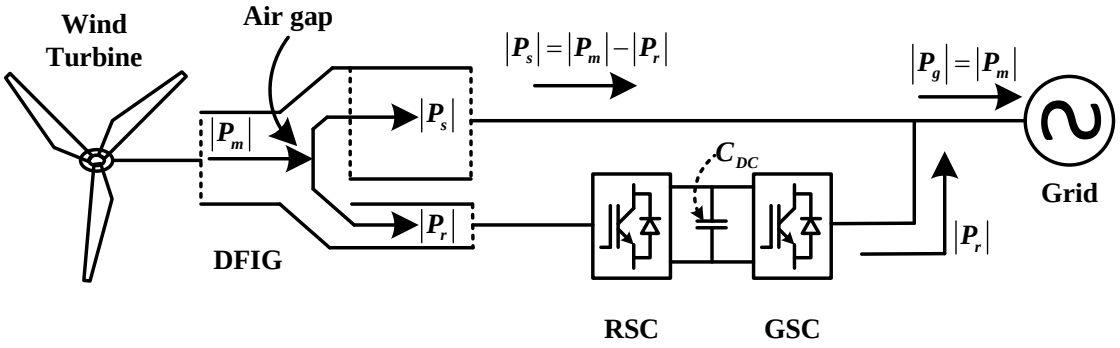

Figure 3-7. Power flow in DFIG during Super-Synchronous Mode of Operation

Thus, the DFIG supports bidirectional rotor power flow based on wind speed, and the net output power remains governed by the sum of stator and rotor contributions. This flexible operation improves energy capture over a wider wind speed range and reduces mechanical stresses.

3.3.3. Back-to-Back Converter: RSC and GSC Roles

The RSC regulates the rotor current to control electromagnetic torque and reactive power. It enables vector control in a synchronously rotating frame, effectively decoupling torque and flux control.

The Grid Side Converter (GSC) maintains a constant DC-link voltage and exchanges reactive power with the grid. It plays a crucial role in fulfilling grid code

requirements, including low-voltage ride-through (LVRT), frequency support, and power quality enhancement.

Some literature refers to RSC as Machine Side Converter (MSC) [41], [42] and GSC as Load Side Converter (LSC) [12], [41].

3.3.4. Slip Power Recovery and Energy Conversion Efficiency

One of the most economically attractive features of the DFIG architecture is that only a fraction of the total wind-generated power, specifically, the slip power, is processed by the PECs. This design leads to reduced converter size, lower cost, and improved system efficiency compared to fully rated converter systems.

Consider that the total mechanical power extracted by the turbine from the wind (P_{mech}) is divided between the stator and the rotor paths:

$$P_m = P_s + P_r \tag{5}$$

In the DFIG system:

- The *stator*, which is directly connected to the grid, delivers the majority of the power.
- The *rotor*, which is connected through the back-to-back converter, handles only the slip-dependent portion.

Mathematically, this power division is approximately given by:

$$\left.\begin{aligned} P_s &\approx \left(1-|s|\right).P_m \\ P_r &\approx |s|.P_m \end{aligned}\right\} \tag{6}$$

Where *s* is the slip, a dimensionless quantity representing the deviation of rotor speed from synchronous speed.

- For small slips (e.g. ±0.3), only 30% or less of the total power flows through the converter.
- This significantly reduces the size and cost of the power electronic components compared to systems where the full generator output must be processed (e.g., in Type D full-converter systems).

Hence, it can be seen from this that at any given time, the rotor converters only need to handle the slip power, not the full machine rating. This is the characteristic that makes DFIGs especially suitable for medium to large-scale WFs, where cost-effectiveness and energy efficiency are both critical.

3.3.5. Betz Limit and Theoretical Power Extraction

The amount of power that can be extracted from wind is fundamentally limited by fluid dynamics. This theoretical upper bound, known as the Betz limit, states that no WT can capture more than 59.3% of the KE of the wind. First derived by Albert Betz in 1919, this limit assumes an ideal actuator disk in incompressible flow with no mechanical or electrical losses.

The maximum extractable power P_{max} from the wind is given by:

$$P_{\max} = \frac{16}{27} \cdot \underbrace{\frac{1}{2} \rho A v^3}_{P_{wind}} \tag{7}$$

Where:

- ρ is the air density in kg/m^3
- A is the swept area of the turbine blades in m^2
- V is the wind velocity in m/s

The fraction $\frac{16}{27}$ corresponds to the maximum power coefficient $C_p^{\max} = 0.593$. In real-world applications, the actual power coefficient is lower due to mechanical, electrical and control-related inefficiencies.

The Betz limit defines the first-stage efficiency of a WECS. It determines the maximum mechanical power that the rotor can extract from the wind, forming the basis for further electrical conversion by the generator system, such as DFIG.

3.3.5. DFIG's Unique Characteristics Conducive to SSR

DFIGs possess certain characteristics that can make them more conducive to SSR when used in SC systems:

1. **Variable Speed Operation:** DFIGs can operate at variable speeds, which can introduce a wide range of frequencies into the system. This increases the likelihood of matching the natural frequency of the SC and the system's torsional modes, leading to resonance.
2. **Grid-side Converter (GSC):** The GSC in a DFIG can introduce additional harmonics and fluctuations into the system. These disturbances can interact with the SC and contribute to SSR.
3. **Control Strategies:** The control strategies used in DFIGs can influence their interaction with the SC. Improperly designed or tuned control systems can exacerbate SSR conditions.

4. **Interaction with PS:** DFIGs are interconnected with the broader PS, which can introduce complex dynamics and resonances. The interaction between the DFIG and the SC within this larger system can lead to SSR.
5. **Torsional Modes:** DFIGs have multiple torsional modes due to the mechanical structure of their rotor. If the torsional frequency of any of these modes matches the resonant frequency created by the SC, SSR can occur.

These unique characteristics of DFIGs, in combination with the presence of SCs, create a complex environment where SSR can be more likely to occur compared to traditional synchronous generators. Therefore, careful design, control, and monitoring are essential to mitigate SSR risks in DFIG-WPSs.

3.3.6. DFIG's Vulnerability to SSR

The DFIG's partial connection to the grid, especially through series-compensated lines, makes it prone to SSR, a condition where the interaction between the generator's control system and the TL can cause destructive oscillations at frequencies below the synchronous frequency of the grid, leading to mechanical stresses on generator TL components, and other equipment, potentially leading to damage or instability.

3.3.7. SSR Mitigation Techniques and Optimal Controller Placement Locations

In [43], to mitigate SSR, an SSR damping controller was proposed for the GSC. The controller employs bus voltages and line currents as feedback signals to inject damping currents at sub-synchronous frequencies, thereby mitigating SSR within the system. A pseudo-adaptive control approach is proposed in [44] as a mitigation strategy for the GSC. In [45], the characteristics of SSR are examined using an adaptive algorithm. Based on this analysis, a pseudo-adaptive controller and a resonant controller are implemented in the GSC to compensate for phase-locked loop (PLL) estimation errors and suppress SSR. The power rating of GSC is slightly higher than that of RSC, as it is closer to the grid, and has to incorporate the higher power of the grid as compared to that of RSC. DFIG-WPP uses RSC for variable-speed control and GSC for grid stability. GSC-based SSR mitigation employs damping controllers, but challenges include complex tuning, higher power handling, and the need for improved adaptive strategies.

In a DFIG-WPP, the RSC is a more optimal location for implementing control compared to the GSC. The RSC directly regulates the rotor currents, enabling independent control of torque and flux, which allows precise regulation of the generator's active and reactive power and, consequently, the stator power fed to the grid. This direct control results in faster power tracking, enhanced damping of SSR oscillations and improved robustness against line faults, making it particularly effective in mitigating transient instabilities. In contrast, the GSC primarily manages DC-link voltage stability and provides limited reactive power support at the grid level, lacking direct influence over stator-side dynamics. Since SSR originates in the rotor circuit, RSC-based control is inherently more effective in suppressing oscillations at the source, whereas GSC control has a weaker impact on the generator's electromechanical response. Additionally, RSC control enables faster response to grid disturbances by dynamically adjusting rotor-side currents, stabilizing stator voltage more efficiently than GSC intervention. These advantages demonstrate that placing the controller in the RSC yields far superior transient performance, quicker SSR mitigation, arresting severe voltage sags and current surges in case of faults, thereby improving the overall grid integration of the DFIG system. An SSR damping controller based on a Proportional-Integral (PI) controller is proposed to mitigate SSR in [46]. The optimal placement of this controller is determined using an algorithm that analyses the critical parameters influencing the behaviour of DFIG-based WFs on SSR. The results suggest that the DC-link voltage is the most suitable input point for the GSC, whereas the q-axis component of the rotor voltage is the most effective input point for the RSC. To mitigate SSR, [47] utilizes a two-degree-of-freedom control strategy, incorporating a PI controller implemented in the RSC. Furthermore, a damping controller utilizing a Proportional Derivative (PD) control strategy is proposed for the RSC to attenuate SSR in [48]. This controller has been successfully developed and validated through hardware implementation. RSC-based control in DFIG-WPP offers superior SSR mitigation, faster transient response, and robust fault handling by directly regulating rotor currents. GSC control, limited to DC-link stability, has weaker SSR suppression. PI and PD controllers enhance RSC performance, ensuring effective damping, improved stator voltage stability, and better grid integration.

3.4. Inertia Deficiency in IBRs and Role of VI in Grid Stability

All RES, primarily solar and wind, are not only intermittent in nature but also Inverter-Based Resources (IBR), meaning they are entirely reliant on power electronics and lack the inherent inertia found in conventional sources of electricity generation. Conventional sources, on the other hand, inherently possess a physical rotating mass coupled with governors that regulate the system's inertia. This inertia plays a key role in stabilizing the system's frequency, a function that is typically absent in RES, which relies on inverter-based technologies that lack mechanical inertia. Therefore, standard renewable energy-producing equipment is unable to regulate power supply frequency variations caused by grid oscillations [49]. The inertia of the PS is falling, posing a threat to frequency stability [50]. Modern grid integration methods, such as synthetic or VI, can help mitigate this issue [51]. VI control involves using the KE stored in the WT's rotor to enhance the electromagnetic power output of the inverter [26], thereby slowing down the frequency drop over a short period [52]. An in-depth investigative analysis in [53] demonstrates the impact of VI on enhancing system stability and emphasises the importance of assigning VI, particularly to remote WFS. RES, like solar and wind, lack natural inertia, impacting frequency stability. VI control extracts KE from WTS, mitigating frequency drops and enhancing grid stability, especially for remote WFS.

This work provides research gaps and contributions as follows:

1. RES, particularly wind and solar, lack inherent inertia due to their reliance on IBRs, leading to frequency instability. Existing solutions for synthetic inertia remain underexplored in large-scale wind power integration. This study enhances VI control, optimising the use of WT rotor KE to stabilise frequency and improve overall grid resilience. The placement of the VI controller is done in the RSC of the model.
2. Conventional SSR mitigation techniques primarily rely on GSC-based control, which lacks direct influence over rotor-originated oscillations, leading to limited effectiveness. The work motivation is on developing an optimised RSC-based damping controller for more effective SSR suppression and enhanced transient performance.
3. Despite the known benefits of VI, its implementation in remote WFs remains underexplored, affecting stability in weak grids. This study investigates and

optimises VI deployment for remote WFS, ensuring better grid integration and system stability.

4. Most works do not provide a detailed comparison of RSC- and GSC-based control strategies for SSR mitigation. This study systematically investigates both approaches and demonstrates RSC's superior performance in SSR mitigation and transient stability.
5. Many SSR mitigation studies rely on theoretical models without real-time validation. This study employs OPAL-RT simulations and hardware-based experiments to validate the proposed strategies, ensuring practical implementation feasibility.

Building on the operational principles and structural characteristics of wind energy conversion systems, the next chapter focuses on the mathematical modelling of the DFIG-based wind power plant and its representation in state-space form for analytical and control design purposes.

CHAPTER 4. SYSTEM MODELLING AND STATE-SPACE ANALYSIS

4.1. Design of Wind PS Model under study

Figure 4-1 depicts the power flow diagram of the DFIG-WF. The WE is converted into mechanical power via turbine blades and a multistage GB, which drives the rotor shaft. The turbine and rotor shafts rotate in the direction of the wind, while the generated electromagnetic torque opposes the aerodynamic torque, exciting the DFIG to produce electrical power. The system operates in both sub-synchronous and super-synchronous modes, maintaining a constant total power supply to the grid, regardless of operational mode. SC enhances power transmission efficiency but introduces the risk of SSR, leading to oscillations that can destabilise the system. Additionally, three-phase symmetrical faults can cause sudden voltage dips, resulting in severe transient instability. These disturbances necessitate an effective control strategy to ensure stable and reliable grid integration.

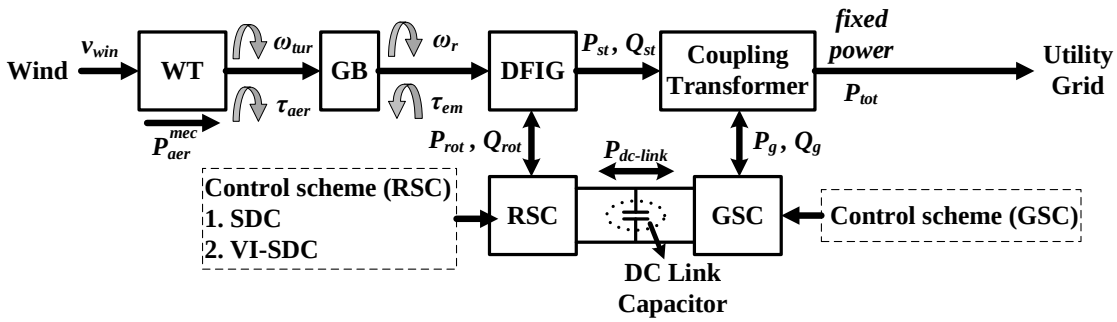

Figure 4-1. Block diagram of the DFIG system with integration of the grid

The DFIG interfaces with the grid through the stator (which carries most of the power) and the rotor (which connects via slip rings and back-to-back VSCs). The RSC regulates active and reactive power, allowing dynamic control over torque and flux, while the GSC stabilizes DC-link voltage. Given that SSR originates in the rotor circuit, RSC-based control is more effective in mitigating oscillations at the source. To enhance grid stability, advanced damping controllers are employed within the RSC to suppress SSR, mitigate voltage sags, and improve fault ride-through (FRT) capability. Proper tuning of these controllers ensures that DFIG-WTs can operate reliably under varying wind speeds, compensation levels, and grid fault conditions.

4.1.1. Expression for the Power of WT

The wind power of an air mass flowing at a speed v_{win} through an area A_{tur}^{swp}, captured by the turbine and converted to aerodynamic mechanical power available from the turbine rotor is given as [1],

$$P_{aer}^{mec} = C_p(\lambda,\beta) \times \underbrace{\frac{1}{2}\rho_{air} A_{tur}^{swp} (v_{win})^3}_{P_{win}} = \frac{1}{2} C_p(\lambda,\beta)\rho_{air}\pi(R_{tur})^2 (v_{win})^3 \quad (8)$$

where P_{aer}^{mec} is the wind power; C_p is the power coefficient, a key performance metric for WTs, quantifying the efficiency with which the wind's KE is converted into mechanical energy, depending on turbine design, determined by blade pitch angle (β) and tip speed ratio (TSR $\rightarrow \lambda$); ρ_{air} is the specific air density, a function of pressure and temperature (assumed as 1.1644 kg/m^3 at sea level and temperature of 30° C); A_{tur}^{swp} represents the area occupied by the rotating wind blades (i.e. turbine-swept area) in m^2; v_{win} denotes undisturbed wind speed approaching the turbine in m/s; R_{tur} is the radius of the WT in m.

4.1.2. Expression for Torque

The WT blades capture KE from the wind and convert it into mechanical rotational energy. The wind-induced aerodynamic torque (T_{aer}) can be computed using the following expression:

$$T_{aer} = \frac{P_{aer}^{mec}}{\omega_{tur}} = \frac{C_p(\lambda,\beta)\rho_{air} A_{tur}^{swp} (v_{win})^3}{2\omega_{tur}} \quad (9)$$

where ω_{tur} is the angular velocity of the turbine's rotor shaft (R_{tur}) in rad/sec.

The aerodynamic performance of a WT is characterized by the power coefficient (C_p), a nonlinear function of TSR (λ) and blade pitch angle (β), which is expressed by

$$C_p = C_1\left(\frac{C_2}{\lambda_i} - C_3\beta - C_4\right)\exp\left(-\frac{C_5}{\lambda_i}\right) + C_6\lambda \quad (10)$$

Where

$$\frac{1}{\lambda_i} = \frac{1}{\lambda + C_7\beta} - \frac{C_8}{\beta^3 + 1}$$

$$\lambda = \frac{\text{tip speed of the blade}}{\text{wind speed}} = \frac{v_{tip}}{v_{win}} = \frac{\omega_{tur} \times R_{tur}}{v_{win}} = \frac{\frac{2\pi N_{tur}}{60} \times R_{tur}}{v_{win}}$$

With C_1 = 0.5176, C_2 = 166, C_3 = 0.4, C_4 = 5, C_5 = 21, C_6 = 0.0068, C_7 = 0.08, C_8 = 0.035. The blade pitch angle is maintained constant at β = 0°, and N_{tur} is the rotation of the turbine blade in Revolutions Per Minute (RPM).

A WT of 1.5 MW is designed in this work, at a constant 9 m/s rated wind speed, incorporating a multi-stage step-up gear mechanism. The design optimizes for a maximum power coefficient $\left(C_p^{max}\right)$ of 0.3755, achieved at a TSR (λ = 6), recognised as the optimal value for maximising energy capture from the available wind. From the equation (9), the WT radius is calculated to be 54.735 m.

4.1.3. Expression for the GB ratio

Due to the relatively low rotational speed of WT, a multistage step-up GB is used to increase the rotational speed to a level suitable for power generation in the generator. Torque of the (GB) T_{gb} and the rotor's angular speed (ω_{rot}) are expressed as follows,

$$\left.\begin{aligned} T_{gb} &= \frac{T_{aer}}{\eta} \\ \omega_{rot} &= \eta \omega_{tur} \end{aligned}\right\} \tag{11}$$

where η is the multi-stage step-up GB ratio, 52π rad/sec (163 rad/sec) and 28π rad/sec (88 rad/sec) are considered as the maximum (ω_{rot}^{max}) and minimum (ω_{rot}^{max}) rotor speeds of DFIG, respectively, obtained as ±30% of 40π rad/sec (126 rad/sec), which is the synchronous ω_{rot}. The corresponding synchronous N_{tur} = 1200 rpm, with maximum (N_{tur}^{max}) and minimum (N_{tur}^{min}) values as 1560 rpm and 840 rpm, respectively. is obtained as 0.9866 rad/sec from the equation of λ by substituting λ = 6 and R_{tur} = 54.735 m. η is calculated as 165.5816 at a constant speed of 9 m/s and 163 rad/sec rotor speed.

4.1.4. Expression for the Mechanical Equation of the whole system

The mechanical equation of the system is expressed as follows

$$\underbrace{\left(\frac{J_{tur}}{\eta^2} + J_{DFIG}\right)}_{Total\ inertia\ of\ the\ system} \times \frac{d}{dt}\omega_{rot} = T_{aer} - T_{em} - F\omega_{rot} \tag{12}$$

where T_{em} and F are the electromagnetic torque of DFIG and the coefficient of friction, respectively. J_{tur} and J_{DFIG} are the aggregated inertias of the turbines and the generators.

For a lossless generator, the mechanical equation of the system is as follows

$$J_{total}\frac{d}{dt}\omega_{rot} = \tau_{aer} - \tau_{em} \tag{13}$$

Where J_{total} represents the total inertia of the system's rotor and turbine.

4.2. Expressions for Stator and Rotor Powers

The DFIG consists of both a stator and a rotor, where the stator is directly connected to the grid while the rotor is connected via PECs. The stator generates most of the power (70-75%) and feeds it directly into the grid. The rotor allows variable-speed operation by adjusting the slip and contributes to about 25-30% of the total power through the converter system.

The power generated by the WT is converted into electrical power by the DFIG and transmitted to the grid via the stator and rotor windings. The mechanical power from the turbine and the electrical power from the stator are calculated using the equation below.

$$\left.\begin{aligned} P_{aer}^{mec} &= T_{aer}\omega_{rot} \\ P_{st} &= T_{em}\omega_{st} \end{aligned}\right\} \tag{14}$$

Under ideal conditions and at a steady speed (ω_{rot} = constant) for a lossless generator, the generator's mechanical torque (T_{aer}) matches the electromagnetic torque (T_{em}) applied by the generator to the rotor. Furthermore, the aerodynamic mechanical power available from the turbine rotor is the combined value of power output from the rotor and the stator. Consequently, the rotor's electrical power output (P_{rot}) can be calculated as follows,

$$\left.\begin{aligned} P_{rot} &= P_{aer}^{mec} - P_{st} = \tau_{aer}\omega_{rot} - \tau_{em}\omega_{st} \\ &= -\tau_{aer}\left(\frac{\omega_{st} - \omega_{rot}}{\omega_{st}}\right)\omega_{st} = -s\tau_{aer}\omega_{st} \\ &= -sP_{st} \quad \left(\because \tau_{em} = \tau_{aer}\right) \end{aligned}\right\} \tag{15}$$

P_{rot} is also known as the slip power in the context of DFIG, as it is directly related to the slip (s) of the machine, which is the difference between the synchronous speed of the stator magnetic field and the actual rotational speed of the rotor. This is a key term that shows the ability of the DFIG to operate in variable speed conditions, crucial for WT applications where wind speed fluctuates, leading to changes in the slip. In the context of DFIG, the slip can vary between – 0.3 and + 0.3, corresponding to ± 30% above (super-synchronous) and below (sub-synchronous) the synchronous speed, which is

predominantly restrained by the converter limitations and stable power exchange requirements between the rotor and the grid. This makes P_{rot} only a part of P_s. P_{rot} is a function of s in both magnitude and direction, as T_{gen} (owing to its mode of operation, generation) and ω_s (owing to the grid voltage's constant frequency) are positive. For speeds greater than synchronous speed (i.e. super-synchronous, s < 0), $P_{rot} > 0$, and $P_{rot} < 0$ for speeds lower than synchronous speed (i.e. sub-synchronous, s < 0). In the super-synchronous range, P_{rot} flows from DFIG's rotor to the grid, captured using the rotor slip ring and brushes, and is routed to the DC-bus capacitor, increasing the DC voltage. In the sub-synchronous range, P_{rot} is taken out of the DC-bus capacitor, leading to a fall in the DC voltage. During the synchronous speed operation, $P_{rot} = 0$, indicating whole of the generated power is being transmitted via the DFIG's stator directly to the grid.

4.2.1. Torque Conversion Dynamics in a Two-Mass shaft DFIG system

The torque conversion dynamics within the drivetrain can be appropriately modelled using a two-mass shaft system, with its behaviour described by the following set of equations:

$$\left.\begin{aligned} \frac{d}{dt}\omega_{tur} &= \frac{1}{2H_{tur}}\left(\tau_{aer} - K_{stif}\gamma - D_{tur}\omega_{tur}\right) \\ \frac{d}{dt}\omega_{rot} &= \frac{1}{2H_{gen}}\left(K_{stif}\gamma - \tau_{em} - D_{gen}\omega_{rot}\right) \\ \frac{d}{dt}\gamma &= 2\pi f\left(\omega_{tur} - \frac{1}{\eta}\omega_{rot}\right) \end{aligned}\right\} \tag{16}$$

Here, H denotes the inertia constant, K_{stif} represents the torsional stiffness coefficient, γ is the torsion angle, D_{tur} is the torsional damping coefficient, and f denotes the grid frequency. The subscripts *tur* and *gen* correspond to the turbine and generator sides, respectively.

The dynamic behaviour of the converter can be derived by applying KVL across relevant loops and KCL at appropriate nodes within the SC DFIG model, leading to the following expression at the Grid-Side Converter (GSC) output loop:

$$\frac{d}{dt}\begin{bmatrix} i_{ga} \\ i_{gb} \\ i_{gc} \end{bmatrix} = \begin{bmatrix} \left(-i_{ga}\right) & \left(-v_{ga}\right) & \left(2S_a - S_b - S_c\right) \\ \left(-i_{gb}\right) & \left(-v_{gb}\right) & \left(-S_a + 2S_b - S_c\right) \\ \left(-i_{gc}\right) & \left(-v_{gc}\right) & \left(-S_a - S_b + 2S_c\right) \end{bmatrix} \begin{bmatrix} R_{gf}/L_{gf} \\ 1/L_{gf} \\ v_{dc}/3L_{gf} \end{bmatrix} \tag{17}$$

Here, the subscripts *a*, *b* and *c* indicate the respective phases of the 3-φ network; i_g and v_g represent the current and voltage in the GSC loop, respectively. R_{gf} and L_{gf} are the resistance and inductance of the filter of the GSC, respectively, and S_a, S_b and S_c are the input switching signals for the GSC.

4.2.2. Modelling of DC-Link Capacitor

A DC-link capacitor acts as an energy buffer between the RSC and GSC, stabilizing voltage fluctuations and ensuring bidirectional power flow in the rotor circuit. At the junction connecting the DC-link capacitor, the relationship can be expressed as follows:

$$\frac{d}{dt}v_{dc} = \begin{bmatrix} i_{dc} \\ -(i_{ga}S_a - i_{gb}S_b - i_{gc}S_c) \end{bmatrix} \begin{bmatrix} 1/C_{dc} \end{bmatrix} \tag{18}$$

Here, i_{dc} represents the DC current flowing into the DC-link circuit, v_{dc} denotes the DC-link voltage, and C_{dc} represents the DC-link capacitance.

4.2.3. Expressions for RSC, stator-side, and GSC loops

The RSC controls the rotor currents to regulate active and reactive power exchange between the rotor and the grid. It plays a crucial role in SSR mitigation and power factor control. The GSC manages the DC-link voltage stability and provides limited reactive power support, ensuring smooth power delivery to the grid. On the input side of the RSC, the relationship can be expressed as follows:

$$\frac{d}{dt}\begin{bmatrix} i_{ra} \\ i_{rb} \\ i_{rc} \end{bmatrix} = \begin{bmatrix} -i_{ra} & -v_{ra} \\ -i_{rb} & -v_{rb} \\ -i_{rc} & -v_{rc} \end{bmatrix} \begin{bmatrix} R_r/L_r \\ 1/L_r \end{bmatrix} \tag{19}$$

Here, i_r, v_r, R_r and L_r represent the rotor current, voltage, resistance and inductance, respectively.

In the stator-side loop, the corresponding equations can be derived as follows:

$$\frac{d}{dt}\begin{bmatrix} i_{sa} \\ i_{sb} \\ i_{sc} \end{bmatrix} = \begin{bmatrix} i_{sa} & v_{sa} \\ i_{sb} & v_{sb} \\ i_{sc} & v_{sc} \end{bmatrix} \begin{bmatrix} R_s/L_s \\ 1/L_s \end{bmatrix} \tag{20}$$

Here, i_s, v_s, R_s and L_s represent the stator current, voltage, resistance and inductance, respectively.

At the node where the capacitor is connected to provide SC for the TL, the following equations can be derived:

$$\frac{d}{dt}\begin{bmatrix} v_{sca} \\ v_{scb} \\ v_{scc} \end{bmatrix} = \begin{bmatrix} i_a \\ i_b \\ i_c \end{bmatrix} \begin{bmatrix} 1/C_{sc} \end{bmatrix} \tag{21}$$

Here, i represents the current flowing through the TL, and vsc denotes the voltage across the SC (C_{sc}).

In the grid-side loop, the corresponding equations can be formulated as follows:

$$\frac{d}{dt}\begin{bmatrix} i_a \\ i_b \\ i_c \end{bmatrix} = \begin{bmatrix} i_a & (v_a - v_{sca} - e_a) \\ i_b & (v_b - v_{scb} - e_b) \\ i_c & (v_c - v_{scc} - e_c) \end{bmatrix} \begin{bmatrix} R/L \\ 1/L \end{bmatrix} \tag{22}$$

where v is the voltage at the PCC of the DFIG-WPP, R and L are the total resistance and inductance (inclusive of the inductance of the transformer) of the TL, respectively, and e is the grid voltage.

4.2.4. Modelling of the Transmission System

The PS model described by equations (17)–(22) is nonlinear and time-varying in nature, which poses challenges for implementing straightforward control strategies. To facilitate control design, the model (in *abc* reference frame) is transformed into a time-invariant form using the *dq*-axis transformation, as outlined below:

$$x_{abc} = T_{abc}^{qd} X_{qd} \tag{23}$$

Where represents any signal pertaining to current, voltage or switching behaviour in equations (17)–(22), and transformation matrix $\left(T_{abc}^{qd}\right)$ can be expressed as:

$$T_{abc}^{qd} = \frac{2}{3}\begin{bmatrix} \sin\omega_o t & \sin(\omega_o t - 120°) & \sin(\omega_o t + 120°) \\ \cos\omega_o t & \cos(\omega_o t - 120°) & \cos(\omega_o t + 120°) \\ 1/2 & 1/2 & 1/2 \end{bmatrix} \tag{24}$$

This indicates that the *abc-dq* transformation is carried out using the angular frequency (ω_o) of the TL, with its reference frame rotating in synchronism with the grid.

4.3. Final mathematical equations for PS with SC DFIG-WF

The comprehensive mathematical formulations for the PS featuring SC DFIG-WF are presented in equations (25)–(38), encompassing all relevant mechanical and electrical dynamics of the DFIG-WPP.

$$\omega_{tur}' = \frac{1}{2H_{tur}}\left(\tau_{aer} - K_{stif}\gamma - D_{tur}\omega_{tur}\right) \tag{25}$$

$$\omega_{rot}' = \frac{1}{2H_{gen}}\left(K_{stif}\gamma - \tau_{em} - D_{gen}\omega_{rot}\right) \tag{26}$$

$$\gamma' = 2\pi f\left(\omega_{tur} - \frac{1}{\eta}\omega_{rot}\right) \tag{27}$$

$$I_{gq}' = -\omega_o I_{gd} - \frac{R_{gf}}{L_{gf}} I_{gq} - \frac{V_{gq}}{L_{gf}} + \frac{v_{dc}}{L_{gf}} S_q \tag{28}$$

$$I_{gd}' = -\frac{R_{gf}}{L_{gf}} I_{gd} + \omega_o I_{gq} - \frac{V_{gd}}{L_{gf}} + \frac{v_{dc}}{L_{gf}} S_d \tag{29}$$

$$v_{dc}' = \frac{1}{C} i_{dc} - \frac{1}{C} I_{gq} S_q - \frac{1}{C} I_{gd} S_d \tag{30}$$

$$I_{rq}' = \omega_o I_{rd} - \frac{R_r}{L_r} I_{rq} - \frac{V_{rq}}{L_r} \tag{31}$$

$$I_{rd}' = -\frac{R_r}{L_r} I_{rd} - \omega_o I_{rq} - \frac{V_{rd}}{L_r} \tag{32}$$

$$I_{sq}' = -\omega_o I_{sd} + \frac{R_s}{L_s} I_{sq} - \frac{V_{sq}}{L_s} \tag{33}$$

$$I_{sd}' = \frac{R_s}{L_s} I_{sd} + \omega_o I_{sq} + \frac{V_{sd}}{L_s} \tag{34}$$

$$V_{scq}' = -\omega_o V_{scd} + \frac{1}{C_{sc}} I_q \tag{35}$$

$$V_{scd}' = \omega_o V_{scq} + \frac{1}{C_{sc}} I_d \tag{36}$$

$$I_q' = -\omega_o I_d + \frac{R}{L} I_q + \frac{1}{L}\left(V_q - V_{scq} - E_q\right) \tag{37}$$

$$I_d' = \frac{R}{L} I_d + \omega_o I_q + \frac{1}{L}\left(V_d - V_{scd} - E_d\right) \tag{38}$$

Equations (25)–(38) indicate that the system exhibits nonlinear behaviour, primarily due to the nonlinear characteristics of the switching signals and the converter circuit currents.

4.3.1. Expression for the Power Flow between the WF

The stator is directly connected to the grid, ensuring a stable power supply. The system can provide reactive power compensation via the RSC and GSC, which improves

grid stability and power quality. The active power (P) and reactive power (Q) exchanged between the WF and the grid can be mathematically represented as the following equations:

$$\left.\begin{aligned} P &= \frac{3}{2}\left(V_{sq}I_{sq} + V_{sd}I_{sd} + V_{gq}I_{gq} + V_{gd}I_{gd}\right) \\ Q &= \frac{3}{2}\left(V_{sq}I_{sd} + V_{sd}I_{sq} + V_{gq}I_{gd} + V_{gd}I_{gq}\right) \end{aligned}\right\} \tag{39}$$

From the observations in [54], it is clear that the inherently electrical nature of SSR is often accompanied by coupled torsional oscillations, emphasizing the importance of integrated electro-mechanical modelling for accurate analysis. Accordingly, the proposed controller primarily focuses on regulating the GSC current to govern the switching behaviour of the converter. The q-axis component of the GSC current, I_{gq}, is selected as the main control objective due to its direct coupling with the switching signals. Conversely, the d-axis component, I_{gd}, is disregarded since the d-axis component of the grid voltage is zero [55], rendering its control unnecessary. Furthermore, the controller must effectively regulate V_{dc} to protect the converters from overcurrent, despite its minimal influence on SSR.

4.3.2. Determination of Power Rating for DFIG

During the super synchronous mode of operation, DFIG is capable of delivering power from both the stator and the rotor. As the speed range of the motor is considered between 88 rad/sec and 163 rad/sec, the corresponding slip range for which a DFIG operates is, respectively. The selection of DFIG is done so that rated power gets delivered at the rated speed. DFIG also supplies power from the rotor under the condition of rated power, which is slip times the stator power [12]. The amount of total rated power delivered by DFIG (P_{tot}^{*}) is given as,

$$\left.\begin{aligned} P_{tot}^{*} &= P_{st}^{*} + P_{rot}^{*} = P_{st}^{*} - s^{*}P_{st}^{*} = P_{st}^{*}\left(1 - s^{*}\right) \\ P_{st}^{*} &= \frac{P_{tot}^{*}}{\left(1 - s^{*}\right)} \end{aligned}\right\} \tag{40}$$

where the slip at rated power is represented by s^{*}, which is . Substituting this value in the equation, the rated stator power (P_{st}^{*}) is obtained as 1.1538 MW. Designing a DFIG with a rating of 1.1538 MW is feasible due to the inherent capability of the RSC to handle reactive power requirements. This is a key advantage of DFIG technology.

4.4. Design of DC Link Voltage

The rotor voltage reaches its maximum value at a slip of 0.3, as rotor voltage equals the product of slip and stator voltage. However, as a safety motive attribute, this paper considers the maximum rotor voltage as 575 V instead of 30% of it. For a 575 V system, the maximum rotor voltage is determined as V_{rot}^{max}=575 Volt. The DC link voltage (V_{dc}) is obtained with the following relation as [12],

$$V_{dc} \geq \left(\frac{2\sqrt{2}}{\sqrt{3} \times m} \right) V_{rot}^{\max} \tag{41}$$

where m is the modulation index (m =1), the calculated DC link voltage, determined by substituting appropriate values into the equation (41), is 938.9711 V. In this configuration, a safety factor of 22.5% is incorporated, leading to a selected DC link voltage of 1150 V.

4.5. Design of Transformers and VSC Rating

The system is designed to accommodate single-phase loads within a three-phase, four-wire distribution network, utilizing the neutral point provided by the three-phase transformer. Since the DC link voltage opted is 1150V, the voltage on the low voltage (LV) side winding $\left(V_{xfmr}^{LV}\right)$, as per the equation (41) must be lower than 704 V (~61.25% of 1150 V). The final value of $\left(V_{xfmr}^{LV}\right)$, is chosen as 575 V (i.e. 81.68% of 704 V). Therefore, a 115.5 MVA, 161/0.575 kV Δ-Y transformer is employed in this system since we are considering the grid voltage as 161 kV. The rating of the GSC is selected as 1.1538 MVA, which corresponds to the maximum stator power when the load is disconnected. The current rating (in rms) of GSC is thus calculated as [12],

$$I_{GSC}^{rms} = \frac{VA_{GSC}}{\sqrt{3} \times V_{xfmr}^{LV}} = \frac{1.1538 \times 10^6}{\sqrt{3} \times 575} = 1158.5161 \text{ A} \tag{42}$$

Now, the peak current of GSC $\left(I_{GSC}^{pk}\right)$, is calculated as,

$$I_{GSC}^{pk} = \sqrt{2} \times I_{GSC}^{rms} = \sqrt{2} \times 1158.5161 \text{ A} = 1638.3892 \text{ A} \tag{43}$$

Next, considering a 7% ripple content in the peak-to-peak GSC current I_{GSC}^{pp}, we obtain the peak-to-peak current ripple as,

$$I_{GSC}^{pp} = 7\% \; of \; 1638.3892 \text{ A} = 114.6872 \text{ A} \tag{44}$$

The current rating for each of the Insulated Gate Bipolar Transistors (IGBTs) used in the GSC, after considering a safety factor of 30% is determined as follows [12],

$$I_{GSC}^{IGBT} = 1.3 \times \left\{ I_{GSC}^{pk} + I_{GSC}^{pp} \right\} \tag{45}$$

Substituting the values from equations (43) and (44) into equation (45), we obtain , the maximum current rating of each IGBT in GSC is 2278.9993 A. Therefore, a 2300 A current rating IGBT is chosen.

The voltage rating of the IGBT depends on the DC link voltage. For instance, if 1265 V is the maximum voltage across the DC link (V_{DC}^{max}), the IGBT's voltage rating (considering a safety factor of 30%) would be 1.3 x 1265 V = 1644.5 V. Thus, an IGBT with 1800 V as a voltage rating is chosen. MG7405WZ is a suitable module available in the market.

The maximum real and reactive power flow through the RSC determines its volt-ampere (VA) rating. The maximum real power flowing through the RSC at (s*) is calculated as,

$$\left.\begin{aligned} P_{tot}^{*} &= P_{st}^{*} + P_{rot}^{*} = \left(-\frac{P_{rot}^{*}}{s^{*}}\right) + P_{rot}^{*} = P_{rot}^{*}\left(1-\frac{1}{s}\right) \\ \underset{\substack{\textit{Maximum real power}\\ \textit{flow via RSC}}}{P_{rot}^{*}} &= P_{tot}^{*}\left(\frac{s^{*}}{s^{*}-1}\right) = 1.5\text{ MW}\left(\frac{-0.3}{-0.3-1}\right) = 0.3462\text{ MW} \end{aligned}\right\} \quad (46)$$

The control algorithm for the RSC is designed to supply the required magnetization current to the DFIG. Based on the machine parameters, the DFIG draws a lagging reactive power of 0.78 MVAr during motoring mode, which is supplied by the RSC from the rotor side. The rated rotor reactive power (Q_{rot}^{*}) at maximum slip (s*) is calculated,

$$Q_{rot}^{*} = s^{*} \times 0.78\text{ MVAr} = 0.234\text{ MVAr} \quad (47)$$

The overall rating of the RSC is then calculated as,

$$VA_{RSC} = \sqrt{\left(P_{rot}^{*}\right)^{2} + \left(Q_{rot}^{*}\right)^{2}} = \sqrt{0.3462^{2} + 0.234^{2}} = 0.4178641\text{ MVA} \quad (48)$$

Furthermore, the current rating of the RSC I_{RSC}^{rms} is calculated as:

$$I_{RSC}^{rms} = \frac{VA_{RSC}}{\sqrt{3} \times V_{rot}^{\max}} = \frac{417864.1}{\sqrt{3} \times 575} = 419.5721\text{ A} \quad (49)$$

Next, the peak current of RSC $\left(I_{RSC}^{pk}\right)$ is computed as follows,

$$I_{RSC}^{pk} = \sqrt{2} \times I_{RSC}^{rms} = \sqrt{2} \times 419.5721\text{ A} = 593.3645\text{ A} \quad (50)$$

Thereafter, considering a 7% ripple content in the peak-to-peak RSC current $\left(I_{RSC}^{pp}\right)$, we obtain the peak-to-peak current ripple as,

$$I_{RSC}^{pp} = 7\%\ of\ \ 593.3645\text{ A} = 41.5355\text{ A} \quad (51)$$

The current rating for each of the IGBTs in the RSC (I_{RSC}^{IGBT}), incorporating a safety factor of 30%, is determined as follows:

$$I_{RSC}^{IGBT} = 1.3 \times \left\{ I_{RSC}^{pk} + I_{RSC}^{pp} \right\} \tag{52}$$

Substituting the values from equations (50) and (51) into equation (52), it can obtain (I_{RSC}^{IGBT}), the maximum current rating of each IGBT in RSC is 825.37 A. The voltage rating, similar to that of the GSC, is selected as 1800 V. AMM800GA176D is a suitable module available in the market.

4.6. Linearized System Modelling and Eigenvalue Analysis for System Stability Assessment

This section presents the theoretical validation of the time-domain simulation results through eigenvalue analysis. The objective is to assess the dynamic behaviour and stability of the DFIG-based system under various conditions, including SSR and fault-induced disturbances. To facilitate this, the system is linearized around a defined operating point, and its dynamics are represented in the standard state-space form:

$$\left.\begin{aligned} \dot{X} &= AX + BU \\ Y &= CX + DU \end{aligned}\right\} \tag{53}$$

Here, **X** denotes the state vector, **U** the input vector, **Y** the output vector, and **A**, **B**, **C** and **D** are the constant matrices derived from the linearized model of the system.

The state vector **X** consists of electrical and mechanical dynamic states such as rotor current components (i_{dr}, i_{qr}), rotor speed deviation ($\Delta\omega_r$), and in some cases, DC-link voltage variation (ΔV_{DC}), enabling detailed modelling of the DFIG under transient events. These variables collectively and comprehensively capture the internal dynamics of the DFIG under transient grid perturbations.

The input vector **U**, on the other hand, primarily includes the control voltages applied to the rotor windings (v_{dr}, v_{qr}) and the mechanical torque input (T_m), which is typically derived from the incident wind speed (v_{win}). Although wind speed is not a state variable, it plays a crucial role in shaping system dynamics by affecting the mechanical power extracted from the wind.

The output vector **Y** includes the observable system responses such as the rotor speed (ωr), voltage magnitude of one of the phases (v_{a_mag}), current magnitude of one of the phases (i_{a_mag}), electromagnetic torque response (T_{em}), the active and reactive powers injected into the grid (P_g, Q_g) and DC-link capacitor voltage (V_{DC}).

State vector (**X**):

$$X^T = \begin{bmatrix} i_{dr} & i_{qr} & \Delta\omega_r & \Delta V_{DC} \end{bmatrix} \tag{54}$$

Input vector (**U**):

$$U^T = \begin{bmatrix} v_{dr} & v_{qr} & T_m \left(or\ v_{win} \right) \end{bmatrix} \tag{55}$$

Output vector (**Y**):

$$Y^T = \begin{bmatrix} \omega_r & v_{a_mag} & i_{a_mag} & T_{em} & P_g & Q_g & V_{DC} \end{bmatrix} \tag{56}$$

A Matrix (*4* × *4*) – State to State Dynamics:

$$A = \begin{bmatrix} -\frac{R_r}{L_r} & \omega_s & \frac{L_m}{L_r} i_{qs} & 0 \\ -\omega_s & -\frac{R_r}{L_r} & -\frac{L_m}{L_r} i_{ds} & 0 \\ 0 & 0 & -\frac{D}{2H} & \frac{1}{2H} \frac{dT_{em}}{dV_{DC}} \\ 0 & 0 & -\frac{1}{C_{DC}} \frac{dP_r}{d\omega_r} & -\frac{1}{R_{DC} C_{DC}} \end{bmatrix} \tag{57}$$

Here R_r, L_r are the rotor resistance and inductance, L_m is the mutual inductance, H is the inertial constant, D represents the mechanical damping, C_{DC}, R_{DC} are the DC-link capacitor and resistor, $\frac{dT_{em}}{dV_{DC}}$ shows the sensitivity of torque to DC-link voltage, and $\frac{dP_r}{d\omega_r}$ denotes the sensitivity of rotor-side active power to rotor speed.

B Matrix (*4* × *3*) – Inputs to State Dynamics:

$$B = \begin{bmatrix} \frac{1}{L_r} & 0 & 0 \\ 0 & \frac{1}{L_r} & 0 \\ 0 & 0 & \frac{1}{2H} \\ 0 & 0 & 0 \end{bmatrix} \tag{58}$$

C Matrix (*7* × *4*) – States to Output Mapping:

$$C = \begin{bmatrix} 0 & 0 & 1 & 0 \\ \frac{dv_{a_mag}}{di_{dr}} & \frac{dv_{a_mag}}{di_{qr}} & 0 & 0 \\ \frac{di_{a_mag}}{di_{dr}} & \frac{di_{a_mag}}{di_{qr}} & 0 & 0 \\ \frac{dT_{em}}{di_{dr}} & \frac{dT_{em}}{di_{qr}} & 0 & 0 \\ \frac{dP_g}{di_{dr}} & \frac{dP_g}{di_{qr}} & \frac{dP_g}{d\omega_r} & 0 \\ \frac{dQ_g}{di_{dr}} & \frac{dQ_g}{di_{qr}} & \frac{dQ_g}{d\omega_r} & 0 \\ 0 & 0 & 0 & 1 \end{bmatrix} \tag{59}$$

D Matrix (*7* × *3*) – Direct Input to Output Feedthrough:

$$D = \begin{bmatrix} 0 & 0 & 0 \\ \frac{dv_{a_mag}}{dv_{dr}} & \frac{dv_{a_mag}}{dv_{qr}} & 0 \\ \frac{di_{a_mag}}{dv_{dr}} & \frac{di_{a_mag}}{dv_{qr}} & 0 \\ \frac{dT_{em}}{dv_{dr}} & \frac{dT_{em}}{dv_{qr}} & 0 \\ \frac{dP_g}{dv_{dr}} & \frac{dP_g}{dv_{qr}} & 0 \\ \frac{dQ_g}{dv_{dr}} & \frac{dQ_g}{dv_{qr}} & 0 \\ 0 & 0 & 0 \end{bmatrix} \tag{60}$$

To compute the system eigenvalues, the linearized state-space model is first converted into its corresponding transfer function representation. From this, the characteristic equation is obtained by evaluating the denominator polynomial, whose roots yield the eigenvalues (or poles) of the system. These eigenvalues typically appear in complex conjugate pairs of the form $\lambda=\alpha\pm j\beta$, where α represents the real part and β the imaginary component. The time-domain behaviour of each mode can be expressed as $e^{\lambda t}=e^{\alpha t}e^{j\beta t}$, illustrating that the real part governs the exponential growth or decay of the response, while the imaginary part determines its oscillatory nature. A positive α implies

divergence and instability, whereas a negative α leads to exponential damping and stability. If α=0, the system remains marginally stable, exhibiting sustained oscillations without decay. For the system to be entirely stable, all eigenvalues must lie strictly in the left half of the complex plane, ensuring that every mode exhibits decaying behaviour over time.

In this work, the linearized state-space model is first obtained using MATLAB/Simulink's Model Linearizer app, with the linearization performed at 6 second, a point selected to capture the system's dynamic behaviour during the SSR/faulted condition. This linear model is then converted into its corresponding transfer function representation.

After presenting a detailed modelling of the system, the following chapter introduces the design methodology of the proposed control strategies.

CHAPTER 5. DESIGN OF THE CONTROLLER

5.1. Comparative Analysis of PI-Based and VI-Based SDCs for SSR Mitigation in DFIG-WPPs

This study presents a comprehensive time-domain comparative analysis of various control strategies deployed at different locations within a DFIG-WF. The evaluation focuses on conventional PI-based controllers implemented at the GSC and RSC, as well as a proposed Virtual Impedance-based Sub-Synchronous Damping Controller (VISDC). The analysis is conducted using a modified IEEE-FBM, a well-established test system widely utilized for investigating SSR phenomena. SSR poses a significant challenge in SC-TNs, often leading to adverse interactions between the electrical grid and the mechanical drivetrain of WTs—an issue particularly pronounced in systems employing DFIGs.

Due to their partial electrical decoupling from the grid's rotational inertia, DFIGs inherently lack the natural inertial response characteristic of synchronous generators, rendering them vulnerable to frequency instabilities during rapid grid disturbances. To address this vulnerability, the proposed VISDC incorporates a VI emulation mechanism within the RSC. This emulation enables DFIG-WTs to actively participate in frequency regulation by momentarily adjusting power output in response to frequency deviations. The integration of VI not only enhances system frequency stability but also contributes to effective SSR damping, thereby improving the dynamic resilience and overall robustness of the PS.

5.2. Control Scheme for RSC

Figure 5-1 presents the control scheme of the RSC, which plays a pivotal role in managing the dynamic performance of a DFIG-WECS. The RSC is responsible for three main objectives: (i) supplying the reactive power required to maintain the stator terminal voltage at nominal levels, thereby supporting voltage stability and enabling near-unity power factor operation; (ii) maintaining system frequency despite fluctuations in wind speed and grid load; and (iii) regulating rotor speed to ensure Maximum Power Point Tracking (MPPT), which is essential for maximizing energy capture under varying wind conditions.

The control strategy is based on a Stator Flux Oriented Control Scheme (SFOCS), where the rotor current is decomposed into two orthogonal components: the direct-axis component (i_{dr}) aligned with the stator flux, and the quadrature-axis component (i_{qr}) perpendicular to it. This decoupled approach allows independent control over the active and reactive power. The electromagnetic torque, which is a function of the stator flux and (i_{qr}), can be precisely managed to regulate rotor speed. Simultaneously, (i_{dr}) is controlled to manage the reactive power. Error signals from active and reactive power are processed through PI controllers to generate reference currents, which are then converted into voltage commands and fed into a PWM block via the Inverse Park transformation. This enables accurate switching of the IGBTs in the RSC, ensuring smooth and efficient dynamic response, stability, and optimal power extraction under all operating conditions. The expression for electromagnetic torque can be given as,

$$\tau_{em} = \left(\frac{3}{2}\right)\left(p_{pairs}\right)\left(\phi_{st}^{d}\right)\left(i_{qr}\right) \tag{61}$$

where, τ_{em} represents the electromagnetic torque, φ_{st}^{d} is the d-axis component of the stator flux and p_{pairs} represents the number of pole pairs of the DFIG.

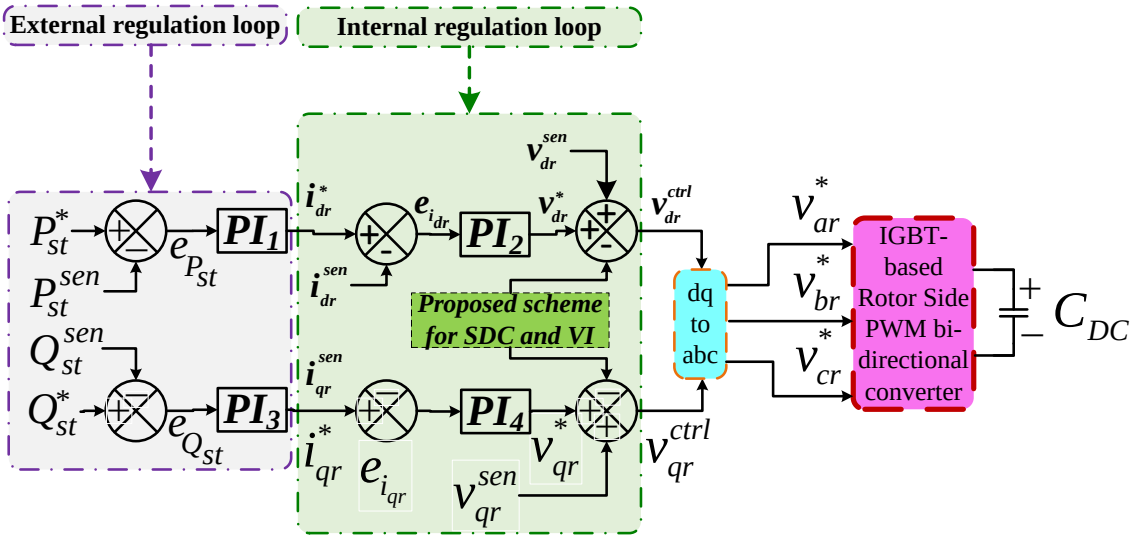

Figure 5-1. Control Scheme for RSC

In the SFOCS of the RSC, the reference rotor currents (i_{dr}^{*} and i_{qr}^{*}) are derived by processing the error signals between the desired and actual active and reactive powers of the stator. These error signals are fed into two separate PI controllers to generate the appropriate current references for controlling the electromagnetic torque and reactive power. The calculated reference currents are then compared with the actual rotor current

values, and the resulting current errors are again processed through a second set of PI controllers. This results in the generation of reference rotor voltages for both the d-axis and q-axis components. These voltage signals are transformed into three-phase stationary frame voltages using the Inverse Park Transformation. Finally, these voltages are modulated using a high-frequency triangular carrier signal to produce PWM signals, which are used to control the six IGBTs of the RSC for precise switching.

5.3. Control Scheme of GSC

Figure 5-2 shows the control scheme of the GSC that is primarily focuses on regulating the voltage across the DC-link capacitor. Maintaining a constant DC-link voltage is essential for ensuring that the RSC receives a stable DC supply, enabling it to generate a constant-amplitude AC voltage. This, in turn, ensures a steady magnetic flux within the DFIG, which is critical for maintaining efficient power conversion and precise control of active and reactive power exchange with the grid. To achieve this, the reference d-axis component of the grid current is determined by evaluating the error between the measured DC-link voltage and its reference value. This error is processed through a PI controller to produce the required active power control signal. For reactive power control, the q-axis reference is typically set to zero, aiming for unity power factor operation. The resulting d- and q-axis current references are then compared with the actual current measurements. The errors are passed through another set of PI controllers to compute the control voltages. These voltages are modulated to generate reference signals, which are then compared against a high-frequency triangular carrier waveform to produce PWM signals that control the six IGBTs of the GSC, ensuring stable grid interfacing.

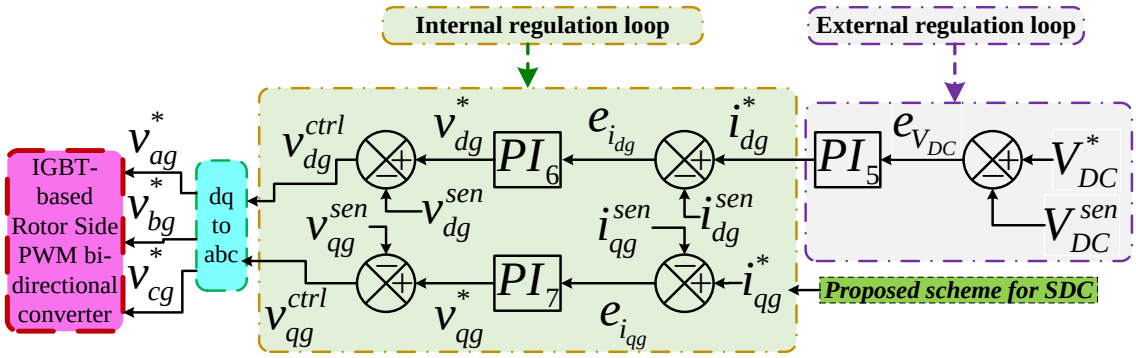

Figure 5-2. Control Scheme for GSC

5.4. Proposed Supplementary Damping Control Scheme

Figure 5-3 illustrates the proposed SDC integrated into the GSC as part of the overall strategy for SSR mitigation and dynamic stability enhancement. The central idea of this control scheme is to introduce an intelligent damping mechanism that responds adaptively to the system's critical operating parameters. In this design, a composite error signal is formulated by combining two key error inputs: (i) the difference between the reference stator voltage and the actual sensed stator voltage (v_{st}^{*} and v_{st}^{sen}), and (ii) the deviation in rotor speed, calculated as the error between the reference rotor angular speed and the actual rotor speed. These two signals represent the electrical and mechanical disturbances, respectively, that commonly arise during SSR events or grid disturbances. These error components are summed and passed through a PI controller, denoted as PIGSC. The controller processes these deviations to generate a corrective signal that is used as the reference value for the quadrature-axis component of the grid current (i_{qg}^{*}). This reference current is essential for dynamically regulating the reactive power contribution from the GSC, thereby improving voltage stability and introducing targeted damping to suppress SSOs. This strategy ensures rapid and adaptive control action while preserving the stability of the entire DFIG-WECS.

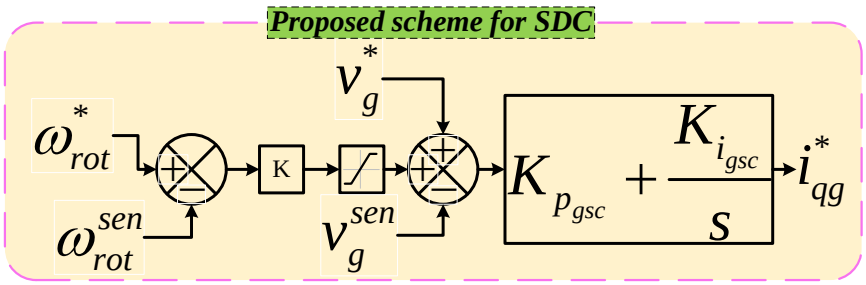

Figure 5-3. Proposed Control Scheme for GSC

In the case of the RSC, as depicted in Figure 5-4, the proposed SDC is designed to enhance the system's dynamic response by directly influencing rotor-originated SSOs. The architecture includes an additional summer block strategically positioned after the third and fourth PI controllers in the control loop. This summer block performs a summation of three critical signals: (i) the reference direct-axis rotor voltage, (ii) the actual sensed rotor voltage, and (iii) the output from the proposed PI controller (PI_{RSC}). The output of the summer block dynamically adjusts the control signal used to modulate the rotor voltage, allowing real-time response to grid and mechanical disturbances. The PIRSC itself receives as input the error signal derived from the difference between the reference rotor

speed and the actual sensed rotor speed (ω_{rot}^{*} and ω_{rot}^{sen}). By processing this rotational speed deviation, the PI controller generates a corrective signal that supports stabilising the generator's electromagnetic torque and rotor current under transient or faulty conditions. This supplementary loop adds an additional layer of robustness and responsiveness to the RSC, allowing the system to effectively damp rotor-induced oscillations and maintain operational stability even under severe grid disturbances or SSR conditions.

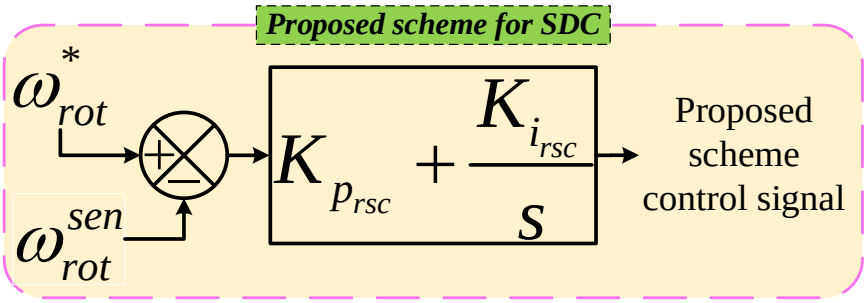

Figure 5-4. Proposed SDC Scheme for RSC

In this work, the *d*-axis component of the rotor current is selected as the input signal for the Virtual Impedance-based Sub-Synchronous Damping Controller (VISDC). Figure 5-5 depicts the proposed VISDC for RSC. This choice is technically justified by the fact that the *d*-axis rotor current in a DFIG is directly linked to the rotor-side active power exchange and reflects dynamic interactions between the rotor and the grid, particularly under sub-synchronous conditions. Unlike the *q*-axis current, which predominantly governs reactive power control, the *d*-axis current is more sensitive to active power oscillations that are characteristic of SSR. Leveraging this sensitivity allows the VISDC to detect and respond more effectively to SSOs. Moreover, since the RSC primarily controls the rotor current components in the synchronously rotating reference frame, incorporating the *d*-axis current enables the controller to modulate electromagnetic torque in real time, thereby damping TIs between the electrical and mechanical subsystems. This approach ensures a more responsive and targeted mitigation strategy, enhancing the robustness of the DFIG-based WF under SC grid conditions.

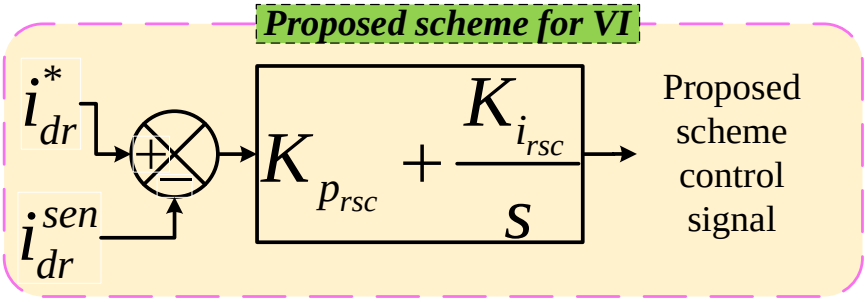

Figure 5-5. VISDC Scheme Proposed for RSC

The functional flow of the proposed SDC schemes is concisely illustrated in Figure 5-6, which provides a step-by-step visualization of signal acquisition, processing, and control action. The figure offers a high-level overview of how the controllers detects perturbations, processes them through a damping logic structure, and applies the necessary impedance correction via the GSC/RSC. This visual representation is intended to complement the theoretical exposition, allowing readers to quickly grasp the control loop structure and its integration into the overall DFIG system.

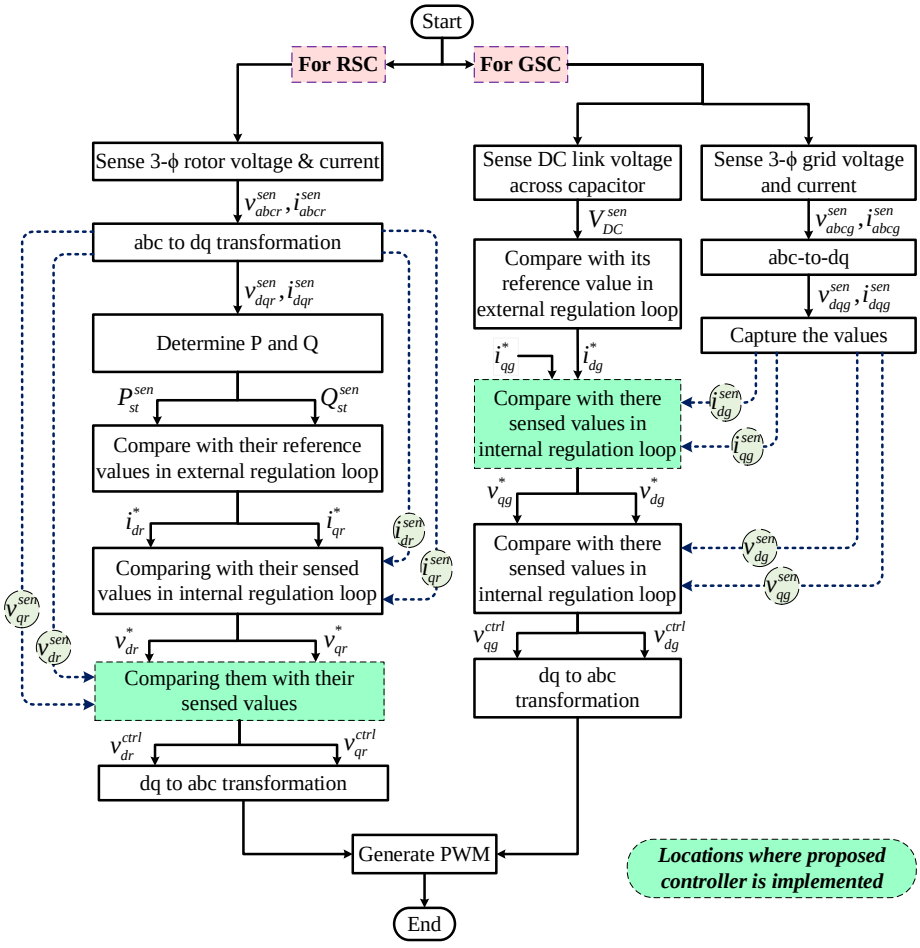

Figure 5-6. Flow chart of the control scheme for the DFIG-based WTG, along with the placements of proposed controllers SDC and VISDC

5.4.1. Controller Parameter Selection and Tuning

The effectiveness of the implemented control schemes depends significantly on the appropriate tuning of PI controller parameters. In this study, all PI controllers associated with the RSC, GSC, and the proposed VISDC (in RSC) are tuned based on the time-domain response and SSR sensitivity of the DFIG-based system using the *Ziegler-Nichols tuning method*. This well-established approach facilitates systematic parameter selection to ensure both stability and dynamic responsiveness.

The *Ziegler-Nichols method* was chosen for its balance between simplicity and practical performance, especially in systems where damping of oscillatory modes is crucial. After initial system response evaluation, the PI parameters were refined through simulation-based validation to improve the damping of SSOs while maintaining acceptable transient and steady-state characteristics.

The finalized controller gains used in the simulation studies are presented in Table 5-1 below:

To maintain consistency and ensure comparability across different control locations, the tuning process involved an iterative approach focused on achieving a desirable trade-off between fast dynamic response and system stability. For each controller, the proportional gain K_p was selected to ensure a sufficiently fast rise time, while the integral gain K_i was tuned to eliminate steady-state error and reduce oscillatory behaviour caused by SSIs.

Table 5-1. Tuned PI Controller Gains for RSC, GSC, and VISDC Schemes

Controller	Control Objective	Proportional Gain (K_p)	Integral Gain (K_i)
GSC-PI	DC-link voltage and reactive power control	1.55	5
RSC-PI	Rotor current regulation and active power control	0.006	0.35
VISDC	Damping SSR using i_{dr} injection	0.6	0.35

The parameters were chosen to provide adequate dynamic performance across a range of operating conditions, including wind speed variations and grid disturbances. Specifically, for the VISDC, tuning was focused on achieving accurate tracking of sub-

synchronous frequency components via *d*-axis rotor current modulation, thereby ensuring effective damping without compromising the PS's transient response.

5.4.2. Controller Tuning Methodology Using Modified Ziegler–Nichols Approach

1. **Initial Setup:** Set the integral gain $K_i = 0$ (or equivalently, make $T_i = \infty$) so that the controller behaves as a *P-only* controller.
2. **Incremental Gain Testing:** Gradually *increase the proportional gain* K_p from a small value while observing the system's time-domain response (e.g., rotor current, DC-link voltage, or power output, depending on the controller location).
3. **Identify Sustained Oscillations:** Continue increasing K_p until the output begins to exhibit *sustained, consistent oscillations* (neither decaying nor growing). This is the point where the system is at the edge of stability, known as the *ultimate point*.
4. **Apply Empirical Multipliers (*Ziegler–Nichols Rules*):** Once the critical gain is identified (internally), apply standard *Ziegler–Nichols* empirical formulas to set the controller gains:

   For a **PI controller**:

   - $K_p = 0.45 \times K_u \rightarrow$ approximated internally (or the gain a which sustained oscillations occurred)
   - $T_i = P_u/1.2$
   - $K_i = K_p/T_i$ (approximate $T_i \approx 2 \times T_{osc}$ i.e. the oscillation period)
5. **Validate and Fine-Tune:** Simulate the controller with the tuned values and observe its performance. You may perform *slight adjustments* based on desired rise time, overshoot, settling time, or damping characteristics, especially for SSR scenarios.

Building upon the controller designs discussed in this chapter, the following chapter presents a comprehensive analysis of the results obtained through detailed simulations and real-time validation using the OPAL-RT testbed. The performance of the proposed control strategies is critically assessed under various operating scenarios, including different compensation levels and fault conditions, to verify their effectiveness and robustness.

CHAPTER 6. RESULTS AND DISCUSSIONS

6.1. Real-time validation using OPAL-RT

This section presents the real-time validation of the MATLAB/Simulink-based model using the OPAL-RT real-time simulation environment. The objective is to verify the feasibility, performance, and stability of the proposed VISDC strategy under practical operating constraints. A dedicated HIL testbench was developed using the OPAL-RT 4610 XG system, which enables high-fidelity execution of complex PS models in real time. The overall deployment was carried out through RT-LAB 2024 v1.2.2, with a fixed simulation step size of 20 μs, selected to maintain numerical stability and ensure synchronization with the hardware interface.

The host system used for model development and control console functions was configured with 32 GB RAM, an Intel Core i7 processor, and Windows 11 (64-bit) operating system, running MATLAB/Simulink R2023a. The Simulink model was appropriately partitioned into the SM_Master and SC_Console subsystems, with each assigned to separate processor cores within the OPAL-RT framework to optimize execution efficiency. The model was compiled into C-code and deployed onto the real-time target for deterministic simulation.

To visualize and analyze real-time responses, a 4-channel Tektronix MDO3000 Mixed Domain Oscilloscope was interfaced through OPAL-RT's 16-channel Analog Output Interface Card (AOIC) analog output channels. All key signals, such as electromagnetic torque, power flow, and grid-injected voltage and current, were captured and verified against their offline simulation counterparts. The results revealed a high degree of correlation, thereby confirming the accuracy and stability of the real-time implementation. Minor signal conditioning was required to map the model outputs to OPAL-RT's operating voltage range of -16 V to +16 V, which was achieved by introducing suitable gain adjustments within the Simulink environment. Figure 6-1 shows the entire experimental setup for the OPAL-RT.

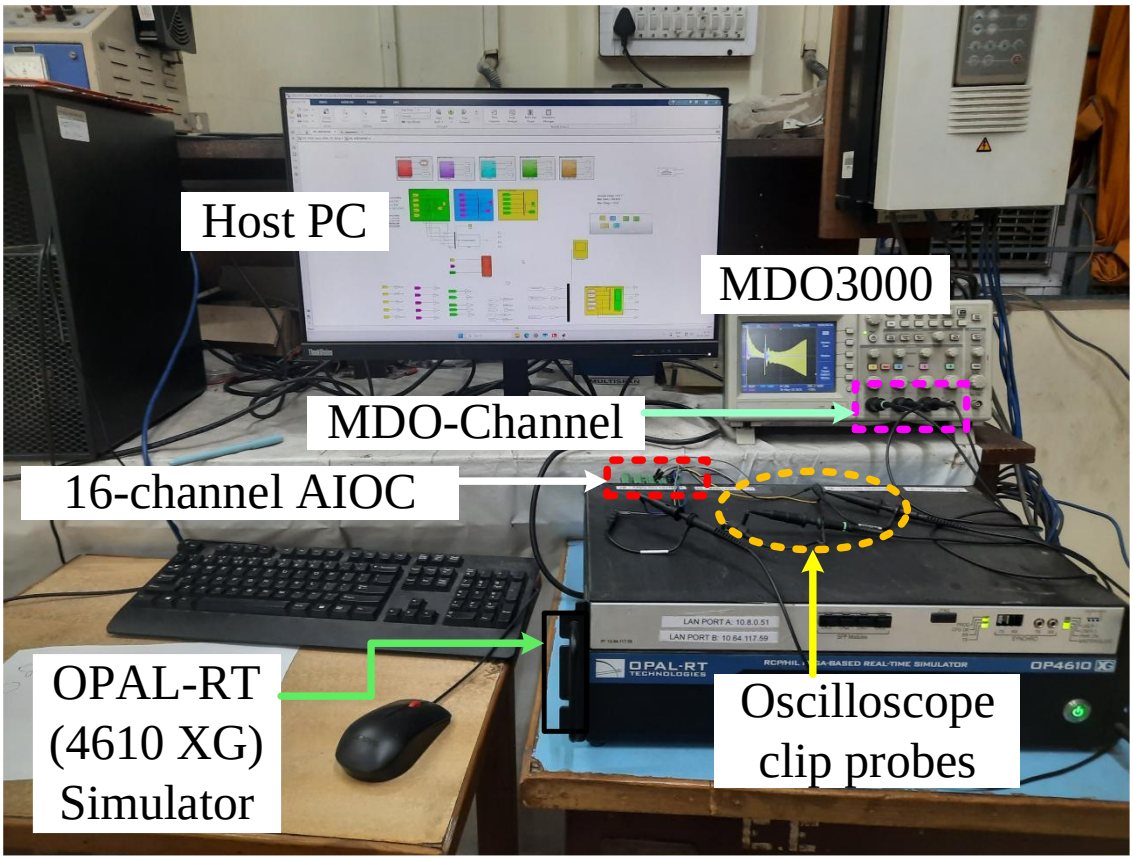

Figure 6-1. Experimental RT-Lab Configuration Using OPAL-RT for Real-Time Verification of the Proposed System

6.2. System under study

In the modelled system, a 100 MW aggregated WF, composed of 67 DFIG units each rated at 1.5 MW, is connected to an infinite bus (representing the utility grid) via a coupling transformer, as shown in Figure 6-2. This transformer steps up the generated voltage from 575 V (typical for DFIG stator and rotor terminals) to 161 kV, facilitating efficient long-distance power transmission. The transformer is rated at 115.5 MVA to match the WF's power output. The internal architecture of the WF includes various subsystems such as the WT aerodynamics, shaft system drivetrain (comprising the hub and multistage step-up GB), induction generator, and PECs (RSC and GSC) interconnected by a DC-link capacitor. Power from the stator is directly injected into the grid via the transformer, while the rotor energy is controlled by the RSC and routed through the DC-link to the GSC before being supplied to the grid. The bi-directional converters are regulated using dedicated control schemes tailored to optimize dynamic response and SSR mitigation.

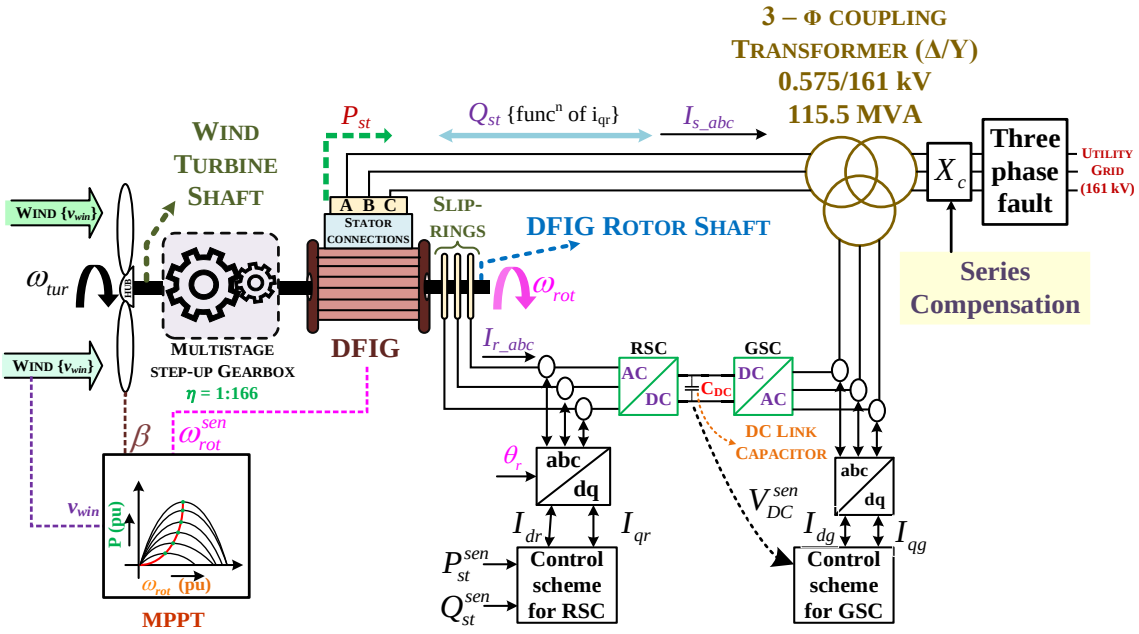

Figure 6-2. Schematic of DFIG-WPS

To rigorously test the robustness of the proposed controller, the study introduces varying levels of SC into the transmission system. These compensation levels are used to replicate different grid scenarios, including those likely to induce SSR. Furthermore, a symmetrical three-phase fault is simulated at 2.5 seconds and cleared at 2.6 seconds to assess the system's resilience under severe fault conditions. The results demonstrate that the proposed VISDC significantly improves the system's damping, reduces settling times, and enhances post-fault recovery, validating its effectiveness in real-world applications.

All the results figures attached are captured using the Mixed Domain Oscilloscope (MDO), and the simulations are performed on OPAL-RT setup (Figure 6-1).

6.3. Varying Compensation Levels:

To thoroughly evaluate the effectiveness of different control strategies in mitigating SSR and enhancing system stability, four scenarios were analysed using time-domain simulations of a DFIG-WF. The system is subjected to two sudden changes in SC: A sudden compensation changes from 2% to 20% (at t = 2 s) and from 20% to 60% (at t = 4 s) to study the behaviour of the system. After 4 seconds, the system becomes unstable, as in cases (1) and (2). To overcome this, a damping controller is implemented in cases (3) and (4). These cases are carried out for SSR and transient stability, and detailed explanations are as follows

Case (1): Without any Controller.

Case (2): SDC Implemented Only at GSC.

Case (3): SDCs Implemented at Both RSC and GSC.

Case (4): VISDC Implemented at RSC.

This setup emulates realistic post-disturbance behaviour in PSs where WFs may remain connected through a single transmission corridor, increasing their vulnerability to SSR. A constant wind speed of 9 m/s is assumed to isolate the impact of compensation on system dynamics, as SSR develops on a rapid timescale when compared to the variation in wind speed. The response is measured by the WF power flow of the active power flow (P), and the reactive power flow (Q) is given in Figure 6-3 and Figure 6-4. Additionally, Figure 6-5 illustrates the electromagnetic torque (Te) of the WF while Figure 6-6 to Figure 6-7 display the magnitude of the stator current and stator voltage (V and I) of the DFIG-based WF.

The detailed explanation is as follows:

Case (1): This baseline scenario reflects a WF operating without any supplementary damping or VI control. At 2% to 20% compensation, the system tolerates the change, though small oscillations emerge in torque and current. However, the sudden increase to 60% compensation at t = 4 s triggers uncontrolled oscillations in all monitored parameters. Figure 6-3 and Figure 6-4 shows the active and reactive power that exhibits erratic swings, losing sinusoidal behaviour. Figure 6-5 illustrates electromagnetic torque and oscillates with increasing amplitude, indicative of positive feedback leading to SSR. PCC voltage and current fluctuate sharply, risking equipment insulation failure and converter shutdown, as shown in Figure 6-6 and Figure 6-7. These oscillations do not decay and instead escalate, leading to system-wide instability. The absence of any control highlights the system's inability to self-stabilise under severe compensation-induced disturbances. A system without control is highly sensitive to abrupt SC, especially under radial connection, confirming the necessity of damping strategies.

The main drawbacks that have existed in case (1) are the damping mechanism to suppress SSOs. After the increase to 60% SC, oscillations grow uncontrollably. The system becomes completely unstable, with significant power swings, voltage/current distortion, and torque fluctuations. The next is provided the complete lack of SSR mitigation demands the introduction of a damping controller. Basic control must be explored to suppress the dangerous oscillations initiated by SC and fault conditions.

Case (2): In this scenario, a damping controller is placed only at the GSC, as commonly seen in several conventional approaches. The initial compensation increase to

20% is better managed than in Case (1), with slightly damped oscillations. After the jump to 60%, however, the controller's limitation becomes evident: The active and reactive power outputs become unstable and begin to oscillate with high amplitude again, as shown in the Figure 6-3 and Figure 6-4. Figure 6-5 to Figure 6-7 depicts the torque, current, and voltage oscillations re-emerge and amplify gradually after a short period of attenuation. Since the origin of SSR is in the rotor, and GSC primarily regulates DC link voltage and reactive power injection, it lacks direct control over the dynamics causing instability. Although some improvement is observed, a GSC-only controller is insufficient to suppress rotor-based SSR, especially in post-fault and high-compensation scenarios. Improvements over case (1): some initial attenuation of oscillations after the 20% compensation step and better behaviour than no control at all. The main drawback occurred in case (2) takes place due to ineffective protection against rotor-induced SSR, which is the root cause. GSC primarily controls DC-link voltage and reactive power, not rotor dynamics. After 60% compensation, oscillations return and grow, showing delayed instability. The next case overcomes the drawback, such as the GSC-only control proving insufficient. SSR mitigation requires control at the origin (i.e., the rotor). Necessity for coordinated control for RSC and GSC to cover broader dynamic ranges.

Case (3): This approach places damping controllers on both the rotor-side and grid-side converters, enabling shared regulation over the rotor dynamics and grid interface. At both 20% and 60% compensation, the system shows substantial improvement: the active/reactive power fluctuations settle within acceptable bounds and torque oscillations are noticeably reduced, as shown in Figure 6-3 to Figure 6-5. Voltage and current at the PCC maintain sinusoidal form with limited peak overshoots, as shown in Figure 6-6 and Figure 6-7. While there is some initial disturbance after the 60% compensation jump, the system stabilizes within 5.447 seconds, showcasing good damping characteristics. The dual-controller setup successfully addresses both grid-side disturbances and rotor-induced SSR. Coordinated placement of SDCs at RSC and GSC offers a balanced solution, significantly reducing SSR and enhancing transient response.

Improvements over case (2): Substantial damping of SSR oscillations. Better settling times (~5.4 s) and limited overshoots. The system maintains stability even after 60% compensation. Weaknesses have existed in the case (3), that is, increased complexity due to the need for two controllers. Dual-controller coordination requires careful tuning and higher computational overhead. While effective, it's not optimal for real-time

implementation in large-scale, distributed WFs. Lacks additional benefits such as inertia emulation needed in weak grids. To overcome all these, case (4) is carried out to provide a more efficient and scalable solution. Desire to include VI, improve response time, and simplify the control architecture with RSC-only placement. Motivation to reduce hardware/software complexity while enhancing robustness.

Case (4): This case deploys a VISDC exclusively at the RSC. The controller dynamically modulates torque output using rotor KE to emulate inertial response while damping SSOs. Across both compensation events, the system exhibits superior dynamic performance: Power, torque, voltage, and current oscillations are quickly damped, as shown in Figure 6-3 to Figure 6-7. The system returns to steady-state conditions within 4.125 seconds, the fastest among all cases. Peak overshoot in torque and speed is limited to under 7%, ensuring mechanical integrity. No reappearance of oscillations post-fault or during sustained high compensation levels. The placement of the VISDC at the RSC allows direct control over the electromechanical interaction between the DFIG rotor and the series-compensated grid. VISDC offers a scalable and practical solution for WFs exposed to fault-induced disturbances, especially when radially connected. It provides both synthetic inertia and effective SSR suppression, bridging the gap between transient support and sustained stability.

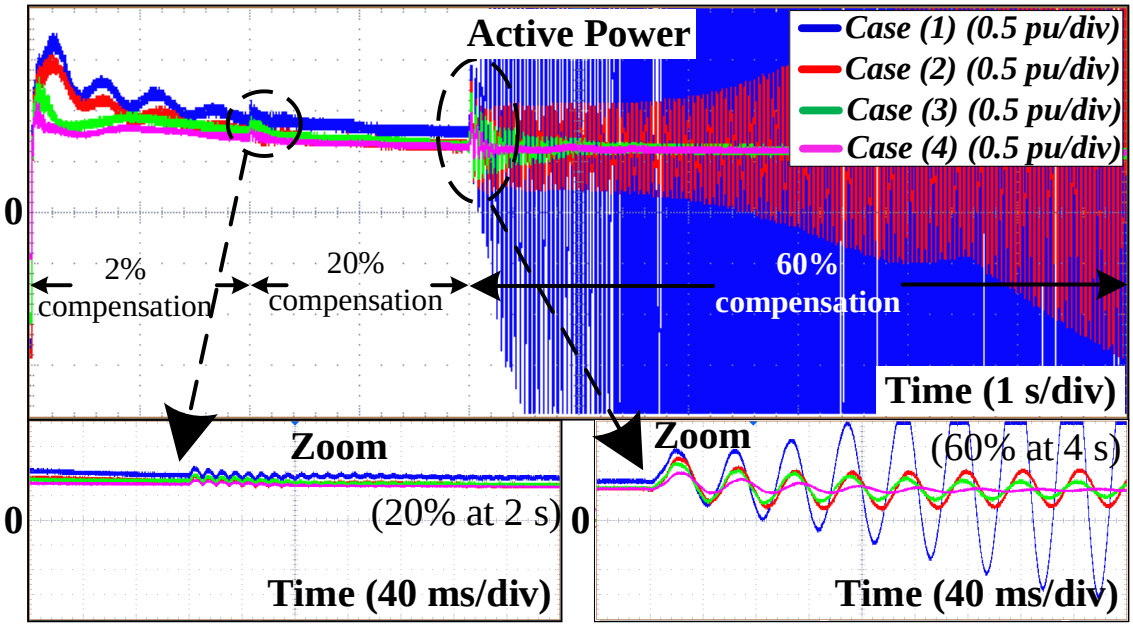

Figure 6-3. Active power in pu of DFIG response subject to varying compensation levels

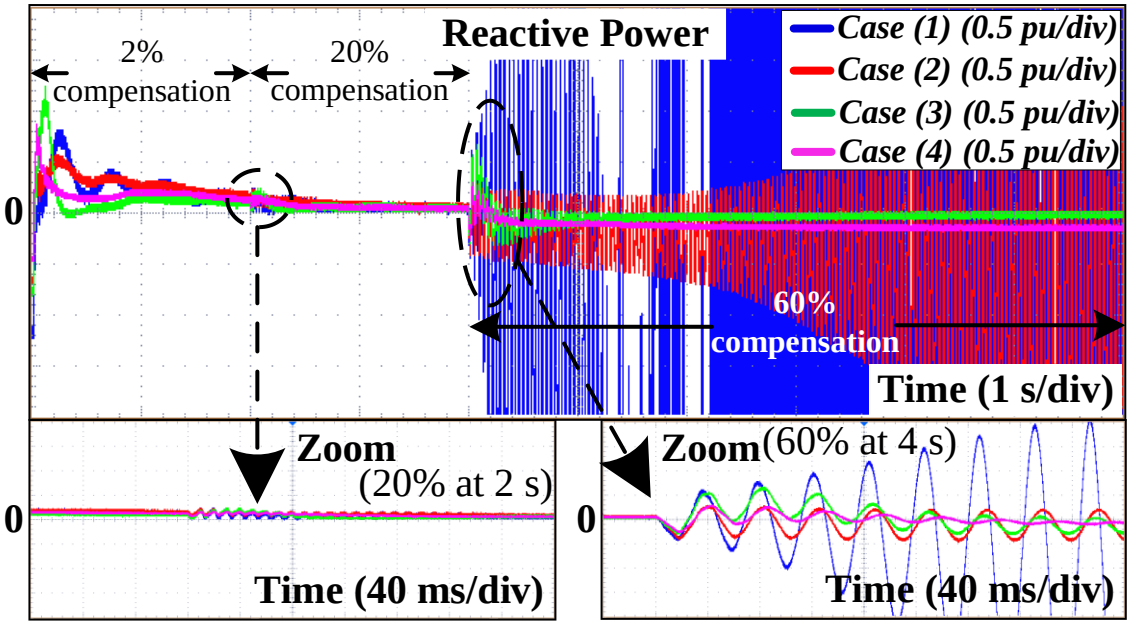

Figure 6-4. Reactive power in pu of DFIG response subject to varying compensation levels

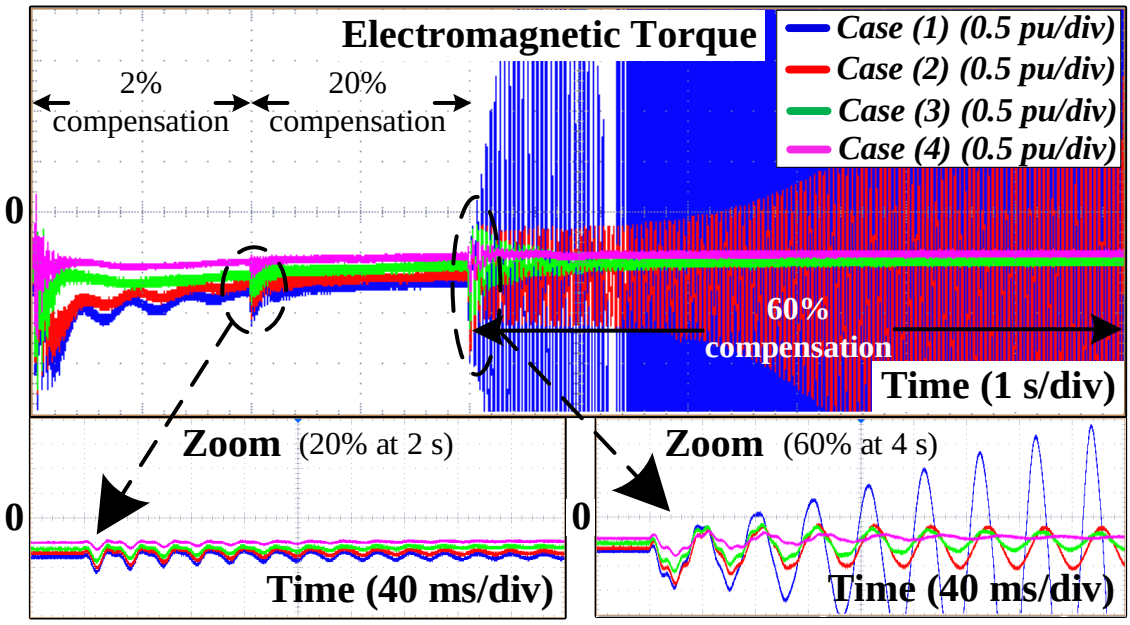

Figure 6-5. Electromagnetic torque in pu of DFIG response subject to varying compensation levels

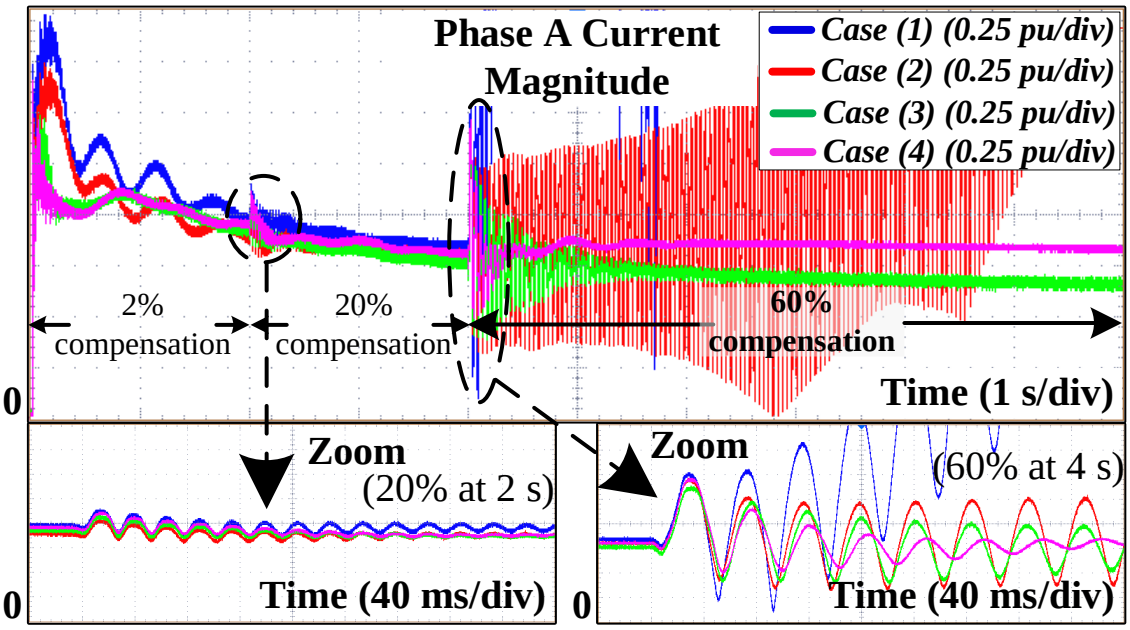

Figure 6-6. Phase 'A' current magnitude in pu of DFIG response subject to varying compensation levels

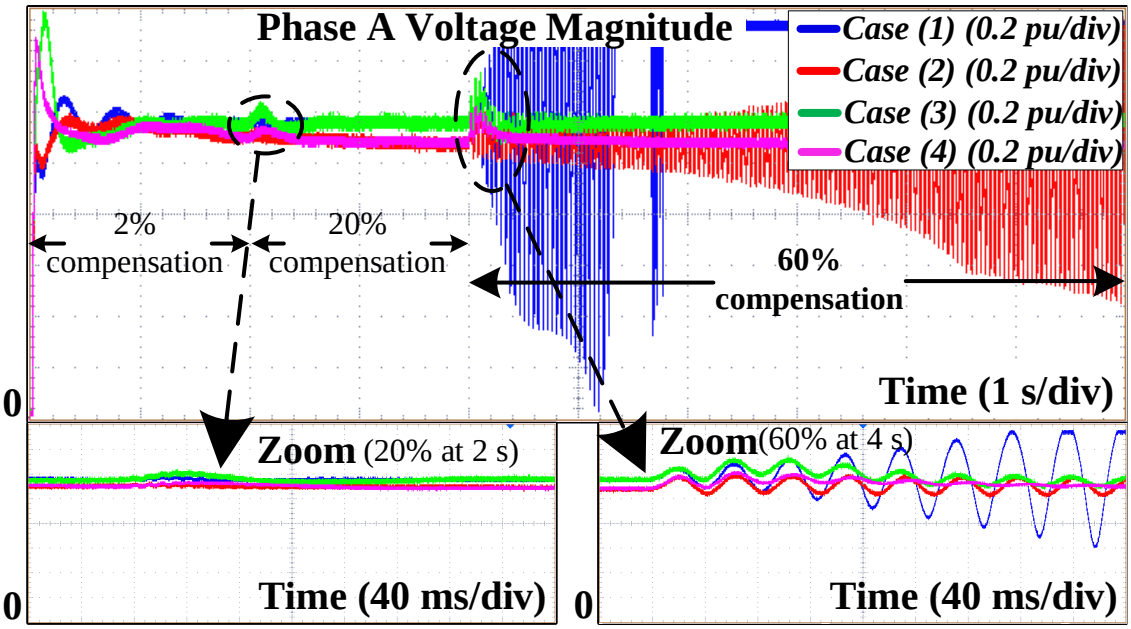

Figure 6-7. Phase A voltage magnitude (in pu) of DFIG response subject to varying compensation level

To evaluate the effectiveness of different SSR mitigation strategies, a structured and unified comparative analysis is performed under varying SC levels. The analysis is designed to reflect both moderate (20%) and high (60%) compensation scenarios, thereby

capturing the dynamic transition from a stable to a potentially unstable operating regime. This approach enables the observation of sub-synchronous oscillation behaviour as well as the responsiveness of different controllers, including the proposed VISDC approach, to such perturbations.

Table 6-1 summarizes the system response and performance across four distinct cases, each representing a progressively enhanced control strategy. The table highlights critical aspects such as damping behaviour, transient response, and the system's ability to suppress SSR-induced instabilities. It also serves to contextualize the advantages and limitations of each approach, providing insight into control placement, coordination complexity, and overall robustness under weak-grid conditions. This comparison facilitates an informed assessment of the trade-offs involved in controller design and underlines the effectiveness of the proposed solution.

Table 6-1. Enhanced Unified Comparative Analysis & Control Strategy Progression for Varying Compensation Levels

Cases and Control strategy	Initial compensation (20%) at t = 2 sec	High compensation (60%) at t = 4 sec	System behaviour and performance	Remark
Case (1): No Controller	No immediate instability, but no damping either	Severe instability: SSR grows rapidly, power and torque fluctuations	(a) No SSR mitigation (b) Unstable voltage, current and torque oscillations	Introduce basic damping to avoid catastrophic instability
Case (2): GSC-only SDC	Minor damping observed, slight improvement	Delayed instability: oscillations reappear and grow after ~6s	(a) GSC cannot directly influence rotor-originated SSR (b) The system becomes unstable again	Need RSC-based damping to act directly at the source of SSR
Case (3): SDC at Both RSC and GSC	Stable, good damping with slight overshoot	Stable but with moderate overshoot and settling (~5.4 s)	(a) Significant SSR mitigation. (b) High complexity due to dual-controller coordination	Simplify control structure while adding VI capabilities
Case (4): VISDC at RSC (Proposed)	Smooth response, minimal overshoot, fast stabilization	Very effective damping, minimal overshoot (<7%), fast settling (< 4.125 s), stable performance under extreme SC	(a) Combines inertia and damping (b) Simple structure with RSC-only control	Optimal solution: robust, scalable, suitable for real-time weak-grid deployment

6.4. Transient Analysis

To comprehensively validate the superior performance and fault-tolerant capability of the proposed VISDC located at the RSC, an extensive robustness assessment was carried out. A symmetrical fault was deliberately introduced at t = 2.5 seconds and cleared at t = 2.6 seconds. This type of fault is widely recognized as the most severe and critical form of disturbance in PSs, owing to its ability to cause maximum short-circuit current, deep voltage collapse, and abrupt system dynamics that test the limits of controller adaptability. Such fault events are not only rare but also high-impact, especially in systems where WFs are connected radially through series-compensated TLs, a configuration that is inherently susceptible to SSR and post-fault transient instability. The following cases have been carried out to study the efficiency of the controller as follows:

Case (A): No Controller.

Case (B): GSC-Based Controller Only.

Case (C): SDC at Both GSC and RSC.

Case (D): Proposed VISDC at RSC.

The stator voltage and current at PCC are depicted in Figure 6-8 and Figure 6-9. Additionally, Figure 6-10 to Figure 6-12 illustrate the active power flow, reactive power flow and electromagnetic torque of DFIG-based WF.

The detailed explanation is as follows:

In **Case (A)**, where no controller is integrated into the system, the impact of a symmetrical three-line-to-ground fault on the wind PS is significantly severe. During the fault event, there is an abrupt and sharp voltage sag at the PCC, which leads to substantial instability across the system, as depicted in Figure 6-8. The fault results in an uncontrolled surge of current, causing stress on both the generator and the grid infrastructure, as depicted in Figure 6-9. The electromagnetic torque becomes highly oscillatory due to the lack of a damping mechanism, and the active and reactive power flows exhibit severe, undamped fluctuations, as shown in Figure 6-10 to Figure 6-12. These unstable behaviours continue even after the fault is cleared, demonstrating the system's inability to recover on its own. Oscillations persist in the voltage, current, torque, and power profiles, with no indication of a settling tendency. The absence of any SDC results in unmitigated rotor-originated oscillations, further amplifying the impact of the fault. Additionally, the generator becomes highly vulnerable to mechanical stress due to unregulated torque variations, posing a serious threat to the operational lifespan and reliability of the system.

This case underscores the system's susceptibility to dynamic disturbances and highlights the critical need for implementing appropriate damping controllers. The results make it evident that, without active control mechanisms, the system cannot maintain stability under fault conditions, thereby necessitating the introduction of advanced controllers to ensure robust operation and mitigate the effects of SSR.

In **Case (B)**, the system incorporates a controller solely at the GSC, which provides marginal improvements in fault response compared to the uncontrolled **Case (A)**. During the three-line-to-ground fault, the GSC-based controller helps in regulating the DC-link voltage and improves the grid voltage and current profile to some extent, as depicted in Figure 6-8 and Figure 6-9. However, the key rotor-side dynamics, particularly electromagnetic torque and rotor speed oscillations, remain largely unaddressed, as shown in Figure 6-12. As a result, while active and reactive power flow shows signs of initial stabilization, it fails to maintain a consistent and steady trajectory post-fault, as depicted in Figure 6-10 and Figure 6-11. The oscillations are momentarily suppressed but re-emerge due to the lack of direct control over the rotor circuit, indicating incomplete damping. The settling time remains relatively high at around 4.0 sec, and the peak overshoot in power and torque parameters, though reduced compared to **Case (A)**, still lies in the range of 100–120%, signifying continued instability risks. A key limitation of this case is that the GSC-based controller affects only grid-side parameters and cannot mitigate SSR originating from rotor-side interactions with the series-compensated line. As a result, despite modest performance gains, the system remains insufficiently robust under severe disturbances, underscoring the need for RSC-based control for effective SSR mitigation.

Case (C) introduces coordinated SDCs at both the GSC and RSC, yielding substantial improvements in dynamic performance during and after fault conditions. When subjected to a symmetric fault, the system demonstrates a well-regulated response in both voltage and current, with transients effectively contained, as observed in Figure 6-8 and Figure 6-9. The electromagnetic torque and active/reactive power deviations are notably suppressed, showing the system's enhanced ability to handle disturbances, as shown in Figure 6-10 to Figure 6-12. Post-fault, the system exhibits visible damping of oscillations and quickly settles to a stable operating point, with a significantly improved settling time of approximately 3.6 seconds. The peak overshoot across key parameters is greatly reduced to the range of 20–40%, indicating enhanced control over dynamic fluctuations. The key advantage in this setup lies in the synergistic action of GSC and RSC controllers,

which enables comprehensive damping of SSO modes and bolsters transient response under compensated line conditions. However, this dual-controller architecture adds complexity to the overall control scheme and increases computational demands, which may pose challenges in real-time applications or under fast-varying grid disturbances. Despite its effectiveness, **Case (C)** is not entirely optimal for highly stressed or weak grid scenarios, leading to the motivation for a more adaptive and intelligent control framework, such as a VI-based strategy integration for achieving improved stability with reduced system complexity.

In **Case (D)**, the system employs the proposed VISDC exclusively at the RSC, demonstrating the most effective and resilient performance across all evaluated scenarios. During the symmetrical three-line-to-ground fault, system variables such as voltage, current, active power flow, reactive power flow and rotor electromagnetic torque show minimal deviations, highlighting the controller's strong ability to stabilize rotor-originated dynamics, as shown from Figure 6-8 to Figure 6-12. The embedded VI provides a crucial buffering effect by temporarily storing and releasing KE, thereby reducing the rate of change in key parameters and limiting the system's exposure to abrupt transients. Following fault clearance, the system exhibits the fastest and most stable recovery among all four cases, with a significantly reduced settling time of approximately 3.1 to 3.15 seconds. The peak overshoot is well-controlled, remaining within 25%, while THD drops below 5%, reflecting improved power quality and waveform integrity. This approach directly targets SSR by damping oscillations at their origin within the rotor circuits, unlike GSC-based methods. Furthermore, the VISDC enhances system robustness even under severe grid conditions, including weak and remote networks. Overall, **Case (D)** presents a superior control strategy, offering an optimal combination of high damping effectiveness, fast stabilization, enhanced power quality, and reduced control system complexity. It stands out as the most promising solution for modern wind-integrated PSs.

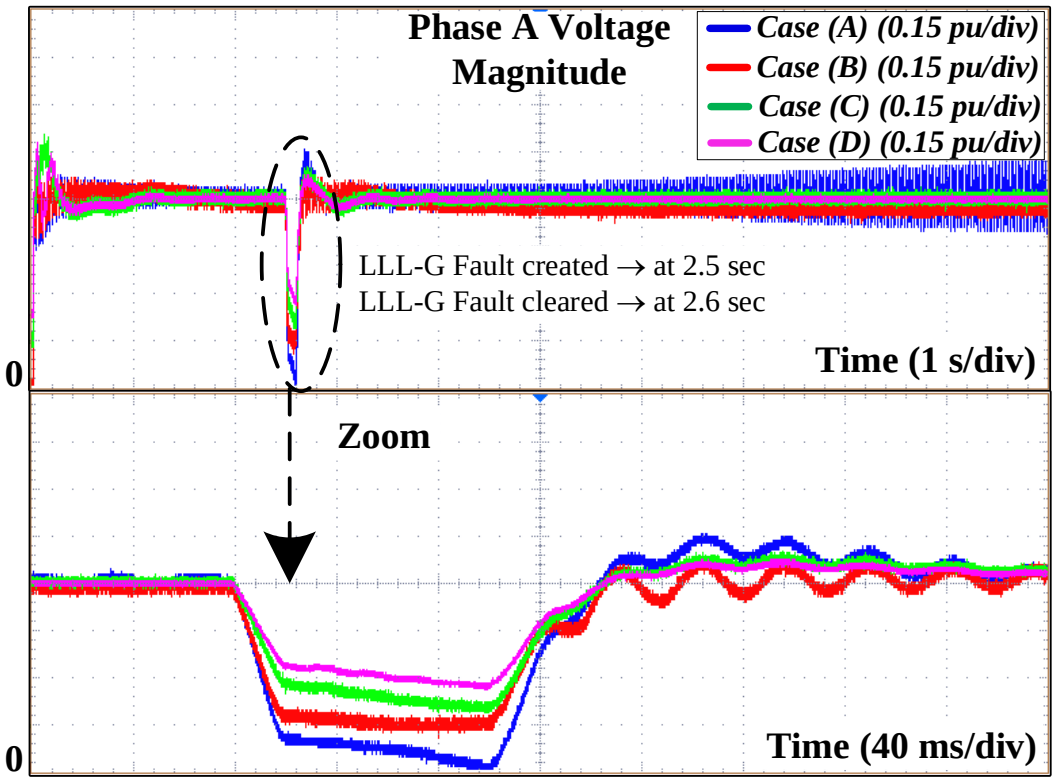

Figure 6-8. Phase A voltage magnitude in pu of DFIG response subject to LLLG fault

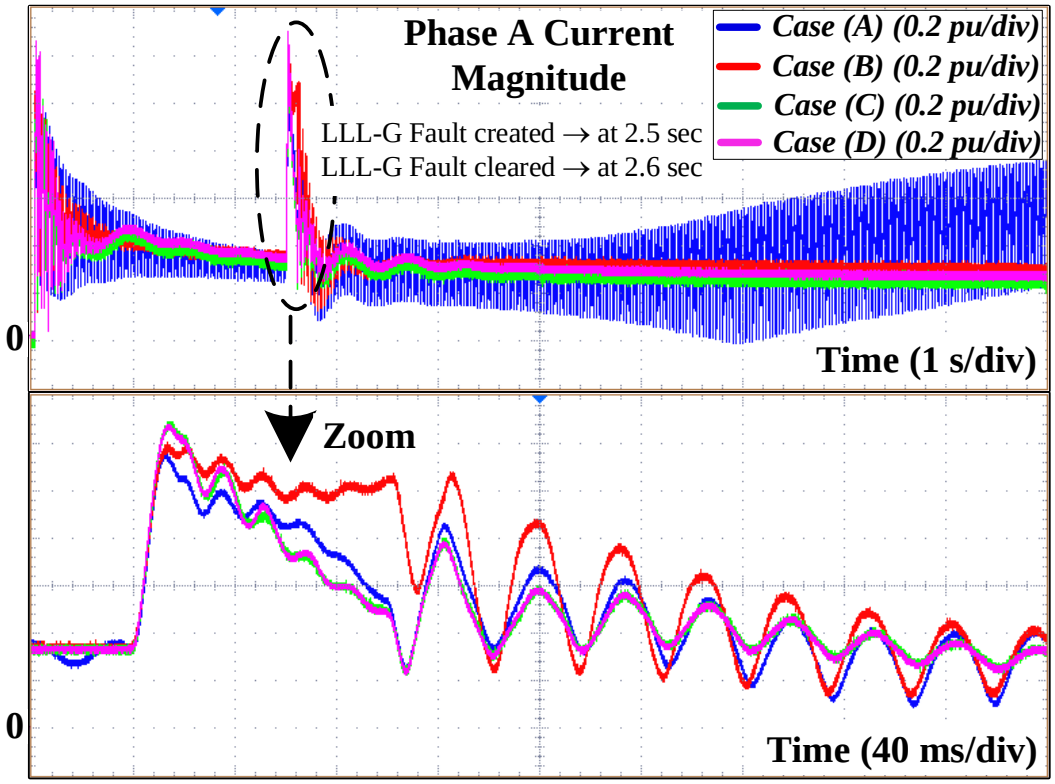

Figure 6-9. Phase A current magnitude in pu of DFIG response subject to LLLG fault

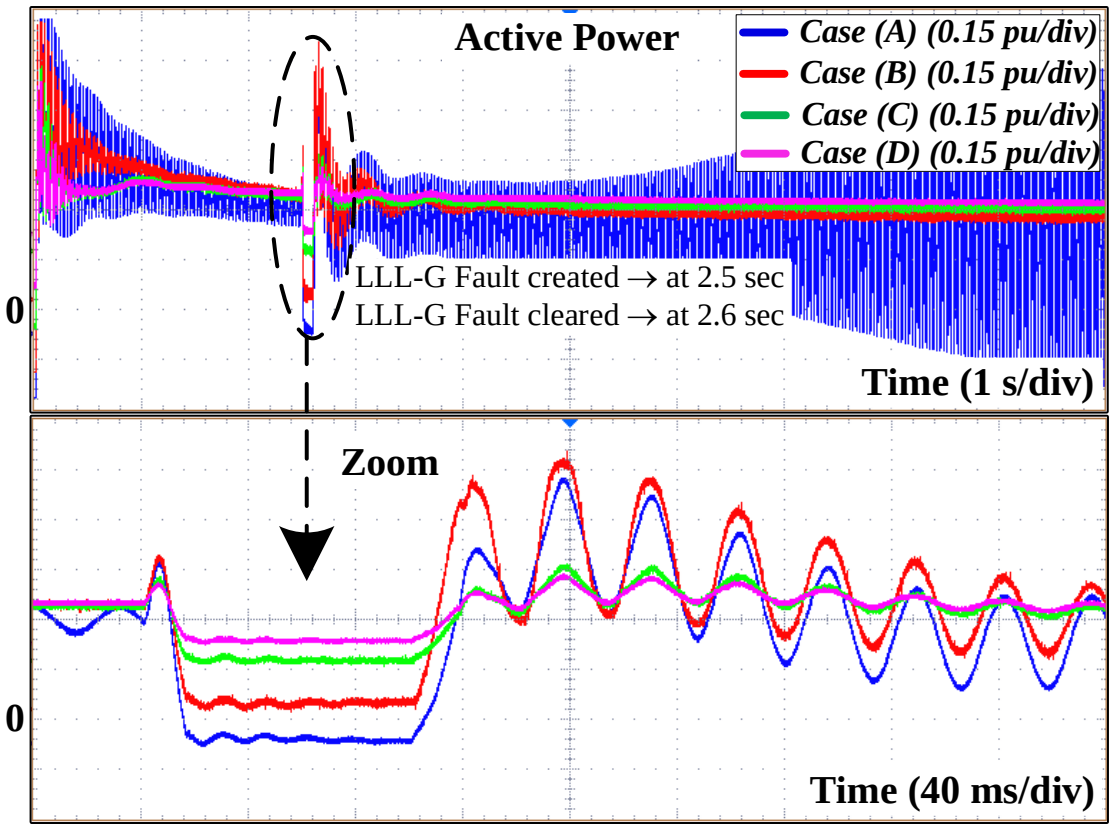

Figure 6-10. Active power in pu of DFIG response subject to LLLG fault

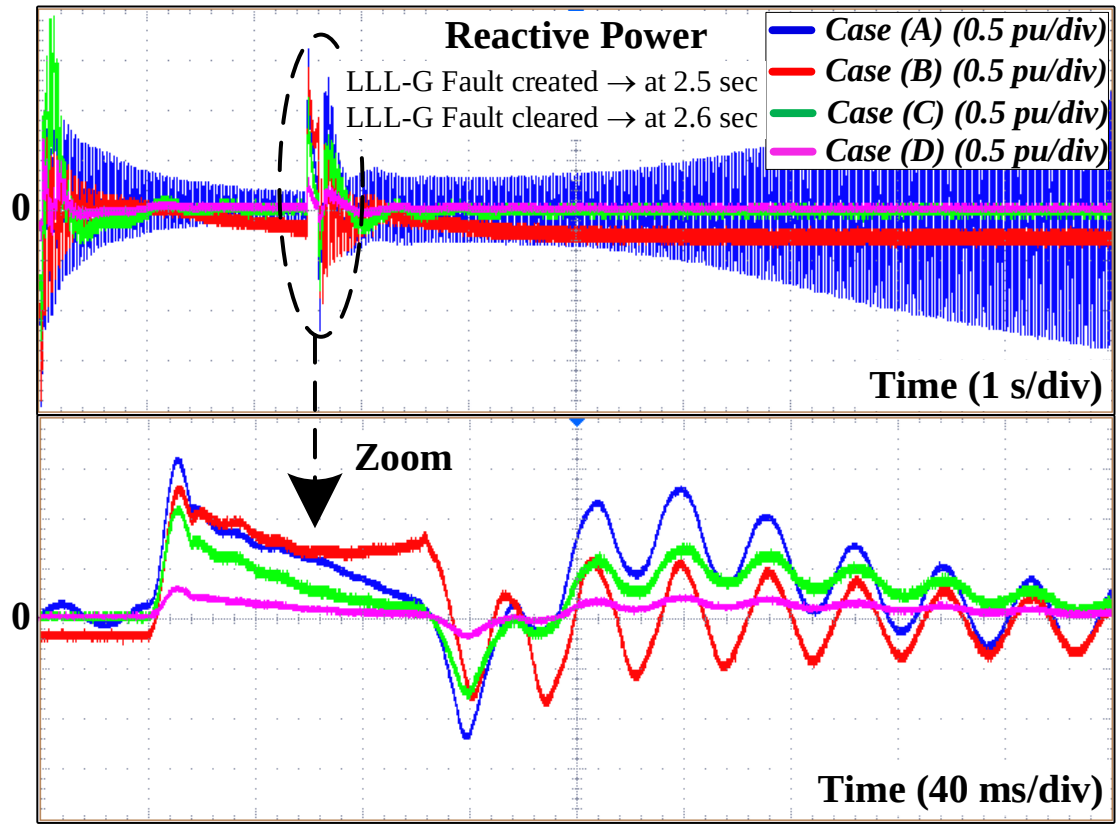

Figure 6-11. Reactive power in pu of DFIG response subject to LLLG fault

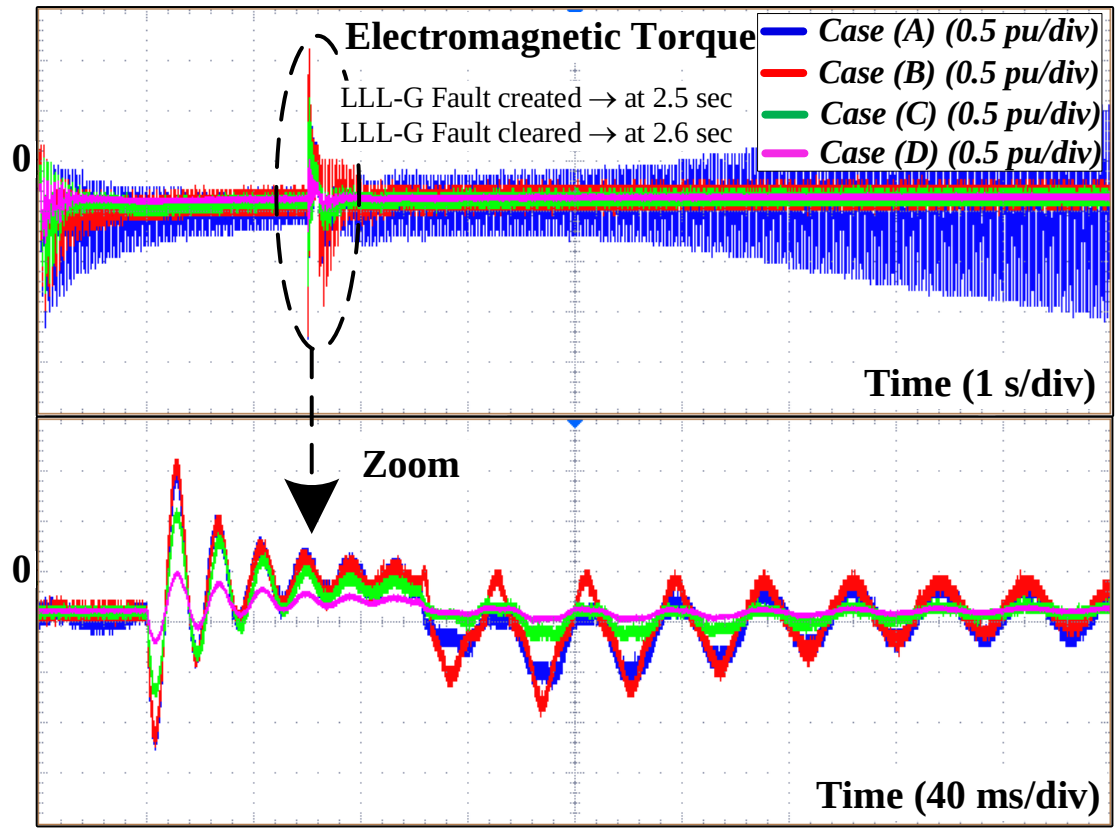

Figure 6-12. Electromagnetic torque in pu of DFIG response subject to LLLG fault

To further validate the proposed controller's effectiveness, a comparative assessment is conducted under faulted grid conditions, where transient disturbances such as voltage sag and fault current surges are more pronounced. This analysis highlights each strategy's ability to suppress SSR and maintain system stability during and after a severe grid disturbance. Key performance metrics such as oscillation damping, peak overshoot, settling time, and the severity of voltage and current deviations are closely observed.

Table 6-2 presents a consolidated overview of the system's transient response across four control scenarios, ranging from no control to the proposed VISDC implementation. Each case captures the system's behaviour under identical fault conditions, allowing for a direct comparison of damping performance, fault containment, and post-fault recovery. The results clearly indicate the progressive enhancement in stability and dynamic performance with each control upgrade, with the proposed VISDC strategy at the rotor-side converter offering the most robust and efficient solution. This assessment underscores the controller's real-time applicability and resilience in fault-prone, weak-grid environments.

Table 6-2. Comparative Case-Wise Controller Performance Evaluation for Transient Analysis

Cases and Controller Location	Fault Current Surge	Voltage Sag	Oscillation Damping	Settling Time	Peak Over-shoot	Fault Response	Remarks and Stability
Case (A): No controller	Very High	Severe	None	>10 s	>150%	Severe voltage drops, uncontrolled currents, and SSR excitation	No damping; system collapse, likely unstable
Case (B): GSC only	High	Moderate	Weak	~4 s	~57%	Minor improvements; rotor remains unstable	GSC alone is insufficient, Marginally Stable
Case (C): RSC + GSC	Moderate	Controlled	Good	~3.5 s	~25%	Controlled fault response; improved damping	More complex but effective Stable
Case (D): VISDC at RSC	Low	Mild	Excellent	~3.1–3.15 s	~12%	Minimal deviation, strong damping during/after fault	Best performance and robustness, Highly Stable

6.4.1. Performance Evaluation of System Parameters Under Severe Grid Faults (LLLG)

To comprehensively evaluate the system's dynamic behaviour under severe grid disturbances, a detailed time-domain analysis was conducted for a three-phase symmetrical (LLLG) fault condition. The fault scenario, considered one of the most critical for WPPs, was applied at the HV side of the TL under 60% SC, an SSR-prone setting. The fault was introduced at 2 seconds and cleared at 2.1 seconds. System responses across four controller configurations—no controller (**Case (A)**), GSC-only SDC (**Case (B)**), RSC+GSC SDC (**Case (C)**), and the proposed RSC-based VISDC (**Case (D)**)—were examined. The analysis focused on key electrical and mechanical parameters such as stator voltage, electromagnetic torque, active/reactive power, and stator current.

Table 6-3 summarizes the percentage of dip/spike during fault, post-fault undershoots and overshoots, and the settling time for each parameter and case. It is evident that **Case (D)**, with the VISDC integrated into the RSC, outperforms all other

configurations across most metrics. Notably, this configuration significantly suppresses torque spikes, mitigates voltage sags, and ensures the fastest recovery with minimal overshoot, thereby affirming its robustness and superior damping characteristics. These insights not only validate the proposed control strategy's effectiveness under real-world fault scenarios but also highlight its potential in enhancing the fault ride-through (FRT) capability of DFIG-WFs.

Table 6-3. Key Transient response parameters subject to LLLG fault

Parameter	Case	Dip/Spike during fault (%)	Undershoot post-fault clearance (%)	Overshoot post-fault clearance (%)	Settling time (sec)
Voltage (v_a_mag)	A	88.1261	5.8701	20.2226	>10
	B	74.7991	22.0682	13.4819	5.337
	C	50.0819	7.9273	18.3594	4.110
	D	43.8584	6.0428	14.5567	3.504
Electromagnetic Torque (T_{em})	A	343.9075	138.4453	80.3571	>10
	B	396.1883	268.834	93.5874	4.188
	C	281.1791	104.6485	19.8344	3.726
	D	11.2706	35.0849	10.9422	2.752
Active Power (P)	A	120	56.92	123.54	>10
	B	100	40.6651	173.8137	4.92
	C	50	10.4649	97.2611	4.118
	D	20	7.1166	28.1007	3
Reactive Power (all values in pu)	A	0.8187	-0.614	0.662	>10
	B	0.7663	-0.517	0.344	4.539
	C	0.7516	-0.5999	0.428	3.44
	D	0.218	-0.1003	0.234	2.9
Current (i_a_mag)	A	267.5241	69.0675	172.8938	>10
	B	283.3442	56.2622	243.5409	4.609
	C	273.1908	26.9644	148.7055	3.761
	D	267.548	20.5053	133.9572	3.482

6.5. Eigenvalue Analysis

The eigenvalues ($\lambda = \alpha \pm j\beta$) of the different cases have been obtained for SSR analysis and transient analysis by linearization of the system. A total of 104 and 97 eigenvalues were obtained for the SSR and fault scenarios, respectively. Only the four most dominant poles from each case are analysed and presented in Table 6-4 to maintain clarity and avoid interpretative complexity. The corresponding oscillation frequencies $\left\{f_r = \frac{\beta}{2\pi}\right\}$ and damping ratios $\left\{\zeta = \frac{-\alpha}{\sqrt{\alpha^2+\beta^2}}\right\}$ are also computed for each case to substantiate the dynamic assessment. These parameters serve to theoretically validate the simulation results. The detailed explanation is as follows:

6.5.1. SSR: Case-wise comparative Analysis

Case (1): In Case 1, the system exhibits poorly damped modes, especially in the first few eigenvalues. As seen in Figure 6-13 and detailed in Table 6-4, the least stable pole is located at $14.166 \pm j12.44$, with a very low damping ratio (DR) of -75.14% and a frequency of oscillation (FOO) of $1.98\ Hz$, indicating substantial instability. The subsequent modes show a gradual increase in frequency from $4.35\ Hz$ to $6.2\ Hz$ and improving damping ratios (-39.55% to -20.72%), but all remain in the RHP. These values indicate that the system is still highly unstable, with weak damping in the low-frequency oscillatory range, typical of SSIs.

Case (2): In Case 2, the real part of the eigenvalues begins to approach zero and even becomes slightly negative, suggesting marginally stable to weakly damped oscillations. As illustrated in Figure 6-13 and summarized in Table 6-4, one such mode, $-0.973 \pm j105.344$, yields a frequency of $16.77\ Hz$ and a positive DR of 0.92%, indicating a minor improvement in stability. Earlier modes like $4.995 \pm j66.208$ still lie in the RHP with negative damping (-7.52%), but overall, the trajectory of poles suggests a transition toward increased damping. However, low-frequency oscillations remain prominent and inadequately controlled.

Compared to **Case (1)**, the first mode's damping in **Case (2)** improves from -75.14% to -7.52% ($\approx 90\%$ enhancement), while the fourth mode shifts from -20.72% to $+0.92\%$ ($>104\%$ improvement). Both modes in **Case (1)** had positive real parts (14.166 and 8.249), indicating RHP instability, whereas in **Case (2)**, the fourth mode moves to the LHP (-0.973), signalling a transition to stability. Oscillation frequencies also increase from $1.98\ Hz$ and $6.2\ Hz$ to $10.54\ Hz$ and $16.77\ Hz$, suggesting improved damping and faster dynamic response.

Case (3): Case (3) demonstrates a significant improvement in damping characteristics. As shown in Figure 6-13 and detailed in Table 6-4, all eigenvalues are now firmly located in the LHP, with increasingly negative real parts. The FOO ranges from $29.31\ Hz$ to $39.59\ Hz$, while damping ratios improve substantially from 8.36% to 21.76%. The most dominant mode, $-15.443 \pm j184.184$, reflects a relatively low-frequency oscillation but with acceptable damping. These results indicate that the system is recovering stability and beginning to exhibit a strongly damped dynamic response under the new compensation level.

Compared to **Case (2)**, **Case (3)** shows a marked improvement in damping behaviour. The first mode's DR increases from *–7.52%* to *+8.36%*, a relative enhancement of over *215%*, while the fourth mode improves from *+0.92%* to *21.76%*, reflecting a substantial rise of over *2264%*. The corresponding real parts also migrate significantly leftward, with the fourth mode shifting from *–0.973* to *–55.443*, indicating much stronger stability. Furthermore, FOO increases from *10.54 Hz* and *16.77 Hz* in **Case (2)** to *29.31 Hz* and *39.59 Hz* in *Case (3)*, highlighting a faster and more robust dynamic response.

Case (4): **Case (4)** presents the best dynamic performance among all SSR scenarios. As illustrated in Figure 6-13 and summarized in Table 6-4, the poles have shifted further left into the LHP with more negative real parts (up to $-126.1 \pm j313.862$) and high-frequency components around *45–50 Hz*. Damping ratios rise sharply, reaching up to *37.28%*, indicating highly damped system behaviour. These results suggest that the increasing compensation level successfully enhances the system's dynamic stability, moving it away from dangerous SSIs.

Building upon the improved damping observed in **Case (3)**, **Case (4)** delivers a more pronounced enhancement in small-signal stability. The dominant poles in **Case (4)** not only shift further leftward into the LHP but also exhibit greater separation from the imaginary axis, with real parts reaching as low as *–126.1* compared to *–55.443* in **Case (3)**. This indicates a significantly faster rate of system response decay. Furthermore, the FOO increases from *39.59 Hz* in **Case (3)** to approximately *45–50 Hz* in **Case (4)**, reflecting a higher frequency dynamic mode with superior damping. The most dominant mode in **Case (4)**, $-126.1 \pm j313.862$, suggests a rapid suppression of rotor-originated oscillations, whereas **Case (3)**'s dominant pole at $-15.443 \pm j184.184$ remains relatively slower. Additionally, DRs rise sharply from a maximum of *21.76%* in **Case (3)** to *37.28%* in **Case (4)**, indicating stronger resistance to oscillatory growth. These changes collectively affirm that the proposed VISDC in **Case (4)** ensures the highest level of SSR mitigation, pushing the system well beyond marginal stability and into a highly damped regime suitable for real-world grid disturbance.

6.5.2. Transient Analysis: Case-wise comparative Analysis

Case (A): **Case (A)** reflects instability in the initial modes, as seen in $33.119 \pm j27.615$ with a low DR of -76.8% and a frequency of $4.4\ Hz$. As the modes progress, damping improves slightly (e.g., -9.78% at $17.83\ Hz$), but several modes remain in or near the RHP, suggesting persistent vulnerability during the fault. The system still experiences strong low-frequency oscillations with insufficient damping, mirroring the unstable dynamics observed in SSR **Case (1)**. These observations are clearly illustrated in Figure 6-14 and quantitatively summarized in Table 6-4, reinforcing the conclusion that **Case (A)** remains dynamically unstable under faulted conditions.

Case (B): In **Case (B)**, a notable transition in system dynamics is observed, with eigenvalues beginning to shift into the LHP. The dominant poles, such as $-0.384 \pm j121.077$, exhibit a positive DR of 0.32%, and subsequent modes demonstrate incremental improvement, reaching up to 1.74%, with associated frequencies around $31.55\ Hz$. These results, as depicted in Figure 6-14 and summarized in Table 6-4, indicate early signs of stabilization, although the system continues to display marginally damped oscillations, reflecting limited robustness under faulted conditions.

Compared to **Case (A)**, **Case (B)** shows a clear improvement in dynamic behaviour. The first mode's DR rises from -76.8% to $+0.32\%$, with its FOO increasing from $4.4\ Hz$ to $19.27\ Hz$. Similarly, the fourth mode improves from -9.78% to $+1.74\%$, with a frequency shift from $17.83\ Hz$ to $31.55\ Hz$. The corresponding real parts also migrate from unstable RHP values (e.g., 33.119) in *Case (A)* to slightly negative values (e.g., -0.384) in **Case (B)**. These transitions reflect a partial recovery in system dynamics, indicating improved damping and faster oscillatory response, though overall robustness under faulted conditions remains limited.

Case (C): **Case (C)** shows further enhancement in system damping, with all dominant poles now well into the LHP. As illustrated in Figure 6-14 and summarized in Table 6-4, frequencies rise to the range of $34\ Hz$ to $41\ Hz$, and DRs improve to between 3.4% and 7.8%, indicating better oscillation control. The leading eigenvalue at $-7.298 \pm j214.716$ demonstrates enhanced damping (3.4%) and underscores the controller's growing effectiveness in mitigating resonance

under fault conditions. This steady progression in damping reflects a more robust dynamic response and increasingly successful fault recovery mechanisms.

Compared to **Case (B)**, **Case (C)** demonstrates a clear progression in damping behaviour. The first mode's DR improves from *0.32%* at *31.55 Hz* to *3.4%* at *34.17 Hz*, reflecting a more than tenfold relative increase. Similarly, the fourth mode shows a notable enhancement from *1.74%* at *31.55 Hz* to *7.8%* at *41.2 Hz*. In addition, the associated eigenvalues shift further left in the LHP (e.g., from *–0.384* to *–7.298*), indicating a strengthened move toward stable and well-damped system dynamics under faulted operation.

Case (D): **Case (D)** demonstrates the most favourable behaviour under LLLG faults. As illustrated in Figure 6-14 and summarized in Table 6-4, the eigenvalues exhibit more negative real parts (e.g., *–40.682 ± j302.774*) and frequencies extending up to *48.19 Hz*, with the highest DR reaching *13.32%*. The system shows strong damping characteristics across all four dominant modes, confirming that fault-induced oscillations are significantly mitigated. These findings indicate that the system, in this configuration, is dynamically robust and well-stabilized even under severe fault disturbances.

Compared to **Case (C)**, **Case (D)** exhibits a notable improvement in both damping and frequency response. The first mode's DR increases from *3.4%* to *13.32%*, marking a relative rise of approximately *292%*, while the fourth mode improves from *7.8%* to *11.96%*, a gain of nearly *53%*. Additionally, the dominant eigenvalues shift further left in the complex plane, with real parts moving from *–7.298* in Case C to *–40.682* in **Case (D)**, indicating stronger stability. The corresponding frequencies also increase from a range of *34 Hz* to *41 Hz* to *41.91 Hz* to *48.19 Hz*, highlighting a quicker oscillatory response. These developments reflect a significantly enhanced dynamic performance in **Case (D)** under faulted conditions.

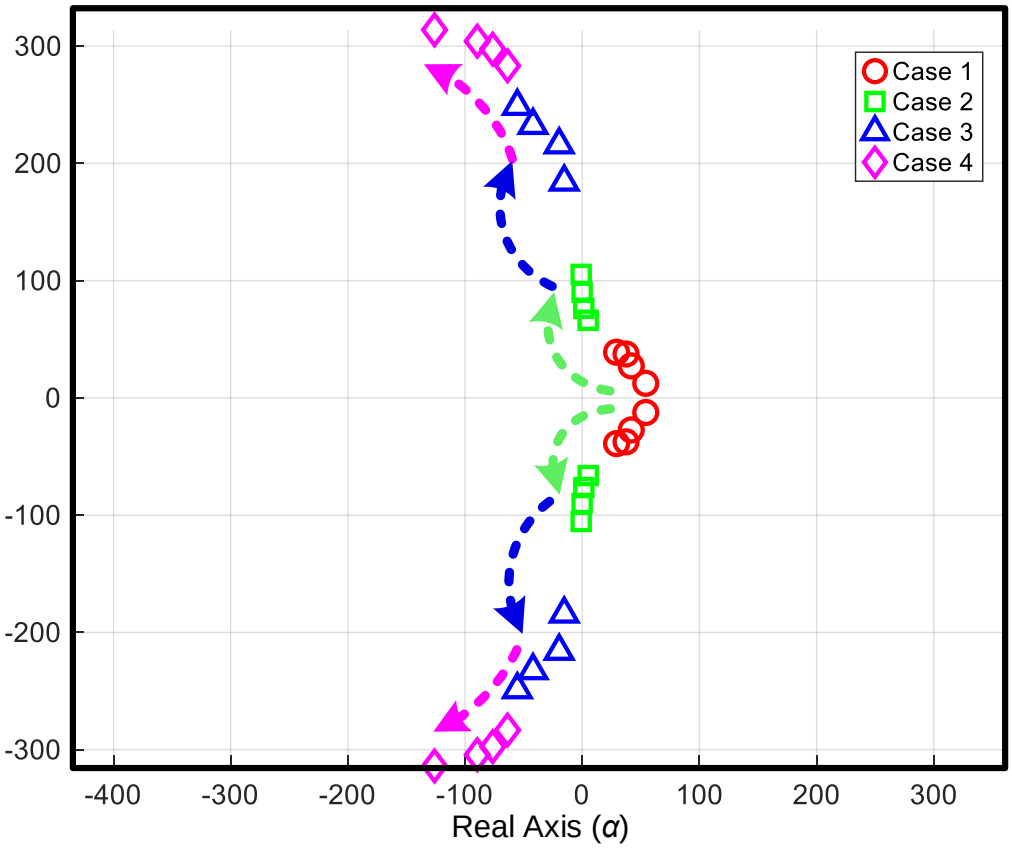

Figure 6-13. Pole Plot of Eigenvalues of SSR Analysis

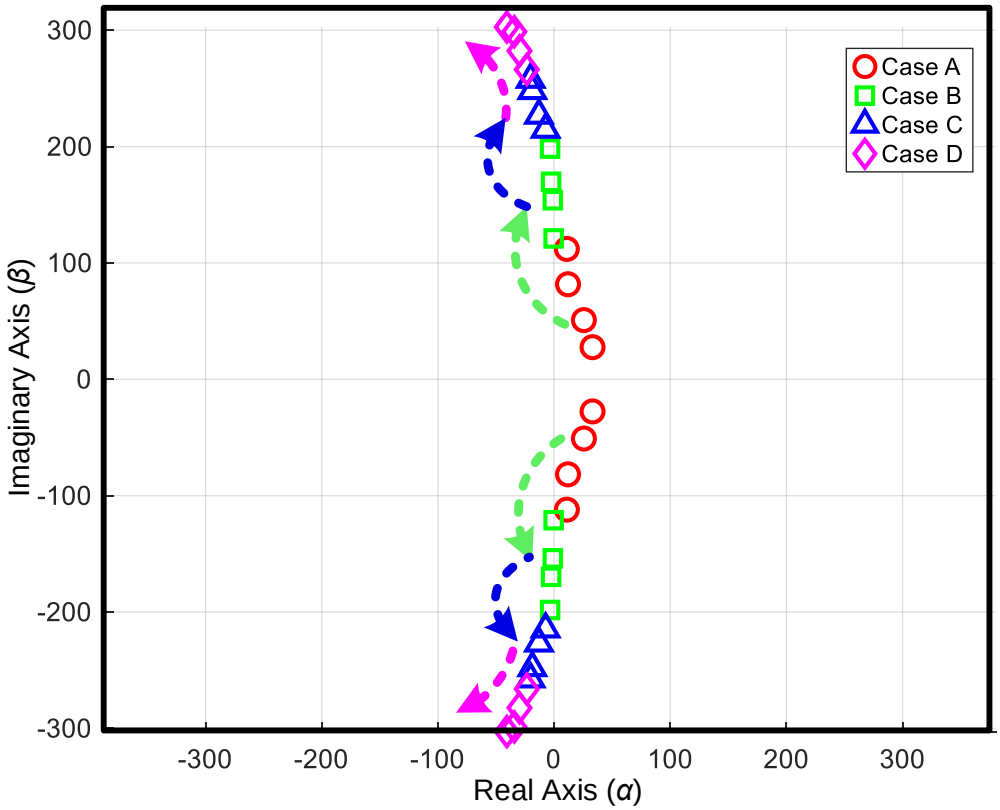

Figure 6-14. Pole Plot of Eigenvalues of Transient Analysis

Table 6-4. Eigenvalues under different test conditions

Mode	SSR analysis (at 60 %)				Transient analysis			
	Case	*Eigenvalues*	*FOO (Hz)*	*DR (%)*	*Case*	*Eigenvalues*	*FOO (Hz)*	*DR (%)*
1	**1**	14.166 ± j12.44	1.98	-75.14	**A**	33.119 ± j27.615	4.395	-76.8
2		11.76 ± j27.312	4.347	-39.55		25.67 ± j50.9	8.101	-45.03
3		9.373 ± j37.442	5.959	-24.29		12 ± j81.681	13	-14.54
4		8.249 ± j38.955	6.2	-20.72		11.009 ± j112.029	17.83	-9.78
1	**2**	4.995 ± j66.208	10.537	-7.52	**B**	-0.384 ± j121.077	19.27	0.32
2		1.314 ± j76.456	12.168	-1.72		-1.071 ± j153.881	24.491	0.7
3		-0.146 ± j90	14.323	0.16		-2.583 ± j169.761	27.018	1.52
4		-0.973 ± j105.34	16.766	0.92		-3.44 ± j198.265	31.554	1.74
1	**3**	-15.44 ± j184.18	29.313	8.36	**C**	-7.298 ± j214.716	34.173	3.4
2		-19.73 ± j215.93	34.366	9.1		-13.006 ± j226.82	36.099	5.72
3		-42.04 ± j232.48	37	17.8		-18.72 ± j247.969	39.465	7.53
4		-55.44 ± j248.73	39.587	21.76		-20.16 ± j257.659	41.007	7.8
1	**4**	-63.774 ± j283.2	45.072	21.97	**D**	-23.493 ± j266.21	42.369	8.79
2		-76.44 ± j297.44	47.34	24.89		-29.77 ± j282.289	44.927	10.49
3		-89.61 ± j304.22	48.419	28.26		-34.217 ± j298.72	47.543	11.38
4		-126.1 ± j313.86	49.952	37.28		-40.68 ± j302.774	48.188	13.32

CHAPTER 7. CONCLUSIONS AND FUTURE WORK

7.1. Conclusion

This study presents a detailed comparative evaluation of various SDC strategies for mitigating SSR and enhancing the dynamic stability of wind-integrated PSs under fault conditions and varying compensation levels. Through extensive simulation-based analysis of four distinct control scenarios, the proposed VISDC implemented at the RSC has been demonstrated to offer the most effective and robust solution. **Case (1)** and **Case (A)** clearly indicate severe instability and prolonged negative damping oscillations, underlining the system's vulnerability without appropriate damping mechanisms. **Case (2)** and **Case (B)** offer slight improvements but fail to address the rotor-originated disturbances, as the controllers in these cases are placed in the GSC of the DFIG. **Case (3)** and **Case (C)** significantly enhance performance, reducing peak overshoot and settling time, but introduce increased system complexity and are not optimal for extreme grid events. In contrast, **Case (4)** and **Case (D)** outperform all other configurations by directly damping rotor-induced oscillations, ensuring the fastest post-fault recovery, lowest overshoot (~10–14%), and shortest settling time (~3.1–3.2 s). Moreover, the VI effect adds stability by mitigating sudden transients. Overall, the proposed VISDC not only improves fault resilience and SSR mitigation but also achieves a balanced trade-off between performance, robustness, and simplicity, making it highly suitable for modern WE applications, especially in weak and remote grid conditions.

In addition to SSR mitigation, the proposed VISDC demonstrates exceptional performance in enhancing transient stability under severe fault scenarios. The time-domain results and eigenvalue-based validation confirm that **Case (D)** achieves superior damping characteristics during LLLG faults, with dominant poles well into the LHP and significantly improved DRs across all critical modes. This leads to rapid system stabilization, effective suppression of oscillatory behaviour, and reliable dynamic recovery following grid disturbances. The consistent improvement in both SSR and transient fault conditions establishes VISDC as a comprehensive damping strategy capable of ensuring grid compliance and operational security in high-penetration wind PSs.

Key Findings:

1. A VI-based RSC control strategy is proposed to enhance frequency stability using WT rotor inertia, especially under low-inertia conditions.
2. The optimized RSC-based damping controller outperforms GSC-based methods in mitigating SSR by directly targeting rotor-side oscillations.
3. Eigenvalue analysis confirms improved damping under both SSR and fault disturbances, with all poles shifted to the LHP.
4. RSC-centric control enables effective VI deployment in weak and remote WFs, improving fault resilience and grid support.
5. Comparative analysis reveals superior performance of RSC-based schemes in SSR mitigation, FRT, and dynamic response.
6. Real-time validation using OPAL-RT and RT-Lab confirms close alignment with simulation results, verifying practical feasibility and robustness.

7.2. Future Scope

While the proposed controller has demonstrated effective SSR mitigation under various disturbances and configurations, several avenues remain open for exploration. These directions can further enhance system adaptability, resilience, and integration within modern power grids. Notable potential extensions include:

1. **ML/AI-Based Adaptive Control:** Smart algorithms can auto-tune controllers in real time, offering proactive and model-free SSR mitigation.
2. **Grid-Forming Converter Transition:** Shifting from grid-following to grid-forming enhances resilience in weak grids and transforms SSR behaviour fundamentally.
3. **BESS Coordination:** Battery Energy Storage System (BESS) can support fast damping and inertia emulation, making it ideal for SSR suppression and FRT enhancement.
4. **Cybersecurity in Converter Control:** With growing digital connectivity, protecting converters from cyber threats is vital for maintaining stable and secure wind operations.

These future directions not only promise to strengthen the technical capabilities of SSR mitigation strategies but also align with the evolving requirements of next-generation smart and secure PSs.

ANNEXURE

DFIG P_{rated} (total)	100 MW
No. of turbines	66 (each 1.5 MW)
Transformer	575V/161kV; 115.5 MVA
Radius of WT	54.735 m
GB Ratio	1:166
DC-link voltage	1150V
Voltage rating GSC and RSC	1800V
Current rating GSC	2.3 kA
Current rating RSC	826 A
PEC rating (each WT)	0.417 MVA

REFERENCES

[1] B. Wu, Y. Lang, N. Zargari, and S. Kouro, *Power Conversion and Control of Wind Energy Systems*, 1st ed. Wiley, 2011. doi: 10.1002/9781118029008.

[2] B. Lin and J. O. Okoye, 'Towards renewable energy generation and low greenhouse gas emission in high-income countries: Performance of financial development and governance', *Renewable Energy*, vol. 215, p. 118931, Oct. 2023, doi: 10.1016/j.renene.2023.118931.

[3] J. S.R., D. L. J., E. P. Cheriyan, and S. T.K., 'Identification and analysis of subsynchronous oscillations in DFIG based wind power plants', in *2016 IEEE Region 10 Conference (TENCON)*, Singapore: IEEE, Nov. 2016, pp. 850–853. doi: 10.1109/TENCON.2016.7848125.

[4] A. A. Eladl *et al.*, 'A comprehensive review on wind power spillage: Reasons, minimization techniques, real applications, challenges, and future trends', *Electric Power Systems Research*, vol. 226, p. 109915, Jan. 2024, doi: 10.1016/j.epsr.2023.109915.

[5] A. Qazi *et al.*, 'Towards Sustainable Energy: A Systematic Review of Renewable Energy Sources, Technologies, and Public Opinions', *IEEE Access*, vol. 7, pp. 63837–63851, 2019, doi: 10.1109/ACCESS.2019.2906402.

[6] Y. Bostani, S. Jalilzadeh, S. Mobayen, T. Rojsiraphisal, and A. Bartoszewicz, 'Damping of Subsynchronous Resonance in Utility DFIG-Based Wind Farms Using Wide-Area Fuzzy Control Approach', *Energies*, vol. 15, no. 5, p. 1787, Feb. 2022, doi: 10.3390/en15051787.

[7] N. Verma and N. Kumar, 'DFIG-Based Wind Plant Coupled Series Compensated Transmission Line: Modeling and SSR Stability Analysis', *J. Inst. Eng. India Ser. B*, vol. 103, no. 6, pp. 1917–1926, Dec. 2022, doi: 10.1007/s40031-022-00807-6.

[8] J. Shair, X. Xie, J. Yang, J. Li, and H. Li, 'Adaptive Damping Control of Subsynchronous Oscillation in DFIG-Based Wind Farms Connected to Series-Compensated Network', *IEEE Trans. Power Delivery*, vol. 37, no. 2, pp. 1036–1049, Apr. 2022, doi: 10.1109/TPWRD.2021.3076053.

[9] S. Müller, M. Deicke, and R. W. De Doncker, 'Doubly Fed Induction Generator Systems for Wind Turbines: A Viable Alternative to Adjust Speed over a Wide Range at Minimal Cost', *IEEE Ind. Appl. Mag.*, vol. 8, no. 3, pp. 26–33, May 2002, doi: 10.1109/2943.999610.

[10] R. Pena, J. C. Clare, and G. M. Asher, 'Doubly fed induction generator using back-to-back PWM converters and its application to variable-speed wind-energy generation', *IEE Proc., Electr. Power Appl.*, vol. 143, no. 3, p. 231, 1996, doi: 10.1049/ip-epa:19960288.

[11] Md. A. Chowdhury, Md. A. Mahmud, W. Shen, and H. R. Pota, 'Nonlinear Controller Design for Series-Compensated DFIG-Based Wind Farms to Mitigate Subsynchronous Control Interaction', *IEEE Trans. Energy Convers.*, vol. 32, no. 2, pp. 707–719, Jun. 2017, doi: 10.1109/TEC.2017.2660539.

[12] S. Puchalapalli and B. Singh, 'A Single Input Variable FLC for DFIG-Based WPGS in Standalone Mode', *IEEE Trans. Sustain. Energy*, vol. 11, no. 2, pp. 595–607, Apr. 2020, doi: 10.1109/TSTE.2019.2898115.

[13] Y. Cheng *et al.*, 'Real-World Subsynchronous Oscillation Events in Power Grids With High Penetrations of Inverter-Based Resources', *IEEE Trans. Power Syst.*, vol. 38, no. 1, pp. 316–330, Jan. 2023, doi: 10.1109/TPWRS.2022.3161418.

[14] S. Kumar and N. Kumar, 'Alleviation SSR and Low Frequency Power Oscillations in Series Compensated Transmission Line using SVC Supplementary Controllers', *J. Inst. Eng. India Ser. B*, vol. 98, no. 3, pp. 255–266, Jun. 2017, doi: 10.1007/s40031-016-0253-5.
[15] K. R. Padiyar, *Analysis of Subsynchronous Resonance in Power Systems*. Boston, MA: Springer US, 1999. doi: 10.1007/978-1-4615-5633-6.
[16] N. Verma, N. Kumar, S. Gupta, H. Malik, and F. P. García Márquez, 'Review of sub-synchronous interaction in wind integrated power systems: classification, challenges, and mitigation techniques', *Prot Control Mod Power Syst*, vol. 8, no. 1, p. 17, Dec. 2023, doi: 10.1186/s41601-023-00291-0.
[17] 'Proposed Terms and Definitions for Subsynchronous Oscillations', *IEEE Trans. on Power Apparatus and Syst.*, vol. PAS-99, no. 2, pp. 506–511, 1980, doi: 10.1109/TPAS.1980.319686.
[18] S. Xia, Q. Zhang, S. T. Hussain, B. Hong, and W. Zou, 'Impacts of Integration of Wind Farms on Power System Transient Stability', *Applied Sciences*, vol. 8, no. 8, p. 1289, Aug. 2018, doi: 10.3390/app8081289.
[19] S. Soued, H. S. Ramadan, and M. Becherif, 'Effect of Doubly Fed Induction Generator on Transient Stability Analysis under Fault Conditions', *Energy Procedia*, vol. 162, pp. 315–324, Apr. 2019, doi: 10.1016/j.egypro.2019.04.033.
[20] A. Gourma, A. Berdai, M. Reddak, and V. Tytiuk, 'Impact of Dispersed Wind Farms' Integration on Transient Stability of Interconnected Grid', *IREE*, vol. 15, no. 1, p. 87, Feb. 2020, doi: 10.15866/iree.v15i1.17218.
[21] A. Chen, D. Xie, D. Zhang, C. Gu, and K. Wang, 'PI Parameter Tuning of Converters for Sub-Synchronous Interactions Existing in Grid-Connected DFIG Wind Turbines', *IEEE Trans. Power Electron.*, vol. 34, no. 7, pp. 6345–6355, Jul. 2019, doi: 10.1109/TPEL.2018.2875350.
[22] X. Wu, Y. Guan, X. Yang, W. Ning, and M. Wang, 'Low-cost control strategy based on reactive power regulation of DFIG-based wind farm for SSO suppression', *IET Renewable Power Generation*, vol. 13, no. 1, pp. 33–39, Jan. 2019, doi: 10.1049/iet-rpg.2018.5050.
[23] G. D. Irwin, A. K. Jindal, and A. L. Isaacs, 'Sub-synchronous control interactions between type 3 wind turbines and series compensated AC transmission systems', in *2011 IEEE Power and Energy Society General Meeting*, San Diego, CA: IEEE, Jul. 2011, pp. 1–6. doi: 10.1109/PES.2011.6039426.
[24] I. Vieto and J. Sun, 'Damping of subsynchronous resonance involving Type-III wind turbines', in *2015 IEEE 16th Workshop on Control and Modeling for Power Electronics (COMPEL)*, Vancouver, BC, Canada: IEEE, Jul. 2015, pp. 1–8. doi: 10.1109/COMPEL.2015.7236515.
[25] M. A. Chowdhury and M. A. Mahmud, 'Mitigation of subsynchronous control interaction in series-compensated DFIG-based wind farms using a nonlinear partial feedback linearizing controller', in *2016 IEEE Innovative Smart Grid Technologies - Asia (ISGT-Asia)*, Melbourne, Australia: IEEE, Nov. 2016, pp. 335–340. doi: 10.1109/ISGT-Asia.2016.7796408.
[26] J. Ndirangu, J. Nderu, and G. Irungu, 'Impact of Variation of Virtual Inertia and Virtual Damping on Frequency and Power Angle Responses of Virtual Inertia Emulation Controlled Converter', in *2022 IEEE PES/IAS PowerAfrica*, Kigali, Rwanda: IEEE, Aug. 2022, pp. 1–4. doi: 10.1109/PowerAfrica53997.2022.9905353.

[27] V. B. Virulkar and G. V. Gotmare, ‘Sub-synchronous resonance in series compensated wind farm: A review’, *Renewable and Sustainable Energy Reviews*, vol. 55, pp. 1010–1029, Mar. 2016, doi: 10.1016/j.rser.2015.11.012.
[28] J. Shair, X. Xie, and G. Yan, ‘Mitigating subsynchronous control interaction in wind power systems: Existing techniques and open challenges’, *Renewable and Sustainable Energy Reviews*, vol. 108, pp. 330–346, Jul. 2019, doi: 10.1016/j.rser.2019.04.003.
[29] D. Duc Tung, L. Van Dai, and L. Cao Quyen, ‘Subsynchronous Resonance and FACTS-Novel Control Strategy for Its Mitigation’, *Journal of Engineering*, vol. 2019, pp. 1–14, Jul. 2019, doi: 10.1155/2019/2163908.
[30] M. P. Thakre, V. S. Kale, K. R. Dhenuvakonda, B. S. Umre, and A. S. Junghare, ‘Study and Mitigation of Subsynchronous Oscillations with SSC Based SSSC’, *JPEE*, vol. 03, no. 09, pp. 33–43, 2015, doi: 10.4236/jpee.2015.39003.
[31] F. Zhang and Z. Xu, ‘Effect of Exciter and PSS on SSR Damping’, in *2007 IEEE Power Engineering Society General Meeting*, Tampa, FL, USA: IEEE, Jun. 2007, pp. 1–7. doi: 10.1109/PES.2007.385672.
[32] F. M. Hughes, O. Anaya-Lara, N. Jenkins, and G. Strbac, ‘A Power System Stabilizer for DFIG-Based Wind Generation’, *IEEE Trans. Power Syst.*, vol. 21, no. 2, pp. 763–772, May 2006, doi: 10.1109/TPWRS.2006.873037.
[33] Z. Miao, L. Fan, D. Osborn, and S. Yuvarajan, ‘Control of DFIG-Based Wind Generation to Improve Interarea Oscillation Damping’, *IEEE Trans. Energy Convers.*, vol. 24, no. 2, pp. 415–422, Jun. 2009, doi: 10.1109/TEC.2009.2015980.
[34] G. Tsourakis, B. M. Nomikos, and C. D. Vournas, ‘Contribution of Doubly Fed Wind Generators to Oscillation Damping’, *IEEE Trans. Energy Convers.*, vol. 24, no. 3, pp. 783–791, Sep. 2009, doi: 10.1109/TEC.2009.2025330.
[35] ‘A Review on Subsynchronous Resonance and its Mitigation Techniques in DFIG based Wind Farms’, *IJRER*, no. v8i4, 2018, doi: 10.20508/ijrer.v8i4.8620.g7532.
[36] B. Liu, J. Zhao, Q. Huang, F. Milano, Y. Zhang, and W. Hu, ‘Nonlinear Virtual Inertia Control of WTGs for Enhancing Primary Frequency Response and Suppressing Drivetrain Torsional Oscillations’, *IEEE Trans. Power Syst.*, vol. 36, no. 5, pp. 4102–4113, Sep. 2021, doi: 10.1109/TPWRS.2021.3055262.
[37] Q. Peng, Z. Tang, Y. Yang, T. Liu, and F. Blaabjerg, ‘Event-Triggering Virtual Inertia Control of PV Systems With Power Reserve’, *IEEE Trans. on Ind. Applicat.*, vol. 57, no. 4, pp. 4059–4070, Jul. 2021, doi: 10.1109/TIA.2021.3080227.
[38] * 21PESGM2215 *et al.*, ‘Modeling and Control Challenges of Weak Low-inertia Power Systems’, *IEEE*. doi: 10.17023/F2TE-YG46.
[39] C. Hou, Z. Xu, K. B. Karnauskas, D. Huang, and H. Lu, ‘Detecting and calibrating large biases in global onshore wind power assessment across temporal scales’, *Nat Commun*, vol. 16, no. 1, p. 3775, Apr. 2025, doi: 10.1038/s41467-025-59195-2.
[40] H. S. Kim and D. D.-C. Lu, ‘Wind Energy Conversion System from Electrical Perspective—A Survey’, *SGRE*, vol. 01, no. 03, pp. 119–131, 2010, doi: 10.4236/sgre.2010.13017.
[41] S. Tyagi, B. Singh, and S. Das, ‘Small Hydro Based Grid Forming Converter Having Power Sharing and Synchronization Capability With DFIG Based WECS’, *IEEE Trans. on Ind. Applicat.*, pp. 1–11, 2023, doi: 10.1109/TIA.2023.3261863.
[42] I. Serban, G. D. Andreescu, L. Tutelea, C. Lascu, I. Boldea, and F. Blaabjerg, ‘New State Observers and Sensorless Control of Wound Rotor Induction Generator (WRIG) at Power Grid with Experimental Characterization’, in *IECON 2006 - 32nd*

Annual Conference on IEEE Industrial Electronics, Paris, France: IEEE, Nov. 2006, pp. 4260–4265. doi: 10.1109/IECON.2006.347548.

[43] X. Zhang, X. Xie, J. Shair, H. Liu, Y. Li, and Y. Li, 'A Grid-Side Subsynchronous Damping Controller to Mitigate Unstable SSCI and Its Hardware-in-the-loop Tests', *IEEE Trans. Sustain. Energy*, vol. 11, no. 3, pp. 1548–1558, Jul. 2020, doi: 10.1109/TSTE.2019.2930289.

[44] D.-Y. Sun, Z.-J. Qian, W.-Q. Shen, K. Zhou, N.-Z. Jin, and Q.-G. Chen, 'Mechanism Analysis of Multiple Disturbance Factors and Study of Suppression Strategies of DFIG Grid-Side Converters Caused by Sub-Synchronous Oscillation', *Electronics*, vol. 12, no. 10, p. 2293, May 2023, doi: 10.3390/electronics12102293.

[45] D. Sun, W. Shen, Z. Qian, F. Meng, Y. Sha, and K. Zhou, 'Multi-Disturbance Factors Analysis and Suppression Strategy of Sub-Synchronous Oscillation on DFIG Grid-Side Converter', *IEEE Access*, vol. 11, pp. 48881–48892, 2023, doi: 10.1109/ACCESS.2023.3277622.

[46] Z. Moradi-Shahrbabak, 'Proposed sub-synchronous resonance damping controller for large-scale wind farms', *IET Renewable Power Gen*, vol. 17, no. 13, pp. 3209–3220, Oct. 2023, doi: 10.1049/rpg2.12837.

[47] P.-H. Huang, M. S. El Moursi, W. Xiao, and J. L. Kirtley, 'Subsynchronous Resonance Mitigation for Series-Compensated DFIG-Based Wind Farm by Using Two-Degree-of-Freedom Control Strategy', *IEEE Trans. Power Syst.*, vol. 30, no. 3, pp. 1442–1454, May 2015, doi: 10.1109/TPWRS.2014.2348175.

[48] J. Shair, X. Xie, Y. Li, and V. Terzija, 'Hardware-in-the-Loop and Field Validation of a Rotor-Side Subsynchronous Damping Controller for a Series Compensated DFIG System', *IEEE Trans. Power Delivery*, vol. 36, no. 2, pp. 698–709, Apr. 2021, doi: 10.1109/TPWRD.2020.2989475.

[49] M. Tang, Z. Li, G. Li, Z. Qie, and Y. Yu, 'Power Oscillation Characteristics of Large Power Systems under Random Disturbances', in *2021 IEEE 5th Conference on Energy Internet and Energy System Integration (EI2)*, Taiyuan, China: IEEE, Oct. 2021, pp. 2866–2870. doi: 10.1109/EI252483.2021.9713269.

[50] T. Kerdphol, F. S. Rahman, Y. Mitani, M. Watanabe, and S. Kufeoglu, 'Robust Virtual Inertia Control of an Islanded Microgrid Considering High Penetration of Renewable Energy', *IEEE Access*, vol. 6, pp. 625–636, 2018, doi: 10.1109/ACCESS.2017.2773486.

[51] Arani and El-Saadany, 'Implementing Virtual Inertia in DFIG-Based Wind Power Generation', *IEEE Trans. Power Syst.*, vol. 28, no. 2, pp. 1373–1384, May 2013, doi: 10.1109/TPWRS.2012.2207972.

[52] M. Tuo and X. Li, 'Optimal Allocation of Virtual Inertia Devices for Enhancing Frequency Stability in Low-Inertia Power Systems', in *2021 North American Power Symposium (NAPS)*, College Station, TX, USA: IEEE, Nov. 2021, pp. 1–6. doi: 10.1109/NAPS52732.2021.9654729.

[53] L. Qi, W. Jiahui, W. Haiyun, Z. Hua, and Y. Jian, 'Effect of DFIG control parameters on small signal stability in power systems', *Sci Rep*, vol. 13, no. 1, p. 2476, Feb. 2023, doi: 10.1038/s41598-023-29278-5.

[54] L. Wang, X. Xie, Q. Jiang, H. Liu, Y. Li, and H. Liu, 'Investigation of SSR in Practical DFIG-Based Wind Farms Connected to a Series-Compensated Power System', *IEEE Trans. Power Syst.*, vol. 30, no. 5, pp. 2772–2779, Sep. 2015, doi: 10.1109/TPWRS.2014.2365197.

[55] M. A. Mahmud, M. J. Hossain, H. R. Pota, and N. K. Roy, 'Robust Nonlinear Controller Design for Three-Phase Grid-Connected Photovoltaic Systems Under

Structured Uncertainties', *IEEE Trans. Power Delivery*, vol. 29, no. 3, pp. 1221–1230, Jun. 2014, doi: 10.1109/TPWRD.2014.2309594.